Dissertation

submitted to the
Combined Faculties for the Natural Sciences and for Mathematics
of the Ruperto-Carola University of Heidelberg, Germany
for the degree of
Doctor of Natural Sciences

presented by

Diplom-Physiker:	Thomas Fuchs
born in:	Solingen

Oral examination: 27.06.2007

Laser-accelerated particles: Investigations towards applications in radiotherapy

Referees: Prof. Dr. Uwe Oelfke

Prof. Dr. Dr. Jürgen Debus

Laser-beschleunigte Teilchen: Untersuchungen zu potenziellen Anwendungenen in der Strahlentherapie

Zusammenfassung

Laser-Plasma-Beschleuniger bieten die Möglichkeit der Erzeugung hochenergetischer Teilchenstrahlen. Da sie im Gegensatz zu konventionellen Beschleunigern kompakter und kostengünstiger sind, wurden in dieser Arbeit potenzielle Anwendungen in der Strahlentherapie untersucht. Zunächst wurde die Abängigkeit der maximalen Protonenenergie von Laser- und Targetparametern studiert. Die Ergebnisse zeigen, dass mit zukünftigen Laser-Systemen klinisch relevante Energien erreicht werden könnten. Zusätzlich wurden Möglichkeiten einer Modifikation des typischerweise exponentiell abfallenden Energiespektrums analysiert. Ein Ansatz bei dem das Spektrum durch elektrische Felder modifiziert wird, die an einem zweiten Target mittels eines zweiten Lasers erzeugt wurden, zeigte unzureichende Ergebnisse. Bei den sogenannten Double-Layer-Targets hingegen weist das Energiespektrum einer zu Beginn an ein Substrat gelagerten Protonenschicht eine "quasi-monoenergetische" Struktur auf. Der Einfluss unterschiedlicher Targetparameter auf die Energieverteilung wurde analysiert und darauf basierend ein Vergleich mit IMRT Prostata-Bestrahlungsplänen durchgeführt. Dieser zeigte für Protonenstrahlen mit einer endlichen Energiebreite eine Steigerung der Planqualität im Gegensatz zu einem Photonenplan. Im zweiten Teil wurden zunächst die dosimetrischen Eigenschaften laser-beschleunigter Elektronen untersucht. Für 250 MeV Elektronen weist die Tiefendosiskurve ein breites Maximum bei Tiefen $\geq$ 20 cm auf. Außerdem ist der Halbschatten eines Bestrahlungsfeldes in Tiefen $<$ 10 cm geringer als der eines Photonenfeldes. Diese Eigenschaften führen zu einer leichten Verbesserung der Qualität von Prostata-Bestrahlungsplänen im Vergleich zu IMRT Photonenplänen.

Laser-accelerated particles: Investigations towards applications in radiotherapy

Abstract

Laser-plasma accelerators provide a new method to create energetic particle beams. Due to their compactness and cost-efficiency the potential of an application to radiotherapy is studied in this work. First, the scaling of the proton energy with laser and target parameters was analyzed. The results imply that future laser systems might generate clinically relevant energies. Furthermore, options of controlling the typically Maxwellian proton energy spectrum were investigated. The approach of a modification by electric fields created at a second target with a second laser yielded insufficient results. However double-layer targets (a proton layer initially attached to a substrate) exhibit a "quasi-monoenergetic" part in the spectrum. Based on the studies of the effects of various target parameters on the energy spectrum a comparison of prostate treatment plans was performed. The increased plan quality for protons compared to photon beams varied with the assumed energy spread. The second part analyzes the dosimetric properties of laser-accelerated electrons. For 250 MeV electrons the depth dose curve yields a broad maximum at depths $\geq$ 20 cm. Additionally the penumbra of treatment fields is smaller compared to the one of photons at depths $<$ 10 cm. These properties led to slightly improved treatment plans compared to IMRT photon plans.

Contents

1 Introduction

The interaction of high-intensity lasers (intensity $I_0 \geq 10^{18} W/cm^2$) with matter provides a new means to create energetic particle beams [1]. In so-called laser-plasma accelerators the leading edge of a laser pulse instantaneously ionizes a gas or a solid target and the interaction of the electro-magnetic wave with the plasma can generate large electric fields which subsequently accelerate charged particles.

E.g. if the laser is focused onto a thin foil (e.g. an aluminum foil with thickness $d = 10$ μm) the leading edge of the pulse ionizes the target atoms and the main pulse is interacting with a highly ionized plasma at the front surface. A large fraction of the laser energy is absorbed as kinetic energy of the electrons in the plasma. In the main acceleration process, called target normal sheath acceleration (TNSA), the electrons penetrate through the foil and create electric fields of extraordinary strength which ionize atoms at the rear surface of the target. Furthermore, the strong electric field accelerates protons which can reach energies up to 60 MeV with currently available technology [2]. If the solid target is replaced by a helium gas jet, the electro-magnetic wave excites a plasma wave. The corresponding electric fields can exceed $\sim 10^{10}$ V/m which accelerates electrons to energies of up to 250 MeV [3].

A projected advantage of laser-acceleration of charged particles is the compactness and cost efficiency of the devices compared to conventional accelerators. Furthermore, currently available experimental laser-plasma accelerators create charged particle beams with maximal energies close to the regime required by modern radiotherapy. Consequently the potential usefulness of laser-plasma accelerators in radiation oncology has been discussed within recent years [4, 5, 6, 7]. This is especially important for the rapidly growing field of hadron therapy.

The advantages of e.g. proton beams compared to photons or electrons are indisputable. Protons clearly exhibit a superior depth dose curve compared to photons which are used in the majority of radiation treatments [8]. Behind the entrance region with a slowly rising dose a sharp increase, called Bragg peak, is following. This peak is located near the end of the finite range of the protons and can be tuned by the proton energy (e.g. 230 MeV protons yield a range of 32 cm). In contrast photons show a depth dose characteristic with a maximum dose at a depth of only a few centimeters and an exponential decrease afterwards. Consequently, proton therapy allows to reduce the integral dose to healthy tissue by a factor 2-3 in comparison to photons without compromising the therapeutic dose in the tumor.

However due to the tremendous building costs of hadron therapy facilities - the costs of the installation of a new cyclotron and a new gantry at the PSI in Villigen, Switzerland,

amount to about €20 million [9] - the majority of cancer patients are still treated with photons. Though it is hard to estimate the costs of a laser-driven proton accelerator it is one hope that the costs for these accelerators are significantly lower, as todays laser-systems are available for a few million euros.

Another restriction is the extended size of the particle accelerators and the beam delivering system. To utilize the benefits of flexible beam angles a rotating gantry is required. However these devices are very massive, e.g. the gantry at the PSI yields a weight of more than 100 tons. With a laser-plasma accelerator one could think of redirecting the laser with mirrors onto the target which itself is rotating around the patient. These potential advantages seem to make these devices to an attractive alternative to conventional particle accelerators in radiotherapy.

However, besides these promising advantages one has to admit that the technology and physical principles of laser-plasma accelerators are by far not as well established as for conventional synchrotrons or cyclotrons. In this thesis I therefore investigate some basic principles of laser-plasma accelerators and how these might be employed for the creation and clinical application of therapeutic proton beams.

The first objection to the possible use of laser-accelerated protons in radiotherapy is related to its currently achievable maximum energy. So far the maximum energy reached is about 60 MeV [2] and does not exceed the energy required for the treatment of ocular tumors (~ 70 MeV and is far away from proton energies needed for deep-seated tumors ($\sim 200 - 250$ MeV). Additionally the energy spectra of laser-accelerated protons show typically a Maxwellian shape which is inadequate for the use in radiotherapy. Only, recently the proposition [10] of double-layer targets to obtain "quasi-monoenergetic" proton spectra was experimentally realized [11, 12].

Another potential application of laser-accelerated particle beams refers to radiotherapy with electron beams. Conventional radiation therapy with electrons is restricted to non-deep-seated tumors. The energies which are used are confined to the range of $5 - 50$ MeV. However several groups [13, 14, 15] proposed the use of very high energy electrons ($150 - 250$ MeV) in radiotherapy. The increase in energy compared to the electron energies used so far, extends the possible use as the range increases. In part II of this work the potential of a future use of laser-accelerated electrons in radiotherapy is studied.

Thesis objectives and outline

In chapter 2 some general concepts and basics of laser and plasma physics are presented. Next, in part I the potential of laser-accelerated protons for an application in radiotherapy are investigated. At first the basic physics of proton acceleration is discussed by means of models and simulations (chapter 3). The underlying physics of the main acceleration process, the plasma expansion, is studied with a self-developed particle in cell (PIC) simulation code (chapter 4).

To estimate which intensities are required to achieve adequate proton energies for

radiotherapy, scaling laws of the maximum proton energy are investigated in chapter 5.

In the following, various methods to modify the typically Maxwellian proton energy spectrum are investigated. In chapter 6 a laser-target configuration of two lasers and two targets is studied by the means of PIC simulations[1]. Furthermore the properties of laser-accelerated protons from double-layer targets are analyzed in chapter 7. These studies include an analysis of treatment planning based on energy spectra expected for higher laser intensities (leading to higher proton energies) which are not available today. This part is completed by conclusions and a short outlook.

In part II the potential for a clinical use of laser-accelerated electrons is studied[2]. The presentation of the underlying physics of electron acceleration in chapter 10 is followed by an investigation of the dosimetric properties of these beams by Monte Carlo simulations in chapter 11. Finally, in chapter 12 the obtained dose distributions are used as a basis for a comparison of treatment plans for 6 MV photons and various electron beam set-ups.

At the end a short summary of all investigations is given.

[1] The PIC simulations in chapter 3, 5, 6 and 7 are performed with the electro-magnetic, fully relativistic PIC code *Calder* [16] which was made available by Erik Lefebvre from the Département de physique théorique et appliquée at the Commissariat à l'Énergie Atomique (CEA), Bruyères le Châtel, France.

[2] Parts of these studies were published in [17].

2 Basics

2.1 Plasma Basics

> *"A plasma is a quasi-neutral gas of charged and neutral particles which exhibits collective behavior."* [18]

This definition requires in addition declarations of *"quasi-neutral"* and *"collective behavior"*. The latter means that motions are not only depending on local conditions but are also driven by long-range electromagnetic forces. E.g. as charges move around electric fields can arise due to the charge displacement, a current is induced by the movement and hence a magnetic field. These fields can affect other charged particles far away.

"Quasi-neutrality" denotes that the plasma is neutral on a macroscopic scale such that for the electron and ion densities $n_{e/i}$ holds $n_i \simeq n_e \simeq n$, where n is called the plasma density. However there still exist non-vanishing electromagnetic forces on a microscopic scale. A criterion for this is that the length over which a charge is shielded by the plasma is much smaller than the characteristical length of the plasma itself.

2.1.1 Debye shielding

The aforementioned shielding distance is the *Debye length* λ_D. To compute this length one considers the following situation [18] in one dimension: At $x = 0$ the potential is held at a value ϕ_0 by a perfectly transparent grid (cf. figure 2.1). The Poisson equation for the potential $\phi(x)$ reads

$$\frac{d^2}{dx^2}\phi = -\frac{e(n_i - n_e)}{\epsilon_0} \tag{2.1}$$

with electron density n_e and ion density n_i. For infinitely heavy ions (the ions do not move significantly due to their large mass) the electron density obeys the Boltzmann distribution $n_e = n_{e,0}\exp(e\phi/k_B T_e)$ where $n_{e,0}$ equals the ion density at infinity and T_e[1] is the electron temperature. Substituting the electron density into 2.1 and expanding the exponential for $e\phi \ll k_B T_e$ leads to

$$\frac{d^2}{dx^2}\phi = \frac{n_{e,0}e^2}{\epsilon_0 k_B T_e}\phi. \tag{2.2}$$

[1] In plasma physics it is customary to express the temperature of a plasma in units of energy, keV or MeV.

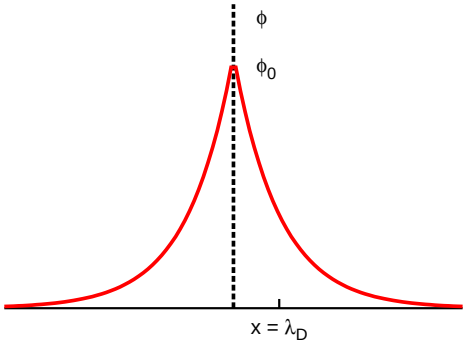

Figure 2.1: Shielding of an electric potential at $x = 0$ in one dimension. The potential decreases exponentially on the scale length λ_D.

The solution is an exponentially decreasing potential $\phi = \phi_0 \exp(-|x|/\lambda_D)$ with the characteristic length

$$\lambda_D = \sqrt{\frac{\epsilon_0 k_B T_e}{n_{e,0} e^2}}. \tag{2.3}$$

The above derivation is only valid if there are enough particles in the Debye sheath, i.e. the *plasma parameter*, $N_D = 4/3\pi\lambda_D^3 n$, which represents the number of particles in the Debye sphere, is much larger than one.

2.1.2 Plasma frequency

If the electrons are moved from their equilibrium position an electromagnetic reset force draws the electrons back to balance the charge of the ions. To determine the corresponding plasma frequency a fixed ion background and small oscillations are assumed. Considering a slab displaced by δx which carries an areal charge density of $\sigma = e n_e \delta x$ obeys the equation of motion

$$m_e \frac{d^2}{dt^2}\delta x = -\frac{e^2 n_e}{\epsilon_0}\delta x \tag{2.4}$$

with the electron mass m_e. This equation describes harmonic oscillations with the *plasma frequency*

$$\omega_p^2 = \frac{n_e e^2}{\epsilon_0 m_e}. \tag{2.5}$$

2.1.3 Critical density

To describe an electromagnetic wave with wave vector $\mathbf{k}$ and frequency ω propagating in a plasma the Maxwell equations have to be solved. Due to the high frequency of the

waves the ions are supposed to be infinitely heavy. Assuming a dependence of the fields and the current on $\exp(i(\mathbf{kr} - \omega t))$ the dispersion relation yields

$$\omega^2 = \omega_p^2 + c^2 k^2. \tag{2.6}$$

The vacuum relation is modified by the term ω_p^2 which introduces a cut-off plasma frequency where the wave vector k becomes imaginary. This means that the electromagnetic wave cannot propagate into the plasma anymore but decreases exponentially. For a given frequency ω_0 and wavelength λ of an electromagnetic wave this cut-off arises at the *critical density*

$$n_c = \frac{\omega_0^2 \epsilon_0 m_e}{e^2} \tag{2.7}$$

$$= \frac{1.1 \times 10^{21}}{\lambda^2/\mu\mathrm{m}^2} \frac{1}{\mathrm{cm}^3}. \tag{2.8}$$

It defines the regimes of overcritical plasmas which are opaque for light waves and undercritical plasmas which are transparent.

2.1.4 Collisions

A plasma created by the interaction of a high intensity laser with a solid or gas target can be considered as *collisionless*. This can be deduced from the frequencies of [19]

- electron-ion collisions,

$$\langle \nu_{ei} \rangle = \sqrt{\frac{2}{\pi^{3/2} m_e T_e^3}} \frac{n_i Z^2 e^4 \ln \Lambda}{12 \epsilon_0^2}, \tag{2.9}$$

- electron-electron collisions,

$$\langle \nu_{ee} \rangle \sim \frac{n_e e^4 \ln \Lambda}{\epsilon_0^2 \sqrt{m_e T_e^3}} \sim \frac{n_e \langle \nu_{ei} \rangle}{n_i Z^2}, \tag{2.10}$$

- and ion-ion collisions,

$$\langle \nu_{ii} \rangle = \sqrt{\frac{1}{\pi^3 m_i T_i^3}} \frac{n_i Z^4 e^4 \ln \Lambda}{12 \epsilon_0^2} \approx \sqrt{\frac{m_e}{m_i}} \langle \nu_{ei} \rangle, \tag{2.11}$$

with $\Lambda \approx (12\pi/Z) n \lambda_d^3$. For a hydrogen plasma with density n (in $1/\mathrm{cm}^3$) and temperature T_e (in keV) the largest collision frequency is

$$\langle \nu_{ei} \rangle \approx \langle \nu_{ee} \rangle \approx \frac{5 \cdot 10^{-14} n}{T_e^{3/2}} \frac{1}{s}. \tag{2.12}$$

For $T_e \gg 0.1$ keV this frequency is much smaller than the corresponding plasma frequency ω_p of under- ($\sim 10^{19}$ $1/\mathrm{cm}^3$) or overcritical ($\sim 10^{21}$ $1/\mathrm{cm}^3$) laser-plasmas. Because typical electron temperatures in laser induced plasmas are much larger than 0.1 keV one can consider these plasmas as *collisionless*.

2.1.5 Ponderomotive force

When a high intensity laser interacts with charged particles the so called *ponderomotive force* pushes them out of regions with high intensities in the direction of the intensity gradient. A descriptive derivation of the ponderomotive force is given in [20]. An electron which experiences the fields of an electro-magnetic wave (frequency ω_0, electric field amplitude $E_{x,0}$) oscillates in the transverse direction of the laser propagation. In the classical case, when the magnetic field can be neglected, the oscillation energy of the electron yields

$$W_{osc} = \frac{1}{2} m_e < v^2 >= \frac{e^2}{4 m_e \omega_0^2} E_{x,0}^2. \tag{2.13}$$

When the amplitude of the electric field is varying in space, the oscillating energy of the electron also changes. As a free electron can neither emit nor absorb photons (it can only scatter them), the change in energy leads to an in- or decrease in the kinetic energy. The total energy $W_{tot} = W_{kin} + W_{osc}$ remains of course constant. Hence the electron feels the *ponderomotive force*

$$\mathbf{F}_{pond} = -\nabla \phi_{pond} = -\frac{e^2}{2 m_e \omega_0^2 c \epsilon_0} \nabla I \tag{2.14}$$

with the *ponderomotive potential*

$$\phi_{pond} = W_{osc} = \frac{e^2}{4 m_e \omega_0^2} E_{x,0}^2. \tag{2.15}$$

The force pushes the electrons towards regions of lower intensities. This feature holds also in the relativistic regime [21]. The energy of an electron oscillating in transverse direction and hence the *ponderomotive potential* is given by [22]

$$\phi_{pond} = \left(\sqrt{1 + a_0^2} - 1 \right) m_e c^2. \tag{2.16}$$

with the normalized vector potential (cf. equation 2.19) $a_0 = 0.85 \lambda / \mu\mathrm{m} \sqrt{I_0 / 10^{18} W/cm^2}$ corresponding to the classical velocity of electrons oscillating in the transverse electric field of an electro-magnetic wave.

2.1.6 Plasma creation

In the electric field of the pedestal (the so called pre-pulse which is described in section 2.2.2) of a high-intensity laser atoms are instantaneously ionized. For different intensity regimes diverse ionization processes are dominant [23]. Keldysh's model [24, 25] distinguishes three regimes for simple atoms only. But numerical simulations as well as analytical approaches show that these regimes are still dominant for plasma creation in solid states.

For comparatively low intensities ($I > 10^{10} W/cm^2$) *multi-photon ionization* is predominant. An electron absorbs multiple photons before reaching an unbound state.

For higher intensities, $I > 10^{14} W/cm^2$, the Coulomb barrier is suppressed. This establishes the possibility of tunneling the potential wall. This phenomenon is called *tunnel ionization*.

For even higher intensities the Coulomb barrier is further suppressed. The electrons are liberated by the so-called *barrier suppression ionization*.

The intensities of lasers used for particle acceleration by laser-plasma accelerators exceed $10^{17} W/cm^2$ and are accompanied by the so-called *pre-pulse* (see section 2.2.2) whose intensity is $10^5 - 10^{10}$ orders of magnitudes lower. These intensities are sufficient for instantaneously creating a plasma. Subsequently the main pulse is interacting with a plasma and provides the possibility of creating energetic particle beams.

2.1.7 Electron heating

When a laser interacts with a plasma, energy is absorbed. Electro-magnetic energy is partially transformed into kinetic energy, mainly into the one of electrons. Various mechanisms contribute to the absorption depending on laser parameters and experimental geometries. Because in this work absorption mechanisms are not studied in detail only a very short overview on electron heating is given.

For moderate intensities, which appear e.g. under pre-pulse conditions (cf. section 2.2.2), collisional absorption by inverse bremsstrahlung [26], the anomalous skin effect [27] and sheath inverse bremsstrahlung [28] participate in the absorption process.

As in the following phenomena of lasers with high intensities interacting with plasmas are studied, only the dominant mechanism of laser absorption in this regime is described in more detail. The central mechanism is ponderomotive heating. Electrons are expelled from high intensity regions by the ponderomotive force which is proportional to the intensity gradient (equation 2.14). At the critical density - where the laser light is reflected - large intensity gradients occur and electrons are accelerated to relativistic energies. Simulations [29] showed that the temperature of the heated electrons scales with the ponderomotive potential,

$$k_B T_e \approx \phi_p = m_e c^2 \left(\sqrt{1 + a_0^2} - 1 \right). \tag{2.17}$$

This scaling is in good agreement with later experimental results [30].

For oblique incident lasers two other mechanisms contribute to absorption. In the case of vacuum heating [31] the part of the oscillating electric field which is normal to the target surface (E_x) can accelerate electrons into vacuum. As inside the target the electric fields vanish, a returning electron feels no decelerating force. It penetrates inside the target with relativistic energy.

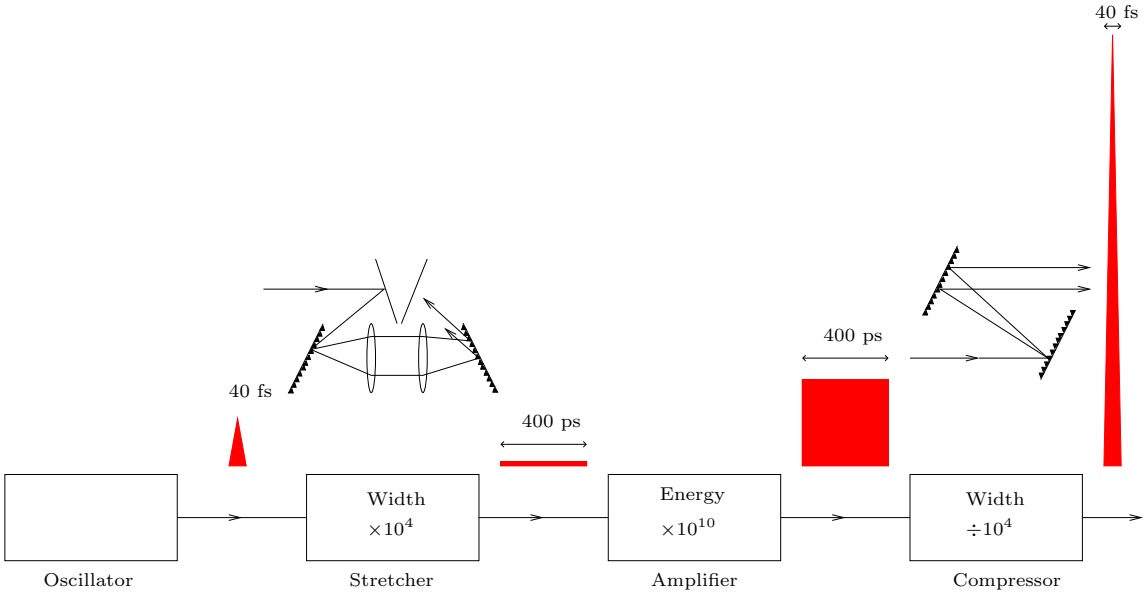

Figure 2.2: Chirped pulse amplification: The pulse provided by the oscillator with a pulse length of 40 fs and an energy of a few nJ is stretched by two opposed gratings where the red wave lengths are crossing the stretcher faster than the blue ones. Then the pulse is amplified by a factor 10^{10}. After the recompression to the original length by two parallel gratings the final pulse yields an energy of a few Joule.

The so-called resonant absorption [32] occurs at the critical density. At this point the frequency of an electron oscillating in the electro-magnetic wave matches the plasma frequency and resonance phenomena arise.

2.2 Laser basics

2.2.1 Chirped pulse amplification

The invention of the Chirped Pulse Amplification (CPA) method [33, 34] provided the possibility to reach laser intensities as they are used in present experiments. Before that, an increase in laser intensity was limited by non-linear effects. At intensities of the order of GW/cm^2 the material index of refraction becomes linearly dependent on the intensity. Therefore a laser with a Gaussian intensity profile sees different refraction indices and the beam quality decreases significantly. The CPA (figure 2.2) avoids this problem by stretching the basic laser pulse in time, then amplifying it and performing a recompression at the end. The pulse is stretched by two opposed gratings by a factor of $10^3 - 10^5$. The positive group velocity dispersion leads to a temporal spread of the frequency components. The resulting pulse intensity is decreased and amplification is

possible. After the amplification of $\sim 10^{10}$ the pulse is recompressed by another pair of gratings. Typical laser parameters achieved by these systems are (e.g. the "Salle jaune" laser of the LOA [35])

- laser energy, $E_{las} \sim 0.8$ J,
- pulse length, $\tau_{las} \sim 30$ fs,
- intensity in a focal spot with a diameter of a few microns, $I \sim 6 \times 10^{19} W/cm^2$,
- laser wavelength, $\lambda = 820$ nm, and
- repetition rate, $f = 10$ Hz.

Even higher intensities of the order of $4 \times 10^{20} W/cm^2$ have been achieved [36] with CPA lasers.

2.2.2 Pre-pulse

An important property of these ultra-short high-intensity lasers is the so-called "pre-pulse". Amplified spontaneous emissions (ASE) in the amplifier lead to a laser pulse accompanying the main pulse on a nanosecond time scale. The contrast between the main pulse with peak intensity and the pre-pulse is between 10^5 and 10^{10}. As the electric fields of the pre-pulse are still large enough to ionize the target a "pre-plasma" is created. The length of the pre-pulse and the contrast to the main pulse are of course influencing the pre-plasma properties, temperature and density gradient, and hence the absorption of the main pulse [37].

2.2.3 Laser parameters

To characterize the laser intensity the dimensionless normalized vector potential a_0 is introduced. An electron oscillating classically in the transversal electric field of an electro-magnetic wave yields a maximum velocity of $v_\perp = eE_{x,0}/m_e\omega_0$. In addition the normalized vector potential

$$a_0 = \frac{v_\perp}{c} = \sqrt{\frac{e^2 I_0 \lambda^2}{2\pi^2 c^5 \epsilon_0 m_e^2}} \tag{2.18}$$

$$= 0.85\sqrt{I_{18}\lambda(\mu\mathrm{m})^2} \tag{2.19}$$

gives a criterion for the relativistic regime (I_{18} in $10^{18} W/cm^2$, $\lambda(\mu\mathrm{m})$ in μm). For $a_0 \gtrsim 1$ the transversal velocity approaches c and the $\mathbf{v} \times \mathbf{B}$ part of the Lorentz force has to be taken into account. Besides a_0, the energy E_{las}, the pulse length τ_{las} and the wave length λ characterize the laser.

2.3 Particle in cell simulations

The simplest way to study plasma phenomena would be to solve the equation of motion for every single particle numerically. An overcritical plasma of 10 μm^3 volume with an electron density of $n_e \sim 10^{21}$ cm^3 consists of $\sim 10^{11}$ particles. The resolution in time should resolve the plasma frequency with $t_{pe} \sim 1$ fs. Hence a simulation of 1 ps takes $\sim 10^{14}$ iterations. Assuming a computation time of 1 μs per iteration would lead to a total simulation time of several years.

2.3.1 Kinetic theory and Vlasov equation

However in kinetic theory for plasmas (e.g. [18]) it is only necessary to know the distribution function $f_\alpha(\mathbf{x}, \mathbf{p}, t)$ of a particle species α. The number of particles dN in the phase space volume $d\Gamma = d\mathbf{x}d\mathbf{p}$ around position $\mathbf{x}$ and momentum $\mathbf{p}$ is given by $dN = f_\alpha d\mathbf{x}d\mathbf{p}$. The distribution function has to satisfy the Boltzmann equation

$$\partial_t f_\alpha + \mathbf{v}\nabla_\mathbf{x} f_\alpha + \mathbf{F}\nabla_\mathbf{p} f_\alpha = (\partial_t f_\alpha)_{coll}, \tag{2.20}$$

where the term on the right hand side describes collisions between particles. In a sufficiently hot plasma collisions can be neglected (see section 2.1.4), the collision term becomes zero and the force $\mathbf{F}$ is entirely electromagnetic. The equation results in the *Vlasov equation*

$$\partial_t f_\alpha + \mathbf{v}\nabla_\mathbf{x} f_\alpha + q(\mathbf{E} + \mathbf{v} \times \mathbf{B})\nabla_\mathbf{p} f_\alpha = 0. \tag{2.21}$$

In Particle in Cell (PIC) simulations [38] this equation is not solved directly but by the method of characteristics. The distribution function is represented by a number of macro-particles and for each particle the equations of motion

$$\frac{\mathrm{d}\mathbf{p}}{\mathrm{dt}} = q(\mathbf{E} + \mathbf{v} \times \mathbf{B}), \tag{2.22}$$

$$\frac{\mathrm{d}\mathbf{x}}{\mathrm{dt}} = \mathbf{p}/m, \tag{2.23}$$

with $m = \gamma m_0$, $\gamma = 1/\sqrt{1 - v^2/c^2}$ are solved.

2.3.2 Weighting and computational cycle

To determine the electric and magnetic fields a spatial grid is introduced. The particles are accumulated by an interpolation scheme on the grid points resulting in a charge and current density on the nodes. The first-order weighting scheme in one dimension (figure 2.3) assigns a particle to the two nearest grid points. The charge and therefore the current are split linearly depending on the distance to the nodes.

Then Maxwell's equations can be solved on the spatial grid assuming specific, e.g. periodic, boundary conditions. The obtained self-consistent electromagnetic fields are

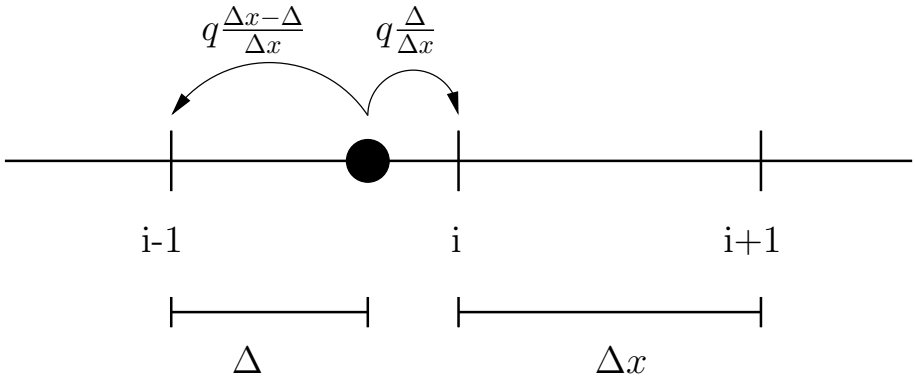

Figure 2.3: A particle is assigned to the two nearest grid points. $(\Delta x - \Delta)/\Delta x$ of the particle charge contributes to the $(i-1)$th grid point. $\Delta/\Delta x$ is attached to the ith node.

interpolated to the particle positions and the equation of motion for each macro-particle can be solved. The full computational cycle is shown in figure 2.4.

2.3.3 "Natural" units

For convenience the physical quantities are transformed to dimensionless variables so that Maxwell's equations read

$$\nabla' \mathbf{E}' = \rho' \tag{2.24}$$
$$\nabla' \times \mathbf{E}' = -\partial_{t'} \mathbf{B}' \tag{2.25}$$
$$\nabla' \mathbf{B}' = 0 \tag{2.26}$$
$$\nabla' \times \mathbf{B}' = \mathbf{j}' + \partial_{t'} \mathbf{E}' \tag{2.27}$$

with the dimensionless variables given in table 2.1.

Due to the dimensionless variables one simulation represents various physical situations. A common simulation set-up with laser intensity $a_0 = 3.7$, laser pulse length $\tau_{las} = 200\ 1/\omega_0$, target thickness $d = 30\ c/\omega_0$ and plasma density $n = 10\ n_c$ represents:

- for $\lambda = 1\ \mu$m a laser of $1.9 \cdot 10^{19} W/cm^2$ and $\tau_{las} = 106$ fs incident on a 4.8 μm thick target at $1.1 \cdot 10^{22}$ cm^3 or
- for $\lambda = 0.5\ \mu$m a laser of $7.6 \cdot 10^{19} W/cm^2$ and $\tau_{las} = 53$ fs incident on a 2.4 μm thick target at $4.4 \cdot 10^{22}$ cm^3.

In the following almost exclusively "natural" units are used and from time to time examples in SI-units are given.

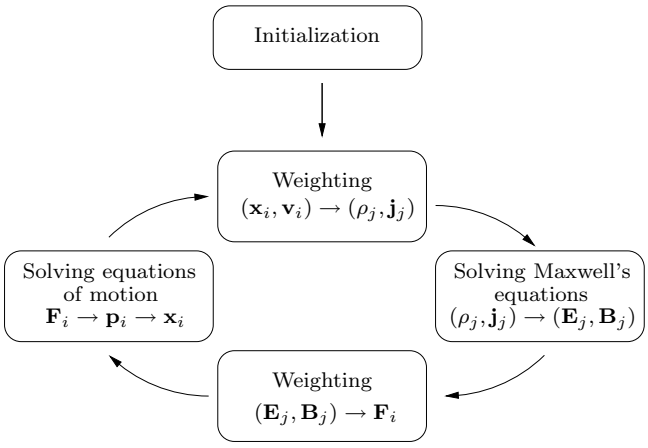

Figure 2.4: After the initialization the computational loop starts. The particles are assigned to the spatial grid. With the resulting charge and current densities the Maxwell equations are solved. The fields are interpolated to the particles positions and the equations of motion are solved for each particle.

2.3.4 Diagnostics

To analyze the simulation various means of diagnostics are available. As these occur in the simulations on laser-accelerated protons (part I) a detailed description is set aside. In general there are two different types of diagnostics. On the one hand there are "time histories" like the total energy, kinetic energies of each particle species or the fraction of absorption of an incident laser pulse. On the other hand periodic snapshots of the system are stored. These are e.g. the xp_x-phase space, energy distribution of a particle species or the electric field at a certain time.

Physical quantity	Dimensionless variable	Units in SI-units($\lambda = 1$ μm)
Distance	$\mathbf{x}' = \mathbf{x}/(c/\omega_0)$	0.159 μm
Time	$t' = t/(1/\omega_0)$	0.531 fs
Velocity	$\mathbf{v}' = \mathbf{v}/c$	$3 \cdot 10^8$ m/s
Mass	$m' = m/m_e$	$9.1 \cdot 10^{-31}$ kg
Momentum	$\mathbf{p}' = \mathbf{p}/(m_e c)$	$2.73 \cdot 10^{-22}$ kg$\cdot$ m/s
Density	$n' = n/n_c$	$1.1 \cdot 10^{21}$ 1/cm^3
Electric field	$\mathbf{E}' = \mathbf{E}/(m_e c\omega_0/e)$	3.2 TV/m
Magnetic field	$\mathbf{B}' = \mathbf{B}/(m_e\omega_0/e)$	10.7 kT

Table 2.1: Simulation units

2.3.5 Choice of initial values

One important issue occurring in PIC simulations are of course numerical instabilities. E.g. if the choice of the grid size Δx, the time step Δt or the number of initialized particles per cell (NPC) is inappropriate, numerical heating can develop. This could appear if non-physical forces due to the grid occur or the time step does not resolve the largest frequency of a physical phenomenon. As a guideline [39] the following initial values are chosen:

- the size of a grid cell is chosen to be $\Delta x \leq \lambda_D$,
- the time step is chosen to be $\Delta t \leq \Delta x/\sqrt{2}$
- the number of particles per cell is chosen to be $NPC \geq 100$ for one-dimensional simulations

If a numerical instability occurred in a simulation, the parameters were varied by trial and error. The main criterion was to ensure the conservation of the total energy.

2.3.6 PIC codes

In this work two different PIC codes are used. In chapter 4 one-dimensional plasma expansions are investigated with a self-developed one-dimensional, electro-static PIC code. All other simulations are performed with *Calder*, an electro-magnetic, fully relativistic PIC code [16] which was made available by Erik Lefebvre from the Département de physique théorique et appliquée at the Commissariat à l'Énergie Atomique (CEA), Bruyères le Châtel, France.

Part I

PROTONS

3 Basics of proton acceleration

3.1 Basic mechanisms

In the interaction of a high-intensity laser with a solid target energetic protons are produced. At first the two main acceleration mechanisms are described. On the one hand an acceleration of protons at the target front surface is present where ponderomotively expelled electrons leave a positively charged cavity behind. On the other side electrons crossing the target form an electric sheath at the rear side leading to an acceleration of protons at the back of the target.

Both mechanisms occur when a laser with an intensity $I_0 \gtrsim 10^{18} W/cm^2$ is focused e.g. onto an aluminum foil with a typical thickness between a few and 100 μm (figure 3.1). The accompanying pre-pulse already ionizes the target surface (by definition the front side) and creates the so-called pre-plasma.

3.1.1 Target front side acceleration mechanism

The target front side acceleration is based on ponderomotively expelled electrons. The resulting electrostatic field accelerates the target surface into the target, called the "hole-boring" mechanism [40, 29, 41]. Sentoku *et al.* [42] studied the phenomenon by means of one-dimensional PIC-simulations. In front of the target a pre-plasma is assumed. When the high-intensity laser reaches the critical density electrons are expelled out of the high intensity region. This process lasts until the ponderomotive potential equals the arising electric potential, $\Phi_{el} \sim \Phi_{pond}$. The existence of this field is limited to the laser pulse duration, τ_{las}. As the acceleration time for the protons in the field, τ_{acc}, is shorter than τ_{las} [43], the protons can gain the maximum energy determined by the ponderomotive potential. In addition simulations show that the accelerated sharp proton front explodes due to repulsive forces leading to an additional acceleration. The maximum energy for protons originating at the target front is estimated to [43]

$$E_{p,front} \sim 2.25 k_B T_e = 1.15 \text{ MeV} \left(\sqrt{1 + a_0^2} - 1 \right). \tag{3.1}$$

For typical intensities of $I = 10^{19} W/cm^2$ the estimation predicts a proton energy of $E_{p,front} \sim 2.1$ MeV.

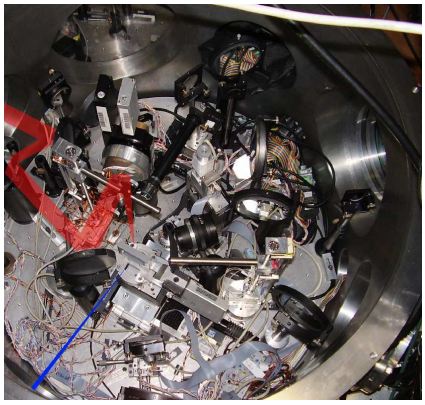

Figure 3.1: [1]Inside the interaction chamber the laser is directed by several mirrors onto an off-axis parabola. This focuses the beam onto the target leading to intensities of up to $10^{19} - 10^{20} W/cm^2$. Due to the formation of an electron sheath at the rear surface protons are accelerated normal to the target rear side.

3.1.2 TNSA mechanism at the rear side

In the interaction of a high-intensity laser with a solid target electrons are heated. Depending on the intensity temperatures of around 1 MeV are obtained (section 2.1.7). Due to their large energies electrons can penetrate through the target and leave it on the back side forming an electron sheath. The corresponding electric field of this sheath, which can reach several TV/m, ionizes parasitic hydrogen atoms stemming from contamination layers at the target back. Afterwards these protons are accelerated normal to the target surface to energies of several MeV (figure 3.2). This mechanism which is dominant in the acceleration of protons is the so-called *Target Normal Sheath Acceleration*

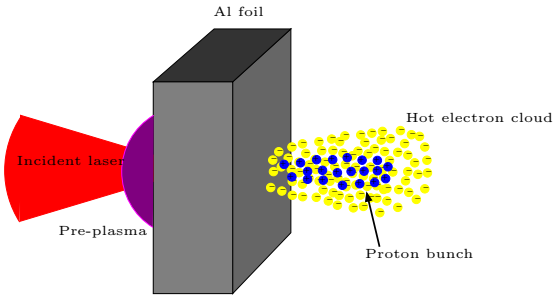

Figure 3.2: The incident laser heats electrons which form a sheath at the rear side. Parasitic protons are accelerated normal to the target surface to energies of several MeV.

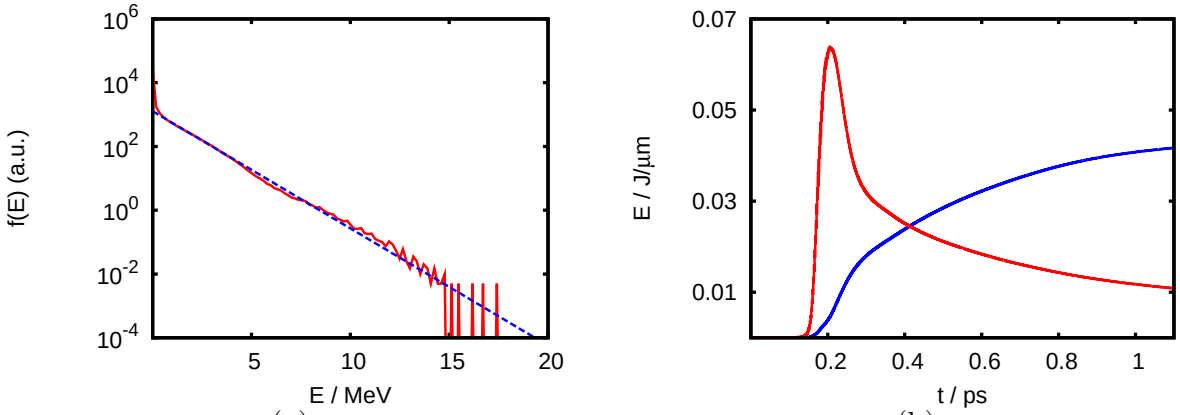

(a) (b)

Figure 3.3: (a) Electron energy spectrum shortly after the arrival of the maximum of the laser pulse at the target surface. The electron temperature is 1.1 MeV (dashed line). (b) Kinetic energy of electrons (red) and protons (blue) versus time.

(TNSA) [29, 44].

However the acceleration field is not homogeneous for all protons at the rear side. At first due to the lateral inhomogeneity of the electron sheath the field is varying. Secondly protons, which are not directly placed at the target surface, experience a reduced acceleration field as the electric field is shielded by the outer protons. The resulting energy spectrum yields a Maxwellian shape with a characteristic cut-off energy (see figure (3.5 (b)) and section 3.2 for the underlying basic model).

For a long time experimental results provided a foundation for controversy on the origin of the protons, the target front or rear side. While several groups proposed a dominant front side acceleration mechanism [45, 46] other groups [2, 47, 48, 44] suggest the rear side as the origin of the fastest protons. In the meantime the fastest protons are supposed to stem from the rear side [49]. However for high laser intensities the front side acceleration mechanism might become more dominant [39].

3.1.3 Exemplary two-dimensional simulation

To illustrate the proton acceleration process in more detail an exemplary two-dimensional PIC simulation is performed. A laser with an intensity of $I = 10^{20} W/cm^2$, a pulse duration of $\tau_{las} = 36$ fs and a transversal size of $l_{y,FWHM} = 5$ μm is incident on a 3.5 μm thick plasma slab. The target consists of electrons and protons with a density

[1]By the courtesy of the Groupe Sources de Particules par Laser, Laboratoire d'Optique Appliqée, CNRS, ENSTA, Palaiseau, France

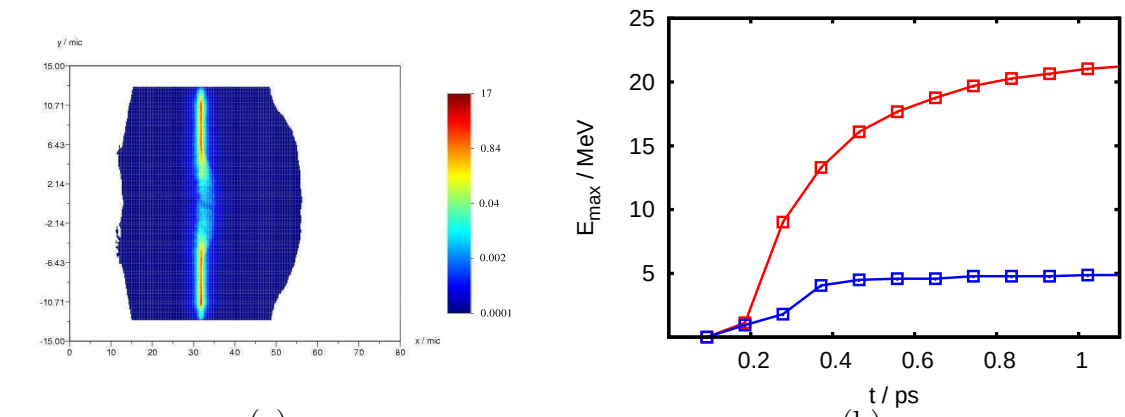

(a) (b)

Figure 3.4: (a) Proton density map at 0.5 ps after the laser pulse has hit the target. The density is given in units of the critical density. (b) Maximum energy of protons propagating in laser direction which are originating from the target front (blue) and rear (red) side respectively versus time.

of $n = 10\ n_c$ and is placed at $x = 32\ \mu$m.

The simulation box with a dimension of 100 μm in longitudinal and 25 μm in transversal direction is divided into cells with side length $\Delta x = \Delta y = 16$ nm. The simulation is lasting for 1.1 ps ($\Delta t = 0.037$ fs).

About 30% of the laser energy is absorbed by the plasma. The electrons are heated and show a Maxwellian energy distribution with $T_e \sim 1$ MeV shortly after the arrival of the maximum of the laser pulse at the target surface (figure 3.3 (a)). The electrons form an electric sheath at the target front and rear side and protons are accelerated (figure 3.4 (a)). In the course of time more and more kinetic energy of the electrons is transferred to the protons via the electromagnetic forces (figure 3.3 (b)). At the end of the simulation, i.e. after 1.1 ps approximately 80% of the kinetic energy is stored in the kinetic energy of the protons.

Figure 3.4 (b) shows the temporal development of the maximum energies of the protons originating from the target front respectively the target rear side. The rear side acceleration is leading to larger proton energies compared to the energy of front side protons.

The xp_x-phase space also shows the two different acceleration mechanisms (figure 3.5 (a)). At the rear side the acceleration is based on the expansion of the target due to heated electrons. This expansion has a counterpart on the front side as of course the expansion takes also place in the backward direction, i.e. in the direction of the laser source. In addition at the front side forward accelerated protons are present. However their momentum is smaller compared to the one of the rear side protons.

3.1.4 Experimental results

As in chapter 5 an extensive number of experiments is compared to a model scaling the maximum energy, here just three exemplary experiments are presented. At the LOA protons with energies of up to 10 MeV were generated [35]. A "table-top" laser which provides a laser pulse of $\sim$ 1 J in $\sim$ 40 fs is focused onto plastic or aluminum foils (thickness ~ 6 μm) leading to intensities of up to $6 \times 10^{19} W/cm^2$. The energy spectrum shows the typical Maxwellian shape with a sharp cut-off at 10 MeV. The divergence angle is around 15° at FWHM for 5 MeV protons.

Hegelich *et al.* [12] suppressed the dominant acceleration of parasitic protons by resistive heating. The laser ($I \sim 5 \times 10^{19} W/cm^2$, $\tau_{las} \sim 500$ fs) interacts with a 50 μm aluminum foil coated with a 1 μm carbon layer at the rear side. When the target is resistively heated the maximum proton energy is reduced from 25 MeV to 3 MeV and their number is reduced by a factor of 10. On the other hand the maximum carbon ion energy (up to 5 MeV/nucleon) and the number of accelerated ions (by a factor of 2.5) are increased.

The highest proton energy reported so far was achieved by Snavely *et al.* [2]. Focusing a $\sim$ 400 J, 500 fs laser, i.e. an intensity of $3 \times 10^{20} W/cm^2$, onto a 100 μm thick CH foil yielded proton energies of up to 58 MeV.

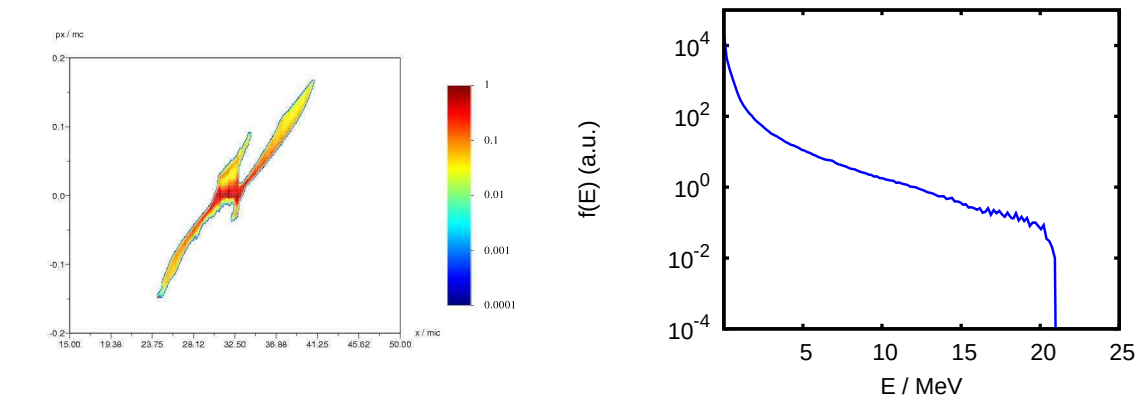

(a) (b)

Figure 3.5: (a) Phase space of protons in arbitrary units at 0.2 ps after laser pulse has reached the target surface in arbitrary units. Protons with positive momenta propagate in the laser direction and are originating from the front as well as from the rear side. Protons from the front with negative momenta propagate in the direction of the laser origin. In experiments the corresponding energies are lower as the pre-plasma (which is neglected in the simulations) changes the density gradient at the front. (b) A typical energy spectrum of laser-accelerated protons.

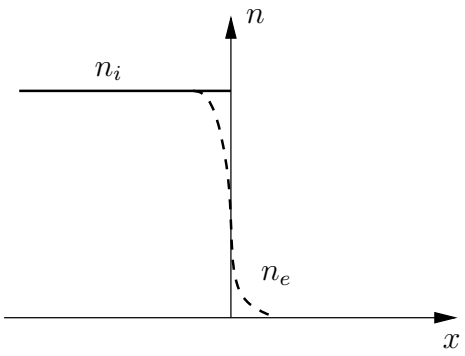

Figure 3.6: Initial situation of the one-dimensional plasma expansion. The ions are at rest and the electrons obey a Boltzmann distribution with a temperature T_e.

3.2 Mora's model

The TNSA mechanism is based on the heating of electrons by the laser-plasma interaction and a following plasma expansion. Mora [50] developed a one-dimensional analytical model of the expansion of a plasma. Though in laser-plasma experiments several underlying conditions of the model (i.e. isothermal expansion, the plasma is filling the negative half space) are not fulfilled, it provides a good insight into the acceleration process.

At $t = 0$ the negative half space is filled with cold ions at a constant density n_i. The electrons are initialized with temperature T_e and obey the Boltzmann distribution (figure 3.6)

$$n_e = n_{e0} \exp(e\phi/k_B T_e). \tag{3.2}$$

The potential ϕ satisfies the Poisson equation $\partial_x^2 \phi = e(n_e - Z n_i)/\epsilon_0$. To determine the initial electric field at the ion front Poisson's equation is integrated from the position of the ion front, x_f, to infinity (appendix A.1).

$$E_{x,front} = \sqrt{\frac{2}{\exp(1)}} E_{x,0} \tag{3.3}$$

with $E_{x,0} = \sqrt{n_{e0} k_B T_e/\epsilon_0}$. Additionally the electric field for positive x is given by (appendix A.2)

$$E_x(x \geq 0, t = 0) = \sqrt{\frac{2}{\exp(1)}} E_{x,0} \frac{1}{1 + x/\sqrt{2\exp(1)}\lambda_D} \tag{3.4}$$

After initialization the system develops under the equations of continuity and motion. The electrons are still assumed to be in equilibrium with the potential ϕ.

$$(\partial_t + v_i \partial_x)\, n_i = -n_i \partial_x v_i, \tag{3.5}$$

$$(\partial_t + v_i \partial_x)\, v_i = -\frac{Ze}{m_i} \partial_x \phi. \tag{3.6}$$

When one assumes quasi-neutrality, $n_e = Zn_i$, one obtains the self-similar solution (valid for $x + c_s t > 0$)

$$n_e = n_{e0} \exp\left(-\frac{x}{c_s t} - 1\right), \tag{3.7}$$

$$v_i = c_s + \frac{x}{t} \tag{3.8}$$

with the ion-acoustic velocity $c_s = \sqrt{Zk_B T_e/m_i}$ and the ion plasma frequency $\omega_{pi} = \sqrt{n_{e0} Ze^2/m_i \epsilon_0}$. Substituting equation (3.7) into equation (3.2) yields a constant electric field between $x = -c_s t$ and the plasma edge,

$$E_{x,ss} = \frac{E_{x,0}}{\omega_{pi} t}. \tag{3.9}$$

The self-similar solution is valid as long as the local Debye length λ_D is much smaller than the scale length of the self similar solution $c_s t$, i.e. $\lambda_D \ll c_s t$ or $\omega_{pi} t \gg 1$. The equality of these two quantities leads to the breakdown of the above approximation and gives a rough estimation of the ion front position and therefore for the ion front velocity,

$$x_{front} = c_s t(2\ln(\omega_{pi} t) - 1) \tag{3.10}$$

$$v_{front} = 2c_s \ln(\omega_{pi} t). \tag{3.11}$$

This implies that the electric field is

$$E_{x,front} = 2\frac{E_{x,i}}{\omega_{pi} t} = 2E_{x,ss}, \tag{3.12}$$

i.e. two times the electric field of the self similar solution.

In addition the self-similar model provides an expression for the ion energy spectrum. Starting from equations (3.7) and (3.8) one obtains (appendix A.3)

$$\frac{dN}{dE} = \frac{n_{i0} c_s t}{\sqrt{2EE_0}} \exp\left(-\sqrt{\frac{2E}{E_0}}\right) \tag{3.13}$$

with $E_0 = Zk_B T_e$. The energy spectrum shows an Maxwellian shape which is typical of laser-plasma experiments.

To determine the maximum cut-off energy at a given expansion time Mora solved equations (3.5) and (3.6) numerically and obtained for the electric field at the ion front

$$E_{x,front} \simeq \frac{2E_{x,i0}}{\sqrt{2\exp(1) + \omega_{pi}^2 t^2}}. \tag{3.14}$$

This fit shows the correct behavior for $t = 0$ and $\omega_{pi}t \gg 1$ (compare to (3.3) and (3.9) respectively). Integrating the electric field results in the ion front velocity

$$v_{front} = 2c_s \ln\left(\tau + \sqrt{\tau^2 + 1}\right) \tag{3.15}$$

with $\tau = \omega_{pi}t/\sqrt{2\exp(1)}$ and therefore the maximum ion energy

$$E_{max} = \frac{1}{2}m_i v_{front}^2 = 2Zk_BT_e\left[\ln\left(\tau + \sqrt{\tau^2 + 1}\right)\right]^2. \tag{3.16}$$

Summing up the analytical model of an one-dimensional isothermal plasma expansion gives expressions for the energy spectrum as well as for the maximum cut-off energy. Recently Mora [51] extended the model by an adiabatic version which will be shortly discussed in chapter 4. In the next section the relation of the model to laser-accelerated protons is given.

3.3 Scaling laws for laser-accelerated protons

3.3.1 Analytical model

J. Fuchs *et al.* [52] developed an analytical model to describe the scaling of the maximum kinetic energy achievable with laser-accelerated protons. The basis of this analysis is the one-dimensional plasma expansion model of Mora [50] for a plasma with initially cold ions and hot electrons with temperature T_e (section 3.2). The plasma expansion model gives an expression for the maximum energy (equation 3.16),

$$E_{max} = 2Zk_BT_e\left[\ln\left(\tau + \sqrt{\tau^2 + 1}\right)\right]^2, \tag{3.17}$$

with $\tau = \omega_{pi}t/\sqrt{2\exp(1)}$ and $\omega_{pi} = \sqrt{n_{e0}Ze^2/m_i\epsilon_0}$. Hence the maximum energy depends on the hot electron temperature T_e, hot electron density n_{e0}, and the expansion time t:

$$E_{max} = E_{max}(T_e, n_{e0}, t). \tag{3.18}$$

As these parameters cannot be controlled directly by the experimental set-up, they have to be linked to the experimental parameters. These are the intensity I_0, the laser wavelength λ, the laser pulse length τ_{las}, the spot size diameter d_0 and the target thickness d.

Hot electron temperature T_e

Wilks *et al.* showed that the hot electron temperature can be estimated by the ponderomotive potential [29, 47]

$$k_BT_e \sim \Phi_{pond} \tag{3.19}$$

$$= m_ec^2\left[\sqrt{1 + I_{18}\lambda_{\mu m}/1.37} - 1\right] \tag{3.20}$$

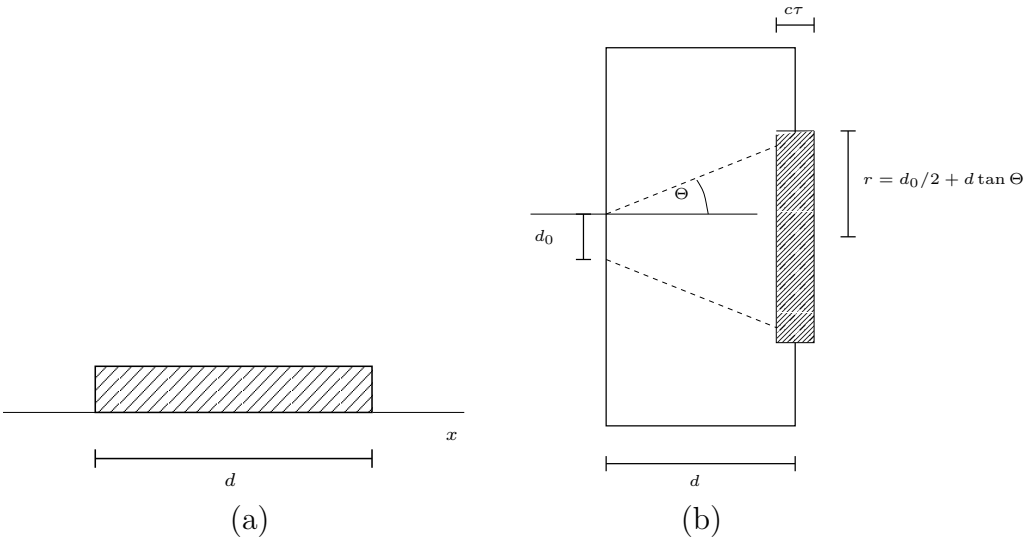

Figure 3.7: The volume over which the hot electrons spread in one (a) respectively two and three (b) dimensions.

where the intensity I_{18} is given in $10^{18} W/cm^2$ and the wave length $\lambda_{\mu m}$ in μm. Thus the hot electron temperature is depending only on laser intensity and wavelength, $T_e = T_e(I, \lambda)$.

Hot electron density n_{e0}

The hot electron density is computed by assuming that the created hot electrons spread homogeneously through the target. Since in the following both one- and two-dimensional simulations as well as data from experiments, i.e. three-dimensional situations, are considered, the corresponding volume has to be computed differently in each case (cf. figure 3.7).

1D simulations: In one dimension the volume is simply the target thickness d. If the thickness is larger than the length of the created electron bunch $c\tau_{las}$ the volume is confined to this length:

$$V_{1D} = \min(d, c\tau_{las}). \tag{3.21}$$

2D simulations: In two and three dimensions the opening angle Θ of the electron bunch which is created at the target front side influences the volume the hot electrons are distributed in. Assuming the electron bunch to be shorter than the target thickness the volume in two dimensions is

$$V_{2D} = c\tau_{las} 2 \left(d_0/2 + d \tan \Theta\right). \tag{3.22}$$

3D experiments: In three dimensions one obtains

$$V_{3D} = c\tau_{las}\pi \left(d_0/2 + d\tan\Theta\right)^2 . \tag{3.23}$$

The opening angle was measured to be approximately $\Theta = 25°$ [53].

In conclusion the volume is a function of the target thickness d and the laser pulse length τ_{las}. In two and three dimensions it depends on the laser spot diameter d_0 as well as on the opening angle Θ.

To calculate the number of hot electrons the absorbed fraction of laser energy fE_{las} is divided by the electron temperature, k_BT_e,

$$N_e = \frac{fE_{las}}{k_BT_e}. \tag{3.24}$$

In simulations the absorption f can be easily measured while for experiments an estimation is given by Key *et al.* [54] (I_{W/cm^2} is specified in W/cm^2) :

$$f(I) = 1.2 \times 10^{-15} I_{W/cm^2}^{0.75}. \tag{3.25}$$

With relations (3.20) and (3.24) the number of hot electrons can be computed as a function of the laser energy, i.e. it depends on the intensity, the laser wave length and for simulations on the absorbed fraction of laser energy:

$$N_e = N_e\left(f, I, \lambda, \tau_{las}\right). \tag{3.26}$$

Hence the hot electron density $n_{e0} = N_e/V$ can be obtained from experimental parameters:

$$n_{e0} = n_{e0}(I, E_{las}, \tau_{las}, \lambda, d_0, d, \Theta). \tag{3.27}$$

Expansion time

Mora's model is based on an isothermal plasma expansion. A finite acceleration time is chosen as in laser-plasma experiments the electrons transfer energy to ions and the expansion is adiabatic. Fuchs *et al.* [52] selected the acceleration time as a free parameter. Fitting the model to a wide range of experimental laser and target parameters yielded an acceleration time of $t = 1.33 \times \tau_{las}$. In section 5.1.4 the dependency of the maximum energy on the acceleration time is studied in detail.

3.3.2 Scaling of the maximum energy

In the previous sections the parameters which determine the maximum energy of an isothermal plasma expansion (equation 3.18) are linked to parameters which can be chosen in experiments. In chapter 5 this model is compared to one- and two-dimensional simulations as well as to experimental data from literature. To demonstrate the relation between the maximum energy and the experimental parameters already here some examples based on the model are discussed. The laser wavelength is $\lambda = 1$ μm and the intensity, the pulse duration and the target thickness are varied.

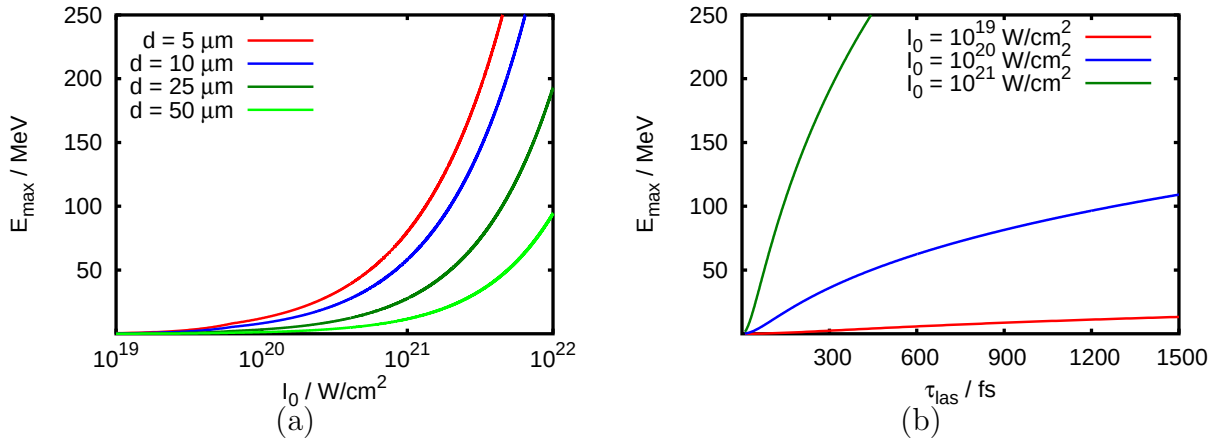

Figure 3.8: (a) The maximum energy depending on the intensity for a laser of 50 fs. The target thickness is varied between $d = 5$ μm and $d = 50$ μm (5 μm $\widehat{=}$ red, 10 μm $\widehat{=}$ blue, 25 μm $\widehat{=}$ dark green, 50 μm $\widehat{=}$ light green). (b) The maximum energy versus the pulse duration for a 25 μm thick target ($I = 10^{19} W/cm^2$ (red), $I = 10^{20} W/cm^2$ (blue), $I = 10^{21} W/cm^2$ (green)).

Dependency on intensity. To show the dependence on intensity a typical experimental set-up with an ultra-short pulse of 50 fs and a focal spot with diameter $d_0 = 10$ μm is chosen. Four exemplary target thicknesses between $d = 5$ μm and $d = 50$ μm are selected. Of course the maximum energy increases with increasing intensity. An energy of almost 200 MeV is predicted for a 25 μm foil at an intensity of $10^{22} W/cm^2$ (figure 3.8 (a)). These intensities will be reached by the class of Petawatt lasers which will be in use in the near future (e.g. [55]). However the choice of targets which should be as thin as possible might be inadequate due to their potential destruction, e.g. by the pre-pulse.

Dependency on pulse duration. In figure 3.8 (b) for a target thickness of $d = 25$ μm the maximum energy is plotted versus the pulse duration for various intensities. As the intensity is constant, a gain in pulse duration means an increase in laser energy. This results in an larger hot electron density and hence in an increase of the maximum proton energy.

Dependency on target thickness. Due to the divergence of the hot electron bunch the hot electron density is decreasing with increasing target thickness. From this a reduction of the maximum energy is following (figure 3.9).

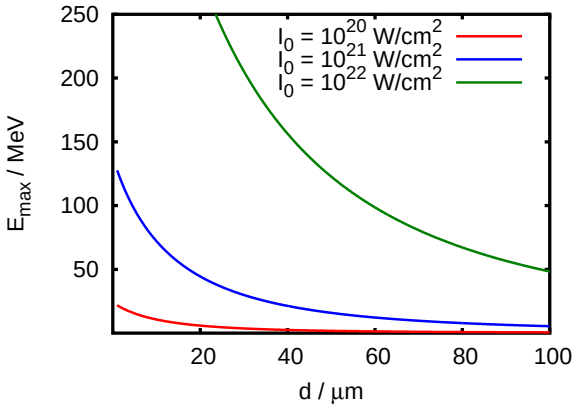

Figure 3.9: Maximum energy versus target thickness. The pulse duration is 50 fs, the red line represents $I = 10^{20} W/cm^2$, the blue one $I = 10^{21} W/cm^2$ and the green one $I = 10^{22} W/cm^2$.

3.4 Double-layer targets

In the interaction of a high-intensity laser with a solid target the dominating TNSA-mechanism (section 3.1.2) accelerates parasitic protons at the target rear side. However the corresponding electric field which the protons experience is inhomogeneous resulting in an exponential energy spectrum. On the one hand the inhomogeneity is based on the laterally varying density of the electron sheath producing a field gradient. On the other hand the field acting on protons which are not situated directly at the surface is shielded by protons placed at the target edge. To overcome the problem of an exponential energy spectrum which is inadequate for a lot of applications, Esirkepov *et al.* [10] proposed so-called double-layer targets.

3.4.1 Basics

These targets are composed of a substrate foil consisting of high-Z material (charge number Z_I and mass m_I) and a thin proton-rich dot on the rear side (charge number Z_i and mass m_i) with limited transverse dimension. The lateral limitation confines the dot to the homogeneous region of the electron sheath (figure 3.10). The thickness of the layer will influence the energy spread. The energy spectrum is expected to be narrower as the thickness of the coating is decreasing. In addition as the acceleration $a = ZeE/m$ is proportional to Z/m, the ratio $m_I Z_i / m_i Z_I$ should be sufficiently large. This ensures that the light ion layer is accelerated more efficiently and can separate from the heavy ion substrate.

Esirkepov *et al.* performed three-dimensional PIC simulations for a laser with an intensity of $1.2 \times 10^{20} W/cm^2$. The proton spectrum yields a quasi-monoenergetic peak

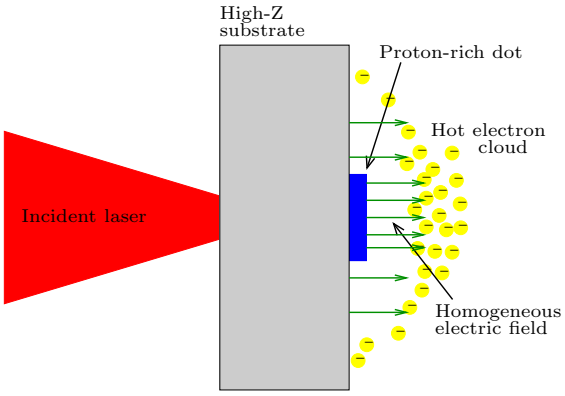

Figure 3.10: Hot electrons created at the front side penetrate through the target and form a sheath at the rear side. Due to the lateral confinement of the proton-rich dot all protons are located in the homogeneous region of the electric field. The generated proton spectrum yields a quasi-monoenergetic peak.

at 65 MeV. The relative energy spread is $\Delta E/E < 5\%$.

Schwoerer *et al.* [11] and Hegelich *et al.* [12] succeeded in realizing the double-layer target proposition experimentally. E.g. Schwoerer *et al.* used microstructured targets consisting of a 5 μm thick titanium foil coated with a 0.5 μm layer of hydrogen-rich polymethyl methacrylate (PMMA). This layer was microstructured by an ablation laser producing PMMA dots of 20×20 μm^2. The laser ($I \sim 3 \times 10^{19} W/cm^2$, $\tau_{las} = 80$ fs) was incident exactly on the opposite side of the dot. The resulting energy spectrum shows a peak at 1.2 MeV with a width of 0.3 MeV. By means of two-dimensional PIC simulations Schwoerer *et al.* showed that for $I = 1.2 \times 10^{21} W/cm^2$ microstructured targets can produce an energy spectrum with a peak at 173 MeV and a relative energy spread of 1%.

3.4.2 Albright's model

To describe the dependency of mean energy and quality of the quasi-monoenergetic light-ion layer on the target constituents Albright *et al.* [56] developed a one-dimensional analytical model.

Basic model

Initially (figure 3.11 shows the situation of an already propagated layer) a light-ion layer with negligible thickness and areal charge density Q_i is attached to a substrate of heavy ions at rest (density n_I, charge number Z_I and temperature $T_I \approx 0$). The electrons consist of two populations. A hot component ($n_{e,h}$, $T_{e,h}$) and a cold component with $n_{e,c} \simeq n_I Z_I$ and $T_{e,c}$, which both obey a Maxwellian energy distribution. Deep inside the

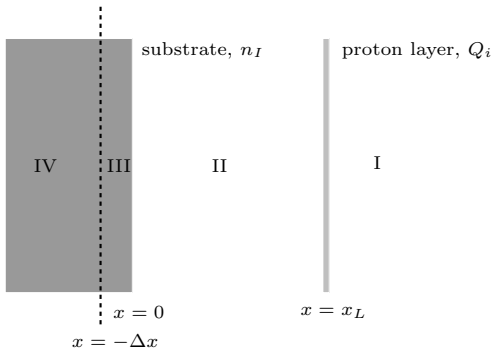

Figure 3.11: A proton layer with negligible thickness which is initially attached to a heavy ion substrate has propagated to position x_L. In region IV the electric field vanishes and boundary conditions ($T_{e,h}$, $T_{e,c}$, $\bar{n}_{e,h}$ and $\bar{n}_{e,c}$) are defined. To the right of the dashed line the cold electron population can be neglected. The proton layer is accelerated by the electric field due to the hot electron population.

substrate the electric field vanishes and the electron densities attain asymptotic densities $\bar{n}_{e,c}$ and $\bar{n}_{e,h}$. The propagating layer is described by the Poisson equation

$$\epsilon_0 \frac{\partial^2 \phi}{\partial x^2} = \bar{n}_{e,h} e \exp\left(\frac{e\phi}{k_B T_{e,h}}\right) + \bar{n}_{e,c} e \exp\left(\frac{e\phi}{k_B T_{e,c}}\right) - Q_i \delta(x - x_L) - Z_I e n_{I0} \nu(x) \quad (3.28)$$

with position of the layer, x_L, and the edge of the substrate at $x = 0$. $\nu(x) \equiv n_I(x)/n_{I0}$ denotes the relative ion density of the substrate (initially $\nu(x) = H(-x)$, H is the Heaviside function). For convenience the equation is rewritten in dimensionless variables $\xi = x/\lambda_D = x/\sqrt{\epsilon_0 k_B T_{e,h}/\bar{n}_{e,h} e^2}$, $\varphi = e\phi/k_B T_{e,h}$, $q = Q_i/\bar{n}_{e,h} e \lambda_D$ and $\Theta = Z_I n_I/\bar{n}_{e,h}$. In regions I-III (figure 3.11) the cold electron population may be neglected for sufficiently large hot electron temperatures $T_{e,h} \ll T_{e,c}$. Then the Poisson equation becomes

$$\varphi'' = \exp(\varphi) - q\delta(\xi - \xi_L) - \Theta\nu(\xi) \quad (3.29)$$

with the light-ion layer position $\xi_L = x_L/\lambda_D$. This equation is solved in each region (I-III) separately.

Solving Poisson's equation

In region I the terms belonging to the light-ion layer and the substrate vanish, $\varphi'' = \exp(\varphi)$. Using $\varphi = -\infty$ and $\varphi' = 0$ as $\xi \to \infty$ the potential and the electric field yield (appendix B.1)

$$\varphi = -2\ln[\exp(-\varphi_{L,I}/2) + (\xi - \xi_L)/\sqrt{2}] \quad (3.30)$$

$$\varphi' = -\frac{\sqrt{2}}{\exp(-\varphi_{L,I}/2) + (\xi - \xi_L)/\sqrt{2}} \quad (3.31)$$

with the potential $\varphi_{L,I} \equiv \lim_{\xi \downarrow \xi_L} \varphi(\xi)$ at the right hand side of the ion layer.

In region II the same integration as before with boundary conditions $\varphi_{L,II} = \varphi_{L,I} \equiv \varphi_L$, i.e. continuous potential, and $\varphi'_{L,II} = \varphi'_{L,I} + q$, i.e. discontinuous electric field due to the singularity in the light-ion charge, yields (appendix B.2)

$$\varphi = \varphi_L + \ln(1+\gamma^2) - 2\ln[1 + p\gamma\sqrt{\exp(\varphi_L)/a - 1}], \tag{3.32}$$

$$\varphi' = \sqrt{2}p\sqrt{\exp(\varphi) - a}. \tag{3.33}$$

with $a \equiv q\left[\sqrt{2}\exp(\varphi_L/2) - q/2\right]$, $\gamma \equiv \tan[(\xi_L - \xi)\sqrt{a/2}]$ and $p = \pm 1$.

In region III (thickness $\Delta\xi$) the ions shield the electric field of the sheath. As $\Theta \gg 1$, hot and cold electrons can be neglected and initially holds $\varphi'' = -\Theta$. Therefore the electric field and potential result in

$$\varphi = -\frac{1}{2}\Theta(\xi + \Delta\xi)^2 \tag{3.34}$$

$$\varphi' = -\Theta(\xi + \Delta\xi) \tag{3.35}$$

with the matching condition

$$\varphi'(0) = -\sqrt{-2\Theta\varphi(0)}. \tag{3.36}$$

First of all the propagation of the layer requires $a > 0$ as a is proportional to the mean force acting on the light ion layer ($F \propto (\partial_x\varphi_{L,I} + \partial_x\varphi_{L,II}) \propto (\partial_x\varphi_{L,I} + q/2) \propto (-\sqrt{2}\exp(\varphi_L/2) + q/2)$). In region I, i.e. on the right hand side of the propagating layer, the electric field is always positive (figure 3.12, equation (3.31)) and decreasing inversely with the distance to the layer. On the left hand side the characteristic of the electric field is determined by the factor $p = \pm 1$ in equation (3.33). For early times when the layer is accelerated $p = -1$ gives the right description. But if the layer propagates far enough and φ_L falls below $2\ln\left(q/\sqrt{2}\right)$ the potential yields a minimum as $\partial_x\varphi_L$ vanishes for $\varphi_L = 2\ln\left(q/\sqrt{2}\right)$ (equation (3.33)). Inserting the minimum, $\varphi_{min} = \ln(a)$ (following from equation (3.33)), in equation (3.32) gives the minimum position, $\xi_{min} = \xi_L - \sqrt{2/a}\arctan\left(\exp(\varphi_L)/a - 1\right)$. From 0 to ξ_{min} the potential and electric field are described by the $p = -1$ solution while for ξ_{min} to ξ_L the $p = +1$ solution is valid (figure 3.12). This means that a negative electric field is decelerating the ions at the rear side of the ion layer.

A descriptive explanation of this feature is the following: If the proton layer propagates far enough the hot electron density (which is decreasing with the distance to the substrate) on the right hand side of the layer cannot balance the proton layer charge anymore. Hence the resulting force which is acting on the left edge of the proton layer is pointing in the direction of the substrate.

To compute the potential and the electric field for a given set of parameters, q and Θ, φ_L at a given position ξ_L is determined. (If the layer has propagated far enough, i.e. $\varphi_L < 2\ln(q/\sqrt{2})$, φ_{min} at a given ξ_{min} is determined. From that a, φ_L and ξ_L are calculated). For this purpose the matching condition (3.36) is solved for $\varphi_{L/min}$. Then the electric field (figure 3.12) and the potential can be easily computed.

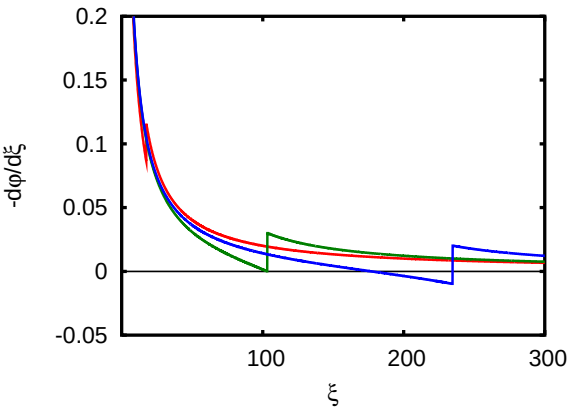

Figure 3.12: At early times, i.e. small ξ_L (red curve), the electric field is always positive and accelerates the light-ion layer. The discontinuity at the position of the layer is proportional to the charge. After the electric field has vanished at ξ_L (green curve) the field at the rear side is negative ($p = +1$ solution) and decelerates ions at the back surface (blue curve).

Energy spread

As in simulations and experiments the layer expands, the energy spread of the bunch is estimated ([56] and appendix B.3). The expansion is driven by the repulsive forces between the ions because the initial charge density of the ion layer is much larger than the local charge density of the hot electrons. In the center of mass frame a uniform slab expands until the density equals the local electron density, $Z_i n_i \approx \bar{n}_{e,h} \exp(\varphi_L)$, and results in an relative energy spread of

$$\left(\frac{\Delta E}{E_0}\right)_{1D} = \sqrt{\frac{q^2 \exp(-\varphi_L) k_B T_{e,h}}{E_0}}. \tag{3.37}$$

In three dimensions the expansion is additionally limited by the three dimensional divergence of the electric field. A layer with transverse dimension $L \gg d_i$, d_i is the initial thickness, expands like an one-dimensional layer until $d \sim L$. Then it expands more slowly as a sphere. The relative energy spread yields

$$\left(\frac{\Delta E}{E_0}\right)_{3D} = \min\left\{\left(\frac{\Delta E}{E_0}\right)_{1D}, \sqrt{\frac{q k_B T_{e,h} L}{3 \lambda_D E_0}}\right\}. \tag{3.38}$$

4 Plasma expansion

To study the characteristics of the main acceleration mechanism, the plasma expansion (see section 3.2), a one-dimensional electrostatic PIC code has been developed. As the principles of PIC codes are described in detail in section 2.3 here only the basic structure of the code is presented.

The simulation box consists of a grid with `NC` cells of width `cell_size`. `nr_species` number of particle species are initialized with properties stored in a list, the so-called `particle_sort_list`. These characteristics are `particle_names, mass, charge`, initial number of particles per cell, `NPC`, and `dynamics`, which indicates the kind of particle pusher (classical, relativistic or immobile particles). In addition the center of the plasma slab, `center_position`, the `length`, its `density` and `temperature` have to be specified. After initialization in the simulation loop the particles are assigned first-order weighting to the grid points. The Maxwell equations are solved for periodic boundary conditions by a simple algorithm which just adds up the charge on the grid points to determine `E(i=0)` with grid index `i` (see appendix C.1). Then `E(i+1)` is given by `E(i+1) = E(i) + 0.5 * cell_size * (rho(i+1) + rho(i))`. Afterwards the electric field is weighted to the positions of the particles which are accelerated by the resulting force.

For all particle species after `display_timesteps` iterations the particle densities (in file `density_***.dat`), the energy spectrum (`en_dist_***.dat`) as well as the electric field (`grid_***.dat`) and the xp_x-phase space (`ph_sp_m_***.dat`) are stored. `***` is the corresponding time and `m` the mass of the particle species. Additionally the electric, kinetic and total energy is stored (`energy.dat`).

The code is used to investigate the main characteristics of plasma expansions. At first the properties of a plasma slab with fixed ions is studied and compared to the analytical model. Afterwards simulations are performed for various parameter sets and the results are compared to the predictions of the theoretical approach. The electron density and temperature as well as the foil thickness are varied.

4.1 Initial state

At first the stationary situation of a plasma slab of fixed ions and a hot electron population is studied. This corresponds to the starting point of Mora's plasma expansion model (section 3.2). However in the simulation the foil has a limited thickness d instead of a homogeneously filled negative half space in the model.

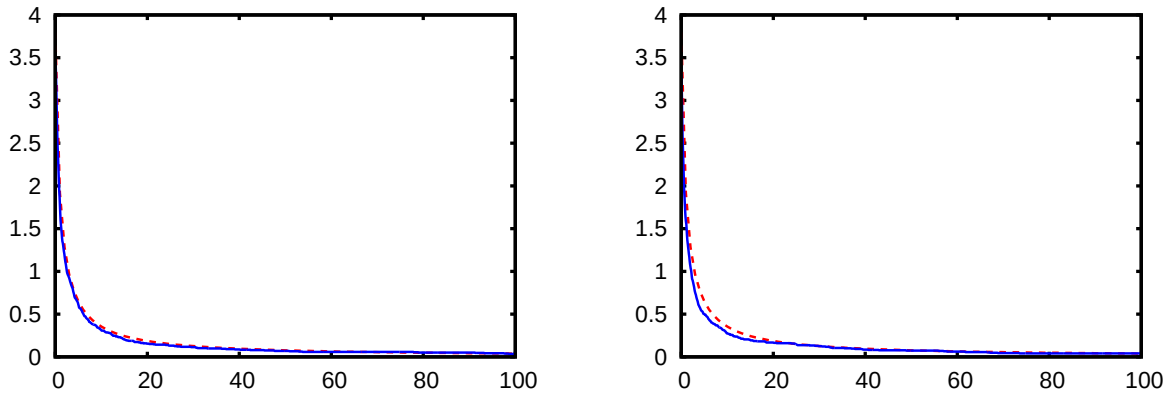

(a) $d = 30\ c/\omega_0$ (b) $d = 5\ c/\omega_0$

Figure 4.1: The comparison of the electric field for (a) a thick and (b) a thin plasma slab with fixed ions. The electron temperature is $T = 1$ MeV and the density $n = 10\ n_c$. The solid blue line shows the simulation result and the dashed red one represents the analytical model.

The analytical model provides an expression for the electric field (equation (3.4)),

$$E_x(x \geq 0, t = 0) = \sqrt{\frac{2}{\exp(1)}} E_{x,0} \frac{1}{1 + x/\sqrt{2\exp(1)}\lambda_D}, \tag{4.1}$$

with $E_{x,0} = \sqrt{n_{e0} k_B T_e / \epsilon_0}$ and Debye length $\lambda_D = \sqrt{\epsilon_0 k_B T_e / n_{e0} e^2}$ for a hot electron population with temperature T_e and density n_{e0} for $x \to -\infty$.

Two different set-ups are studied. At the beginning the electron population with temperature $T_e = 1$ MeV and density $n = 10\ n_c$ is confined to a plasma slab with thickness $d = 30\ c/\omega_0$ and $d = 5\ c/\omega_0$ respectively. The simulation is performed for several hundreds of $1/\omega_0$ and quickly reaching the stationary state with an exponential decreasing electron density outside the original foil. Though the plasma slab in the simulations yields a limited thickness the electric field matches the model predictions (figure 4.1).

4.2 The expansion

In the next step the expansion of a plasma slab is studied. Mora's model assumes an isothermal expansion with an infinitely large reservoir of hot electrons. The maximum energy and the electric field at the ion front after expanding for time t are (equation

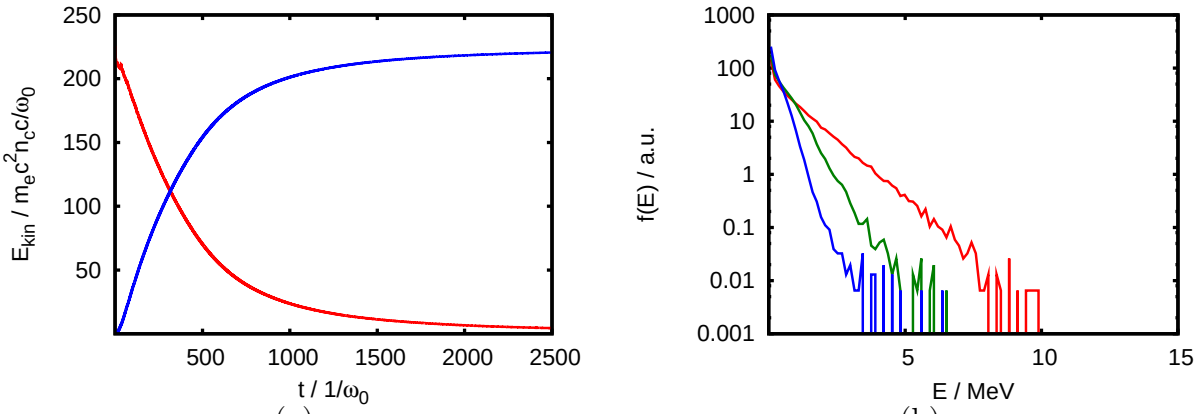

Figure 4.2: (a) The kinetic energy of electrons (red) and protons (blue) for an expanding plasma slab with initial thickness $d = 30\ c/\omega_0$, density $n = 5\ n_c$ and electron temperature $T = 1$ MeV. (b) The electron temperature is decreasing during the expansion ($t = 0\ 1/\omega_0$ (red), $t = 250\ 1/\omega_0$ (green), $t = 500\ 1/\omega_0$ (blue)).

(3.17) and (3.14))

$$E_{max} = 2Zk_BT_e\left[\ln\left(\tau + \sqrt{\tau^2+1}\right)\right]^2, \tag{4.2}$$

$$E_{x,front} \simeq \frac{2E_{x,0}}{\sqrt{2\exp(1)(1+\tau^2)}} \tag{4.3}$$

with $E_{x,0} = \sqrt{n_{e0}k_BT_e/\epsilon_0}$, $\tau = \omega_{pi}t/\sqrt{2\exp(1)}$ and $\omega_{pi} = \sqrt{n_{e0}Ze^2/m_i\epsilon_0}$. Hence the maximum energy is diverging logarithmically for $t \to \infty$. However the expansion of a plasma foil is non-isothermal. The electrons transfer their energy to the ions and therefore lose energy (figure 4.2). Thus the electron temperature is decreasing with time.

To investigate the influence of the limited number of hot electrons the model is compared to various PIC simulations. In addition the simulation results are compared to a numerically obtained expression for the maximum energy of the expansion of thin foils, proposed recently by Mora [51]

$$E_{max}^{foil} = 2m_i(c_s\ln(\alpha d/\lambda_D + \beta))^2 \tag{4.4}$$

with $c_s = \sqrt{Zk_BT_e/m_i}$ and fitting constants α and β. which slightly vary with electron temperature (e.g. for $T_e = 1$ MeV: $\alpha = 0.49$, $\beta = 5.3$). The effects of electron density, electron temperature and foil thickness are studied in the next sections.

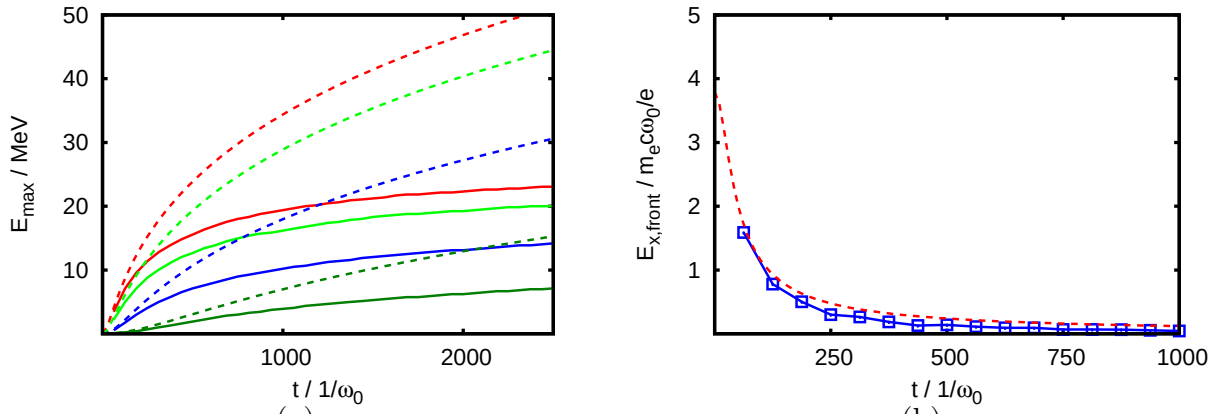

Figure 4.3: (a) Comparison of the evolution of the maximum energy in simulations (solid lines) with the analytical approach (dashed lines) ($d = 30\ c/\omega_0$, $T_e = 1$ MeV). The plasma density is $n = 0.1\ n_c$ (dark green), $n = 1.\ n_c$ (blue), $n = 5.\ n_c$ (light green), $n = 10.\ n_c$ (red) respectively. (b) The evolution of the electric field at the ion front for $n = 10\ n_c$. The dashed line represents the theoretical approach.

Varying the density

First of all the density is varied. The plasma slab has an initial thickness of $d = 30\ c/\omega_0$ and a temperature of $T_e = 1$ MeV is assigned to the electron population. The plasma density is $n = 0.1, 1, 5$ and $10\ n_c$ respectively. With increasing electron density the electric field at the ion front increases (see equation 4.3). Hence the maximum energy is also increasing with electron density. However the evolution of the maximum energy agrees with equation (4.2) only at the very beginning (figure 4.3 (a)). After a short time the increase of the maximum energy with time is weakened compared to the model. In addition in the simulations the maximum energy approaches a limiting value as the electrons are loosing more and more energy. The ratio of the maximum energy at a given time predicted by the model and the corresponding energy in the simulations is the same for all densities from 500 $1/\omega_0$ until the end of the simulations at 2500 $1/\omega_0$.

The evolution of the electric field (figure 4.3 (b)) also gives reasons for the lower energy in the expansion of the foil. The shape of the curve is almost identical but the electric field is always smaller in the case of the simulation compared to the model.

Varying the temperature

For a $30\ c/\omega_0$ thick plasma slab with a density of $n = 5\ n_c$ the initial electron temperature is varied, $T_e = 0.1$ MeV, $T_e = 0.5$ MeV and $T_e = 1$ MeV. Again the evolution of the

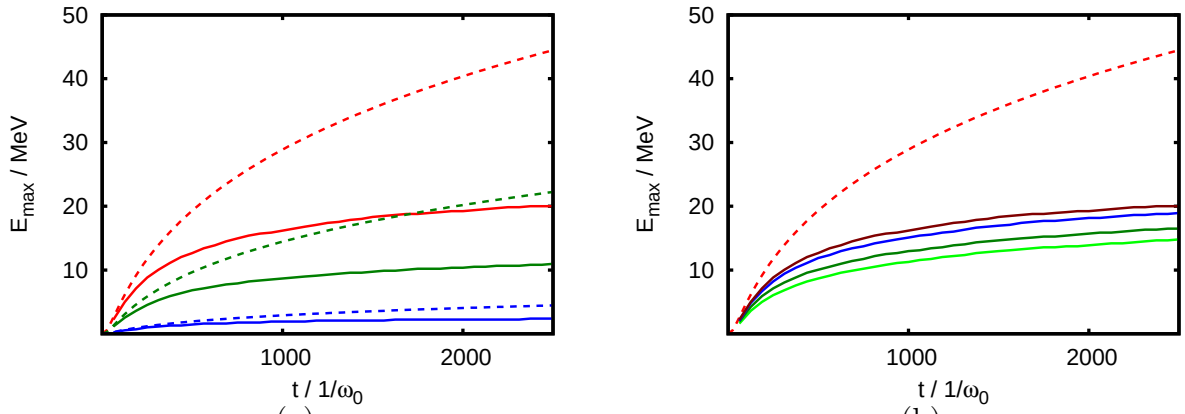

Figure 4.4: Comparison of the maximum energy predicted by the model (dashed lines) and the simulation results (solid lines). (a) For a plasma slab with $d = 30\ c/\omega_0$ and density $n = 5\ n_c$ the temperature is varied ($T = 0.1$ MeV (blue), $T = 0.5$ MeV (green), $T = 1$ MeV (red)). (b) For $T = 1$ MeV and density $n = 5\ n_c$ green), $d = 20\ c/\omega_0$ (blue) and $d = 30\ c/\omega_0$ (dark red).

maximum energy agrees with the model only in the beginning (figure 4.4 (a)). For increasing temperature the maximum energy increases. The deviation from the model is also changing with temperature. With increasing temperature the ratio of the isothermal and the non-isothermal maximum energy becomes larger.

Varying the foil thickness

For an electron temperature of $T_e = 1$ MeV and a plasma density of $n = 5\ n_c$ the foil thickness is varied, $d = 5, 10, 20$ and $30\ c/\omega_0$. The deviation from the isothermal model decreases with increasing thickness (figure 4.4 (b)). The thicker the target, the larger the reservoir of hot electrons and hence the better the simulation agrees with the theoretical approach.

Comparison to thin foil expansion

The comparison of the maximum energy with equation (4.4) shows a good agreement for most set-ups (table 4.1). The fitting parameters $\alpha = 0.49$ and $\beta = 5.3$ are chosen, which are specified in [51] for an electron temperature of $T_e = 1$ MeV.

As equation (4.4) is only valid for $d \geq \lambda_D$, deviations are found for thin targets. Additionally differences in the maximum energy of the simulations and the model predictions are observed for lower temperatures. This is due to the fact that the fitting parameters

T_e/ MeV	d/ c/ω_0	n/ n_c	E_{max}^{sim}/ MeV	E_{max}^{foil}/ MeV
1.	30.	5.	20.1	22.5
1.	20.	5.	18.2	18.5
1.	10.	5.	16.6	13.2
1.	5.	5.	14.5	9.8
1.	30.	0.1	7.1	9.3
1.	30.	1.	14.2	15.2
1.	30.	10.	22.9	26.6
0.5	30.	5.	10.8	13.3
0.1	30.	5.	2.3	3.8

Table 4.1: The maximum energy after 2500 $1/\omega_0$ for varying density, foil thickness and electron temperature. The simulation results are compared to equation (4.4). $\alpha = 0.49$ and $\beta = 5.3$ are chosen representing an electron temperature of $T_e = 1$ MeV.

in the above comparison are assumed to be independent of the temperature as the exact variation with temperature is unfortunately not explicitly specified in [51].

4.3 Summary

The basic features of the main acceleration mechanism for laser-accelerated protons, the plasma expansion, are studied with a self-developed one-dimensional electrostatic PIC code. The maximum energy is increasing with increasing temperature, density and foil thickness. This is due to the larger amount of energy in the plasma.

Mora [51] proposed an analytical expression for the maximum energy of expanding thin foils (equation (4.4)). The comparison with the simulation results (table 4.1) shows a good agreement. However deviations are found for lower temperatures and thin foils. The latter can be explained by the fact that the analytical approach is only valid for $d \geq 20\lambda_D$ which is violated for very thin targets. Additionally the constants α and β in equation (4.4) depend on the electron temperature but the dependence is not explicitely specified in [51].

The evolution of the maximum energy matches the isothermal model of plasma expansion [50] only at the very beginning. Afterwards due to the decreasing electron temperature in the simulations the increase in energy is more moderate compared to the model and approaching a limiting value.

In the next section the studies are extended to the situation where the interaction of the laser with the foil is included.

5 Scaling laws of laser-accelerated protons

The use of protons in radiotherapy requires energies of at least 70 MeV with a range of approximately 4 cm in water for the treatment of ocular tumors. However for deeper-seated tumors higher energies are necessary. A range of 32 cm in water which corresponds to a proton energy of 230 MeV would be suitable to treat most of the common tumors. However the maximum kinetic energy of laser-accelerated protons so far is less than 60 MeV [2]. To investigate the potential of laser-accelerated protons, in this chapter scaling laws of the maximum energy are studied.

The scaling of the maximum energy has been studied by PIC simulations [57] for intensities from $I = 10^{20} W/cm^2$ to $I = 10^{22} W/cm^2$ and target thicknesses between $d = 0.1$ μm and $d = 5$ μm. According to the resulting scaling, $200-300$ MeV protons can be obtained with a Petawatt laser with sub-picosecond duration. In addition analytical models [52, 50, 58] are proposed which also give the same order of magnitude for the intensity which would be necessary for suitable energies.

In this chapter one-dimensional PIC simulations in a wide range of currently available laser (intensity $I_0 = 5. \times 10^{18} - 1.1 \times 10^{20} W/cm^2$, i.e. $a_0 = 2. - 9.$, pulse duration $\tau_{las} = 53 - 531$ fs, i.e. $\tau_{las} = 100 - 500\ 1/\omega_0$) and target parameters (thickness $d = 0.8$ μm $- 15.9$ μm, i.e. $d = 5 - 100\ c/\omega_0$) are performed. The results are compared to the analytical model described in section 3.3 [52, 50]. In addition this model is compared to an exemplary series of two-dimensional simulations and to experimental data from literature. At the end the findings of the simulations and the model are used to roughly estimate the parameter regime for which clinically usable energies can be generated.

5.1 1D simulations

5.1.1 Basic set-up

All one-dimensional simulations with regard to the determination of the scaling of laser-accelerated protons are performed with the same basic set-up (figure 5.1). The laser is incident at the left hand side and hitting the plasma slab in the middle of the simulation box. The laser is characterized by the normalized vector potential a_0 and the pulse duration τ_{las}. The target with thickness d is composed of electrons and protons with densities of $n_{e/i} = 20\ n_c$. The size of one cell is $\Delta x = 0.1\ c/\omega_0$ and the time step is

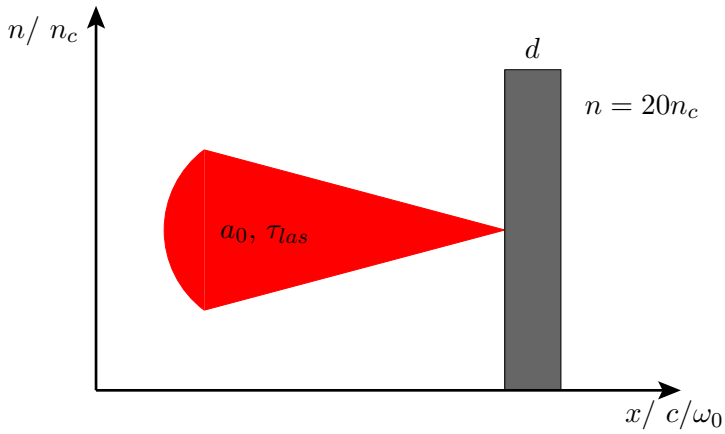

Figure 5.1: The basic set-up for one-dimensional simulations.

$\Delta t = 0.05\ 1/\omega_0$. Initially there are 600 particles per cell. At the left side particles obey reflecting boundary conditions while at the right hand side a combination of absorbing and reinjecting conditions is applied (Protons are absorbed while an electron is only absorbed if a proton is leaving the box in the same iteration step. Otherwise it is reinjected to ensure neutrality of the plasma). Absorbing boundary conditions are chosen for the electric fields.

Initial temperature

In the simulations only the interaction of the main pulse with the target is simulated. As the pre-pulse ionizes the target front one assumes that the main pulse is interacting with a plasma. However the influence of a pre-plasma will be neglected to keep the simulations simple. Thus one starts with a plasma slab of electrons and protons.

If an initial temperature is assigned to the electrons the plasma slab of course starts to expand. The expansion will affect the density gradient at the target front and back and hence the absorption of the laser pulse. To investigate the impact of the expansion prior to the interaction of the main pulse a series of simulations is performed for which the duration of the expansion is varied.

The parameters of the laser pulse are $a_0 = 8.5$ and $\tau_{las} = 136\ 1/\omega_0$. The target yields a thickness of $4.3\ c/\omega_0$. The duration of the plasma expansion before the arrival of the laser pulse is varied from $t_{pre-exp} = 50\ 1/\omega_0$ to $t_{pre-exp} = 1440\ 1/\omega_0$. Figure 5.2 shows the maximum energy and the absorption versus the expansion duration. The longer the expansion lasts the larger is the absorption. From $t_{pre-exp} = 50\ 1/\omega_0$ to about $t_{pre-exp} = 600\ 1/\omega_0$ it increases from around 10% to 23%. Afterwards it grows slightly. The increase is due to the changing density gradient at the front surface. The steeper the gradient is, the less laser energy is absorbed as the laser penetrates less deep inside the plasma (the laser is reflected at the critical density).

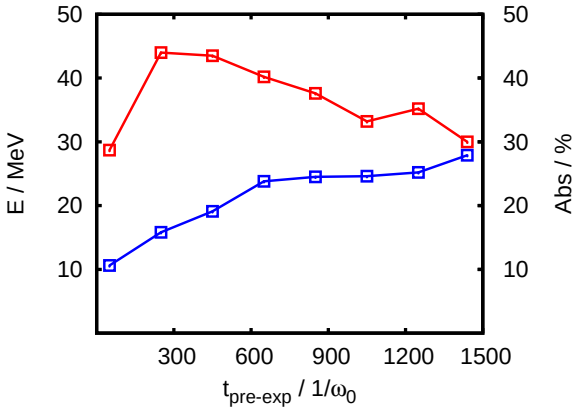

Figure 5.2: The absorption (blue) and the maximum energy (red) versus the duration of the expansion of the target before the laser pulse arrives.

The maximum proton energy however shows at first an increase, reaching a maximum at 200 $1/\omega_0$ and then is decreasing. This is based on two competing phenomena. On the one hand the absorption is increasing with increasing expansion duration leading to higher maximum energies. On the other hand the density gradient at the rear surface also changes. As the expansion takes longer the density profile at the back becomes smoother and hence the built up electric field decreases. This leads to a decrease of the maximum energy. In combination these two processes result in the above described behavior of the maximum energy.

To suppress the effect of the pre-expansion the target should always be in the same state when it is interacting with the laser. However the length of the simulation box is adapted to the laser and target parameters since higher proton energies lead to an larger extension of the protons. Hence the pre-expansion will change if an initial temperature is assigned to the electrons. Therefore the particles are assumed to be at rest at the beginning of the simulation.

How to measure the maximum energy?

Point in time: During the interaction of the laser with the plasma slab electro-magnetic energy is absorbed mainly by electrons. The hot electron population thereby created transfers energy to the protons on much longer timescales. Even for a very long expansion time (> 5000 $1/\omega_0$) the maximum energy still slightly increases. To compare the maximum proton energies for different simulation set-ups a proper point in time has to be chosen. As the temporal development is very similar for a wide spectrum of parameters (figure 5.3) a point in time is chosen when the increase of proton energy in time is negligible. For the simulations in the following sections the maximum energy is determined at 4000 $1/\omega_0$ after the maximum of the laser pulse has arrived at the front

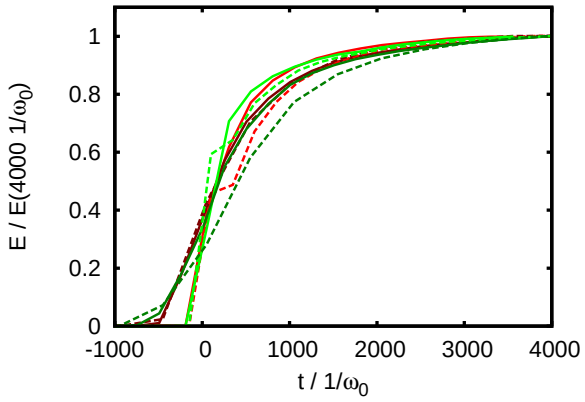

Figure 5.3: The temporal development of the maximum energy for various simulation set-ups. The point of origin of the time axis is the time when the maximum of the laser pulse arrives at the target surface. The energy is normalized to the maximum energy at 4000 $1/\omega_0$ after the arrival of the pulse. The temporal development is very similar for a huge spectrum of parameters ($a_0 = 2. \mathrel{\widehat{=}}$ red, $a_0 = 9. \mathrel{\widehat{=}}$ green, $\tau_{las} = 100 \mathrel{\widehat{=}}$ light color, $\tau_{las} = 500 \mathrel{\widehat{=}}$ dark color, $d = 15\ c/\omega_0 \mathrel{\widehat{=}}$ solid line, $d = 100\ c/\omega_0 \mathrel{\widehat{=}}$ dashed line).

side of the target.

Determination of the maximum: A typical characteristic of one-dimensional simulations is the existence of peaks in the energy spectrum (figure 5.4 (a)). These are due to single macro particles which experienced a larger acceleration than most of the other protons. By increasing the number of particles per cell, i.e. by representing less real particles by one macro particle, the number of peaks can be reduced. In addition the difference between the peak belonging to the most energetic proton (macro-particle) and the maximum "bulk" energy decreases with increasing particle number (figure 5.4 (b)). Actually the maximum energy remains almost constant while the "bulk" energy is increasing. Therefore the energy of the most energetic proton is chosen as the maximum energy. In the following simulations the initial number of particles per cell is 600 which is a compromise between saving computational time and reducing statistical noise.

5.1.2 Dependence on target thickness

At first the dependence on the target thickness is studied. The analytical model of the scaling of the maximum energy gives (section 5, equation (3.17)) gives

$$E_{max} = 2k_B T_{e,hot} \left[\ln \left(\tau + \sqrt{\tau^2 + 1} \right) \right]^2 \tag{5.1}$$

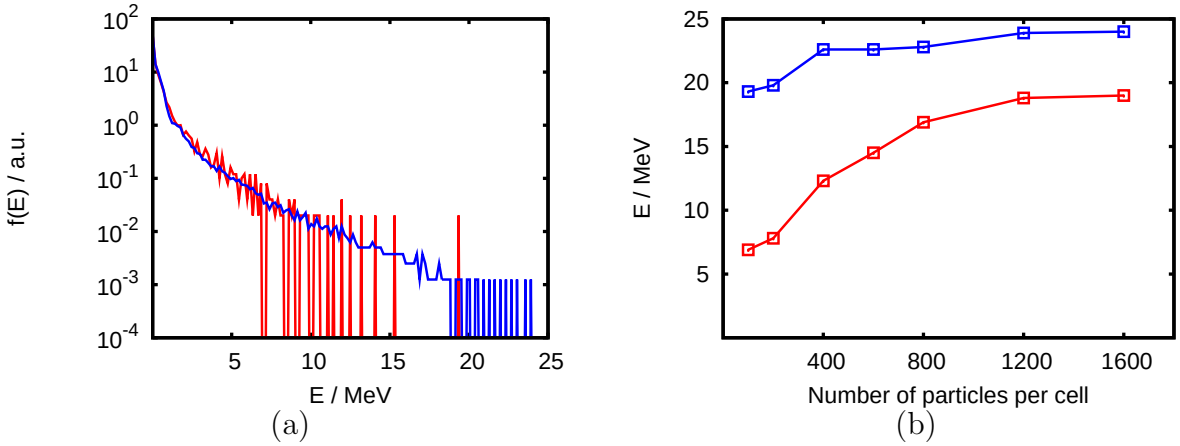

Figure 5.4: (a) The energy spectra for a laser pulse with $a_0 = 5.$, $\tau_{las} = 100\ 1/\omega_0$ interacting with a 5 c/ω_0 thick target. Red corresponds to 100 particles per cell and blue to 1600 particles per cell. (b) The maximum energy of the most energetic proton (blue) and the maximum "bulk" energy (red) versus the number of particles per cell for the aforementioned simulation set-up.

with the hot electron temperature $T_{e,hot}$ and

$$\tau = \frac{\omega_{pi} t}{\sqrt{2\exp(1)}} \propto \omega_{pi} \propto \sqrt{n_{e,hot}} \propto \sqrt{\frac{1}{d}}. \tag{5.2}$$

Hence the dependence on the thickness is included via the density of hot electrons which spread over the target.

For typical hot electron densities of $n_{e,hot} \sim\ n_c$, τ becomes larger than one and the maximum energy simplifies to $E_{max} = 2k_B T_{e,hot} \left[\ln(2\tau)\right]^2$ and hence

$$E_{max} = C_1 \left[\ln\left(\sqrt{\frac{1}{d_{c/\omega_0}}}\right) + C_2\right]^2. \tag{5.3}$$

The target thickness d_{c/ω_0} is specified in units of c/ω_0. C_1 is proportional to the hot electron temperature and C_2 is depending on the hot electron temperature, the fraction of absorption, the laser energy and the expansion time. For a given laser pulse C_1 and C_2 shall remain constant when varying the target thickness. Hence the maximum energy shall decrease with increasing target thickness.

In the simulations the thickness is varied between 5 c/ω_0 and 100 c/ω_0 for laser pulses with $a_0 = 2. - 9.$ and $\tau_{las} = 100 - 500\ 1/\omega_0$. In all simulations a decrease of the maximum energy with increasing target width is found (in fact all simulations are performed in the non-transparent regime where no optimum target thickness is expected [59]). Figure 5.5

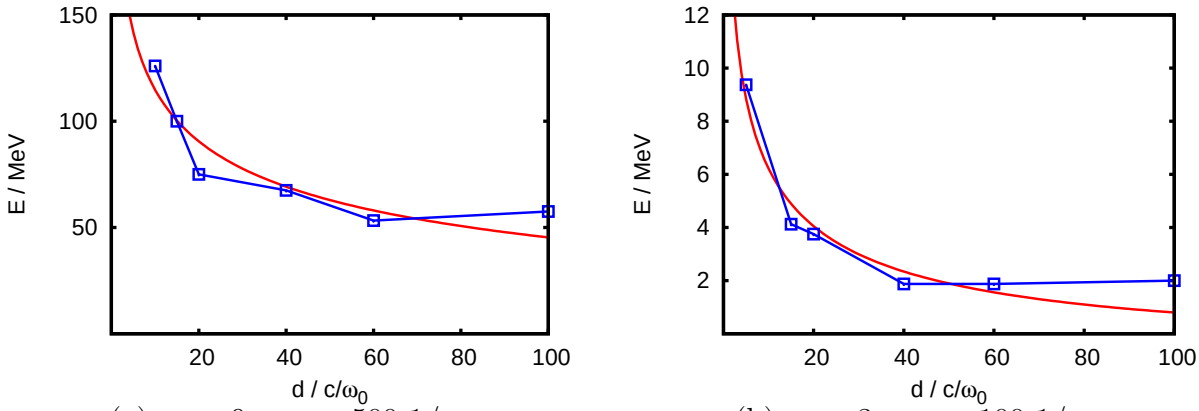

(a) $a_0 = 9$, $\tau_{las} = 500\ 1/\omega_0$ (b) $a_0 = 3$, $\tau_{las} = 100\ 1/\omega_0$

Figure 5.5: The maximum energy for a high intensity, long pulse (a) and a low-intensity, short pulse (b) simulation. Equation (5.3) is fitted to the data points. The red lines represent the fit and the blue ones the simulation results.

shows the simulation results for a high intensity, long pulse case ($a_0 = 9.$, $\tau_{las} = 500\ 1/\omega_0$ and a low intensity, short pulse case ($a_0 = 3.$, $\tau_{las} = 100\ 1/\omega_0$). Equation (5.3) is fitted to these two simulation cases yielding a good description of the dependence of the maximum energy on the target width. The fitting results in $C_1 = 12$ MeV, $C_2 = 4.2$ for the long pulse and $C_1 = 1.9$ MeV, $C_2 = 2.95$ for the short pulse respectively. For the latter, C_1 is close to the expected value resulting from the hot electron temperature (equation (3.20)), $C_1^{mod} = 2m_e c^2(\sqrt{1+a_0^2} - 1) = 2.2$ MeV. For the high intensity pulse however the prediction of the model, $C_1^{mod} = 9.2$ MeV, deviates more significantly from the fitting result.

In general for lower intensities $a_0 \leq 5$ the values predicted by the model agree quite well with the fitting results (figure 5.6 (a)). For higher intensities the deviations from the model become larger. But nevertheless the model provides a good estimation of the constant C_1.

The second constant, C_2 (figure (5.6) (b)), is in the range of 3 to 6. For shorter pulses it is slightly increasing with rising intensity. For longer pulses however no clear dependence on the intensity is visible.

5.1.3 Dependence on intensity

In a second step the dependency of the maximum energy on the laser intensity, characterized by the normalized potential a_0, is studied. The maximum energy (equation (5.1)) is depending on the hot electron temperature T_e and $\tau = \omega_{pi} t/\sqrt{2\exp(1)}$. In the previous section the scaling of the hot electron temperature is satisfactorily described

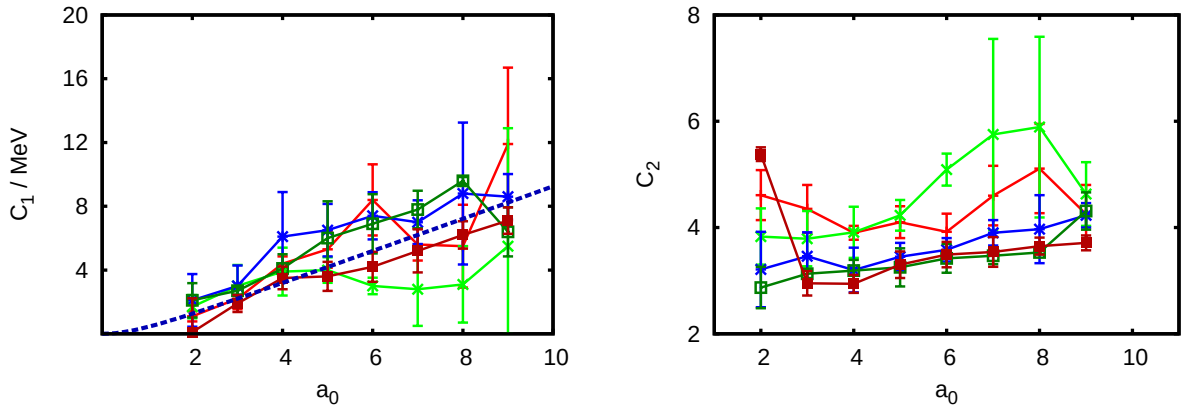

(a) (b)

Figure 5.6: The constants C_1 and C_2 obtained by fitting the simulation results to equation (5.3) for various pulse lengths (100 $1/\omega_0$ (dark red), 200 $1/\omega_0$ (dark green), 300 $1/\omega_0$ (blue), 400 $1/\omega_0$ (light green), 500 $1/\omega_0$ (red)). Additionally in (a) the constant expected from the model is plotted (dashed blue).

by the ponderomotive potential for a wide range of parameters (figure 5.6 (a)). Hence the maximum energy is

$$E_{max} = 1.022 \text{ MeV} \left(\sqrt{1+a_0^2} - 1\right) \left[\ln(\tau + \sqrt{\tau^2+1}\right]^2. \tag{5.4}$$

with $\tau \backsimeq 0.01 t \sqrt{n'_{e,hot}}$, $n'_{e,hot}$ is given in units of n_c and t is the acceleration time. The latter is assumed to be of the order of the laser pulse duration, $t = R \times \tau_{las}$ with the characteristic acceleration time coefficient R, and will be determined in the following.

Before that the calculation of the hot electron density is analyzed in more detail. The hot electron density is given by (section 3.3.1)

$$n_{e,hot} = \frac{f E_{las}}{k_B T_e d} \tag{5.5}$$

with absorption f, laser energy E_{las} and target thickness d. For $a_0 \geq 3$, inserting the laser energy and expanding for large a_0 this expression simplifies to

$$n_{e,hot} = 0.532 f \frac{\tau'_{las}}{d'} \frac{a_0^2}{\left(\sqrt{1+a_0^2} - 1\right)} n_c \tag{5.6}$$

$$\backsimeq 0.532 f \frac{(a_0+1)\tau'_{las}}{d'} n_c, \tag{5.7}$$

where τ'_{las} and d' are given in units $1/\omega_0$ and c/ω_0 respectively.

However the absorption f is varying with laser intensity and pulse duration. But an empirical characterization yields $f = \alpha(\tau_{las}, d) a_0^{\beta(\tau_{las},d)}$ (appendix D.1.1). Thus the maximum energy is given by

$$E_{max} = 1.022 \text{ MeV} \left(\sqrt{1 + a_0^2} - 1 \right) \times \tag{5.8}$$

$$\left[\ln \left(0.01 R \tau'_{las} \sqrt{0.532 \alpha a_0^{\beta} \frac{(a_0 + 1)}{d'} \tau'_{las}} \right. \tag{5.9}$$

$$\left. + \sqrt{\left(0.01 R \tau'_{las} \sqrt{0.532 \alpha a_0^{\beta} \frac{(a_0 + 1)}{d'} \tau'_{las}} \right)^2 + 1} \right) \Bigg]^2 . \tag{5.10}$$

As the model describes an isothermal expansion a characteristic expansion time, $t = R\tau_{las}$, is assumed to take into account the adiabatic expansion in laser-plasma experiments. Fuchs *et al.* suggest to use the acceleration time as a free parameter and fit it for their experimental results to $t = 1.33\tau_{las}$, i.e. $R = 1.33$. Following the suggestion of using the acceleration time as a free parameter the simulation results are fitted to equation (5.10).

The normalized vector potential is varied between $a_0 = 3.$ and $a_0 = 9.$ for target thicknesses $d = 10, 15, 20, 60\ c/\omega_0$ and pulse durations of $\tau_{las} = 100, 200, 300, 400, 500\ 1/\omega_0$. The equation properly characterizes the dependence of the maximum energy on the intensity (figure 5.7 (a)).

The characteristic acceleration time coefficient (figure 5.7 (b)) is of the order of one and decreasing with the pulse length. For $t = 100\ 1/\omega_0$ it is about $R \sim 2.$ while it is decreasing to $R \sim 0.55$ for $500\ 1/\omega_0$. Remarkably the target thickness is only slightly influencing the parameter R. An overall fit gives the relation ($\tau_{las,1/\omega_0}$ is given in units of $1/\omega_0$)

$$R = (111. \pm 21.) \times \tau_{las,1/\omega_0}^{-0.86 \pm 0.035}. \tag{5.11}$$

5.1.4 Dependence on pulse duration

The time-dependent characteristic acceleration time coefficient R is obtained by fitting the maximum intensity depending on the laser intensity. Here the resulting fit (equation (5.11)) is validated for varying pulse duration. Figure 5.8 shows the results for (a) a small thickness of $d = 15\ c/\omega_0$ and (b) a large thickness of $d = 60\ c/\omega_0$. The intensity is varied between $a_0 = 3.$ and $a_0 = 10.$ and the pulse duration between $\tau_{las} = 100\ 1/\omega_0$ and $\tau_{las} = 500\ 1/\omega_0$. The simulation results are compared to the analytical prediction (equation (5.1) where the characteristic acceleration time coefficient obeys equation (5.11). As the absorption is varying with the pulse length the analytical prediction is given for the maximum and the minimum absorption.

For the thin target a good agreement of the simulation results and the theoretical model is found (except for $a_0 = 10.$ where the model under-/overestimates the maximum

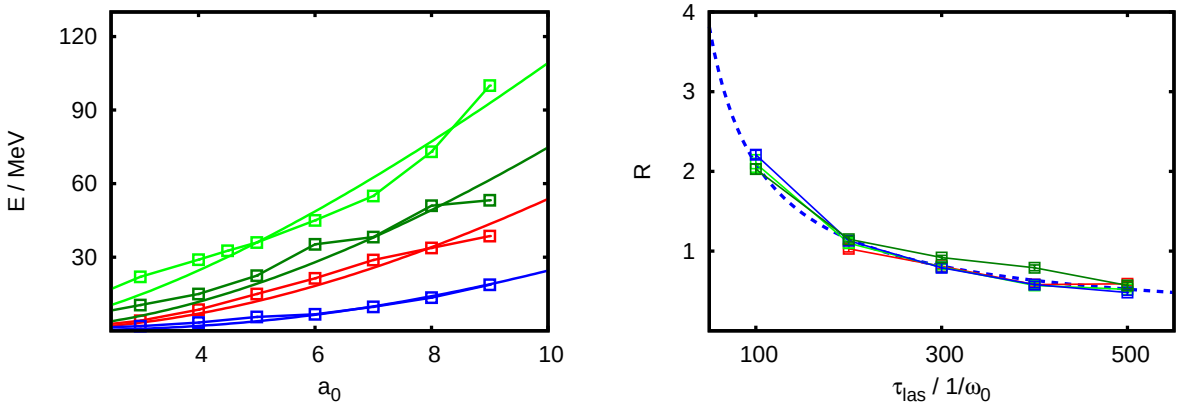

(a) (b)

Figure 5.7: (a) Fit of maximum energy versus a_0, equation (5.10), to the simulation results for three different sets of parameters. Red represents $\tau_{las} = 100\ 1/\omega_0$, $d = 15\ c/\omega_0$, light green $\tau_{las} = 500\ 1/\omega_0$, $d = 15\ c/\omega_0$, blue $\tau_{las} = 100\ 1/\omega_0$, $d = 60\ c/\omega_0$ and dark green $\tau_{las} = 500\ 1/\omega_0$, $d = 60\ c/\omega_0$. (b) The characteristic acceleration time coefficient versus pulse duration for $d = 10\ c/\omega_0$ (red), $d = 15\ c/\omega_0$ (light green), $d = 20\ c/\omega_0$ (blue) and $d = 60\ c/\omega_0$ (dark green).

energy for short respectively long pulse durations). In the case of the $d = 60\ c/\omega_0$ target the model is in agreement with the simulation results for short pulse durations. For longer pulses, $\tau_{las} \geq 400\ 1/\omega_0$ however the simulations yield an increased maximum energy compared to the model.

5.1.5 Dependence on pulse duration at constant laser energy

In this subsection the fit of the characteristic acceleration time coefficient R (equation 5.11) is compared to an additional series of simulations. For a constant laser energy, $E_{las} \propto a_0^2 \tau_{las}$, simulations with varying pulse length between $\tau_{las} = 100\ 1/\omega_0$ and $\tau_{las} = 1000\ 1/\omega_0$ are performed. The reference pulse (i.e. the laser pulse which defines the energy which in the following is kept constant) yields the normalized vector potential $a_0 = 10.$ at a pulse duration of $\tau_{las} = 100\ 1/\omega_0$. Four different target thicknesses, $d = 5, 15, 40, 100\ c/\omega_0$, are studied.

For the two thinnest targets the model and the simulations agree for pulse durations $\tau_{las} \lesssim 500\ 1/\omega_0$. For longer pulses however the maximum energy is further decreasing according to the model while the simulations show a constant or even increasing maximum energy. This deviation can be explained by a closer look at the expected hot electron density. E.g. for $\tau_{las} = 500\ 1/\omega_0$ and $d = 5$ respectively $15\ 1/\omega_0$ equation (5.7) yields a hot electron density of $n_{e,hot} > 40\ n_c$ and $15\ n_c$ at an absorption of $f = 15\%$. This

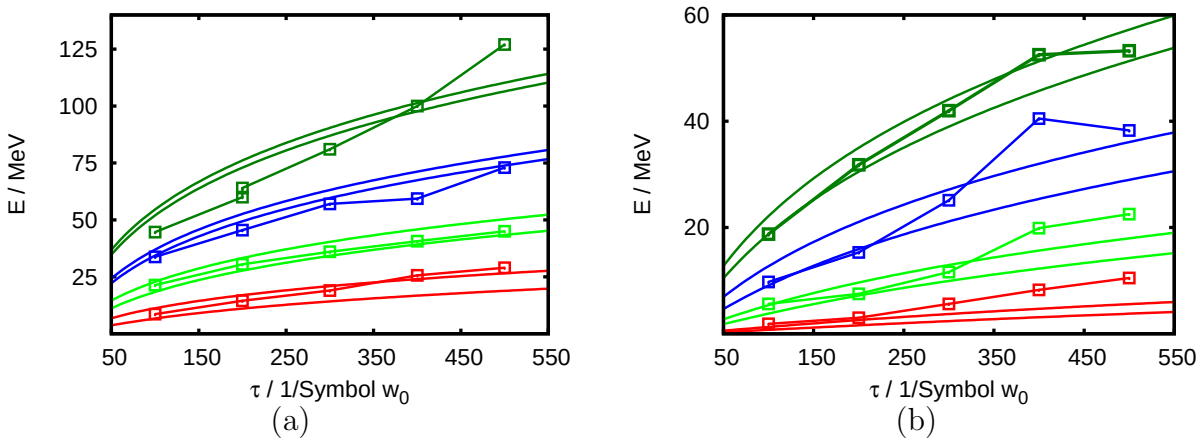

Figure 5.8: The maximum energy versus laser pulse duration for (a) a thin target, $d = 15\ c/\omega_0$, and (b) a thick target, $d = 60\ c/\omega_0$. The red curves represent (a) $a_0 = 10.$ / (b) $a_0 = 9.$, the light green ones $a_0 = 8./a_0 = 7.$, blue $a_0 = 6./a_0 = 5.$ and dark green $a_0 = 4./a_0 = 3.$

means that the analytical hot electron density can exceed the initial electron density of $n_e = 20\ n_c$. In this case the absorbed energy will lead to an further increase of the average electron energy as the total number of electrons is limited. Hence the hot electron temperature shall increase. As the maximum energy (equation (3.17) is depending linearly on the hot electron temperature but only logarithmically on the corresponding density an increase in the maximum energy is expected.

However for the thicker targets, $d = 40$ and $100\ c/\omega_0$, the simulations and the theoretical predictions show a quite different behavior of the maximum energy (figure 5.9 (b)). While the simulations show an increase in the maximum energy with increasing pulse duration the model predicts a decrease.

5.1.6 Discussion

One-dimensional PIC simulations are performed for a wide range of parameters. The normalized vector potential, $a_0 = 2. - 10.$, the pulse duration $\tau_{las} = 100 - 500\ 1/\omega_0$ and the target thickness $d = 5. - 100.\ c/\omega_0$ are varied. The simulation results are in good agreement with the analytical model proposed by Fuchs *et al.* [52] when extending the model by the introduction of a time-dependent characteristic acceleration time coefficient $R(\tau_{las})$. Especially for short pulses and thin targets the simulation results agree well with the model. Fitting of the simulation results to the analytical prediction yields a simple relation of R on the pulse duration, $R = (111. \pm 21.) \times \tau_{las}^{-0.86\pm0.035}$. This relation is independent of target thickness and intensity. Furthermore the finite acceleration time

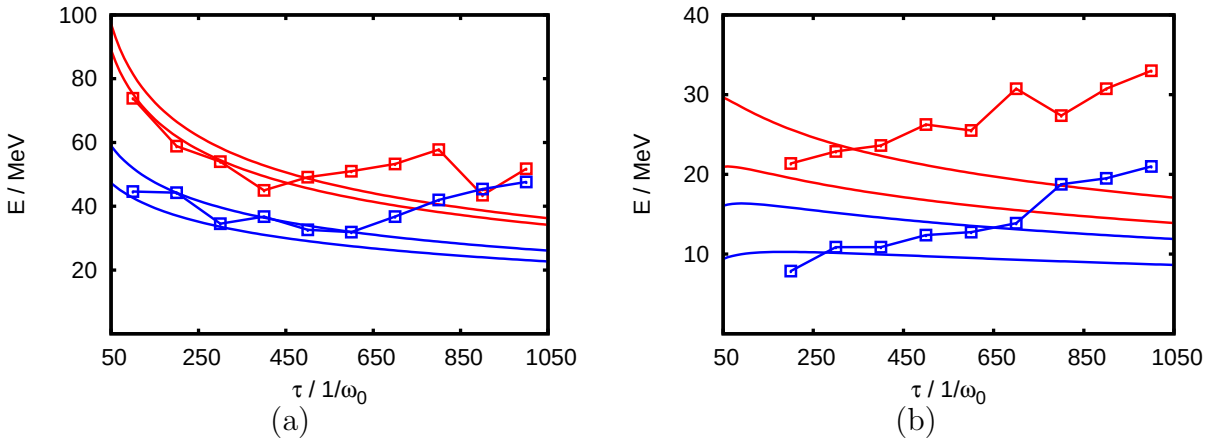

Figure 5.9: The maximum energy versus laser pulse duration at constant laser energy. (a) For thin targets, $d = 5\ c/\omega_0$ (red) and $d = 15\ c/\omega_0$ (blue), the model agrees with the simulations for short pulse durations. (b) For thicker targets, $d = 40\ c/\omega_0$ (red), $d = 100\ c/\omega_0$ (blue) the model and the simulations show conflicting results.

which takes into account the fact that the plasma is expanding non-isothermally, is of the order of the pulse duration. This can be substantiated by the idea of a constant temperature during the interaction of the laser pulse with the plasma. The fact that the characteristic acceleration time coefficient is decreasing with increasing pulse duration can be explained by the longer lasting expansion. As for a long pulse the plasma is expanding much further while the laser is interacting with the target compared to a short pulse, the hot electron density drops much stronger during the interaction. And as the hot electron density is assumed to be constant in the model this is taken into account by reducing the characteristic acceleration time coefficient.

To check if the model can also be applied in two and three dimensions in the following section two-dimensional PIC simulations are performed. Subsequently experimental data from literature is compared to the model.

5.2 2D simulations

As two-dimensional simulations are much more time-consuming only a a few set-ups are chosen to study the scaling of the maximum energy. In subsection 5.1.5 the predictions of the analytical model and the simulation results differ for a series of simulations with constant energy and varying pulse durations. Though these deviations occur especially at large thicknesses the two-dimensional simulations are performed for a thin target of $d = 7.7\ c/\omega_0$ to avoid excessive computational time.

5.2.1 Dependence on pulse duration at constant laser energy

The simulations are performed in a 750. $c/\omega_0 \times 144.$ c/ω_0 box consisting of grid cells with $\Delta x = \Delta y = 0.16$ c/ω_0. 40000 time steps with $\Delta t = 0.08$ $1/\omega_0$ are performed, resulting in a total simulation time of $T = 3200$ $1/\omega_0$. The target ($d = 7.7$ c/ω_0) is placed at $x = 200$ c/ω_0 and consists of 20 n_c electrons and protons. Initially neither the proton nor the electron population possess a temperature. In addition the electrons are placed at the same positions as the protons to avoid an expansion before the arrival of the laser pulse (see section 5.1.1 for more details). Both species are initialized with 30 particles per cell.

The reference laser pulse with a $\cos^2$-shape is operating at intensity $a_0 = 10.$ and pulse length[1] $\tau_{las} = 100$ $1/\omega_0$. In y-direction the pulse is Gaussian shaped with a full width at half maximum of $d_0 = 30$ c/ω_0. The pulse duration is increased to 1000 $1/\omega_0$ in steps of 100 $1/\omega_0$ while keeping the total laser energy constant.

The simulations yield the same behavior like the one-dimensional simulations for thin targets and short pulse durations (section 5.1.5). The maximum energy, which is measured 2500 $1/\omega_0$ after the arrival of the maximum at the target surface, is decreasing with increasing pulse duration (figure 5.10 (a)). However in contrast to the one-dimensional simulations the energy does not start to increase again. As in two dimensions the laser is limited in transversal direction, "additional" electrons are located outside the focal spot which can also be heated. Hence even for long pulses the number of electrons which can experience heating is not exceeded. The electron temperature dose not increase and the simulations show the same decrease as the model.

The simulation results are fitted to equation (3.17 (a)) postulating a time-depending characteristic acceleration time coefficient, $R = a\tau_{las}^b$. As the absorption is varying between 27% and 31% an average absorption of 29% is chosen. Due to the small thickness of the layer and the limited transversal dimension the electrons spread over the whole target. Though apparently the electron density varies in y-direction it is assumed that the hot electron population is distributed homogeneously. This results in the two-dimensional volume $V_{2D} = 144.$ $c/\omega_0 \times 7.7$ c/ω_0. The fit shows a good agreement with the simulation results (figure 5.10 (a)). The characteristic acceleration time coefficient is given by

$$R = (113. \pm 9.1) \times \tau_{las}^{-0.93 \pm 0.019}. \tag{5.12}$$

Like in the case of one-dimensional simulations, it is of the order of the laser pulse duration (figure 5.10). In addition the general shape and the order of magnitude agree with the one-dimensional characteristic acceleration time coefficient. Actually the exponent differs only by 7% from the exponent derived from one-dimensional simulations.

[1] Note that for $\cos^2$-shaped pulses the pulse duration denotes the *total* length of the pulse.

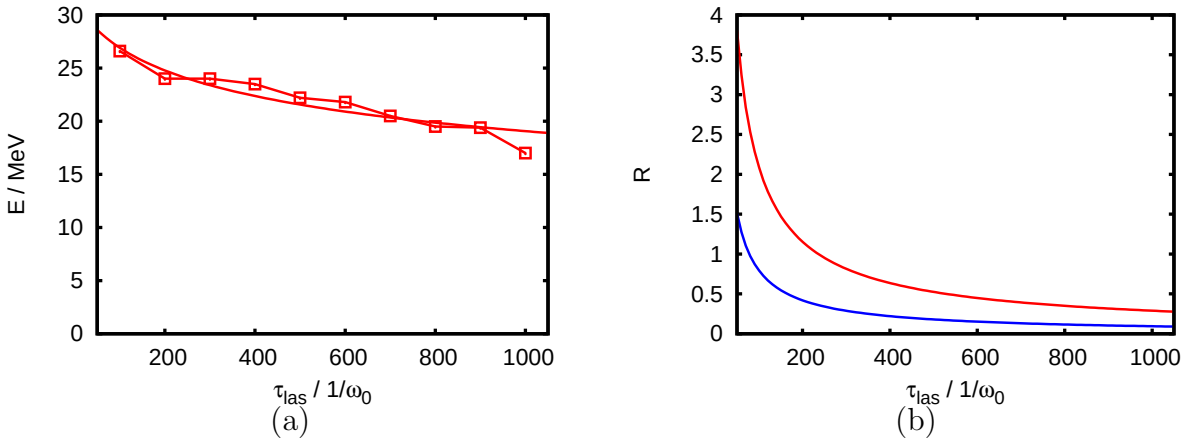

Figure 5.10: (a) Maximum energy versus pulse duration for constant laser energy (at $\tau_{las} = 100\ 1/\omega_0$ the normalized vector potential is $a_0 = 10.$). The data points are fitted to the analytical model, assuming a time-dependence of the characteristic acceleration time coefficient. (b) The characteristic acceleration time coefficient for one- (red) and two-dimensional (blue) simulations. For this plot the two-dimensional pulse duration (i.e. the total length of a $\cos^2$-shaped pulse) is mapped to the full width half maximum of a laser pulse with the same maximum intensity and identical laser energy.

5.2.2 Discussion

The predictions of the analytical model agree well with the results of the two-dimensional PIC simulations when a time-dependent characteristic acceleration time coefficient is assumed. As only a limited number of simulations are performed, conclusions can be drawn only to a certain extent. However the agreement of the exponent of the characteristic acceleration time coefficient with the one-dimensional result seem to justify the application of the model to predict maximum energies or various parameter sets. To study if the model still holds in three dimensions it is compared to experimental results from literature.

5.3 Comparison to experimental data from literature

The experiments are selected to represent a wide range of parameters. In addition only data with exactly specified laser and target parameters are chosen. The intensity varies from $I = 1 \times 10^{17} W/cm^2$ to $I = 6 \times 10^{20} W/cm^2$, the pulse duration from 40 fs to 500 fs and the target thicknesses from 0.75 μm to 220 μm.

The comparison is divided into two groups in order to distinguish between a high and

Reference	$I_0/10^{18} W/cm^2$	τ_{las}/ fs	d/ μm	λ/ μm	d_0/ μm
A. Maksimchuk *et al.* [45]	0.2 - 3.3	400	0.1 - 25	1.053	10.
A. Mackinnon *et al.* [60]	100.	100	3 - 100	0.8	3./5.
M. Allen *et al.* [48]	10.-50.	300	10./48.	1.058	9.4
M. Kaluza [37]	10.	150	0.75 - 85	0.790	5.
J. Fuchs *et al.* [52]	60.	320	20 - 220	1.057	6.

Table 5.1: Summary of experimental data from literature compared to the model with a high pre-pulse contrast.

a low contrast of pre- and main pulse. At first experiments with a high contrast are considered, $I_{pre}/I_0 < 10^{-6}$, with $I_{pre/0}$ denoting the intensity of the pre- and the main pulse respectively. In the second section low contrast experiments ($I_{pre}/I_0 \geq 10^{-6}$) are compared to the model. While in the aforementioned experiments the maximum measured energy is depending on another parameter (like e.g. target thickness or intensity) at the end experiments with only one or a few data points are compared to the model.

5.3.1 Experiments with a high contrast pre-pulse

Table 5.1 summarizes the experiments compared to the model in this subsection. Maksimchuk *et al.* [45] measured the maximum proton energy depending on intensity and target thickness respectively. For varying intensity the model is in good agreement with the experimental results (figure 5.11 (a)). The increase as well as the absolute maximum energy values are given by the analytical predictions. However in the case of the maximum energy dependence on the target thickness the experiments and the model give conflictive results (figure 5.11 (b)). While the model yields a decrease of the maximum energy with increasing target thickness the experimental data shows an increase up to a thickness of 10 μm and a decrease afterwards.

Mackinnon *et al.* [60], Kaluza *et al.* [37] and Fuchs *et al.* [52] measured the maximum proton energy for a wide range of target thicknesses ($0.75 - 220.$ μm). The model as well as the experiments show in general a decrease in the maximum energy with thicker getting targets (figure 5.12 (a) and appendix D.2.1 for additional figures). With the assumptions on the absorption and the opening angle of the electron beam of section 5 the absolute energy values of the model agree with the experimental data of Mackinnon *et al.* and Fuchs *e*t al.. However Kaluza *et al.* set the half-angle of the electrons beam to 8° and got an absorption of 25%. With these values the model is again in good agreement with the experimental results. In addition they observed an optimal target thickness where the proton energy reaches a maximum. This thickness is depending on the pre-pulse duration. The observations can be explained by the fact that the pre-pulse can affect the density gradient on the rear surface by a shock wave or radiative heating. Hence for thin targets the TNSA mechanism at the rear side becomes less important

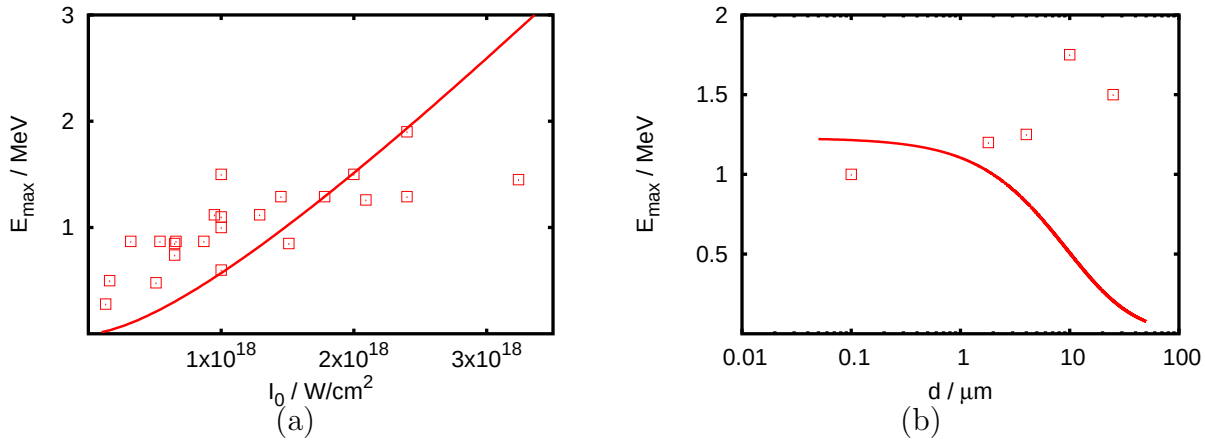

Figure 5.11: Data adapted from Maksimchuk *et al.* [45]. The increase in maximum proton energy with increasing intensity is correctly described by the model (a). For the dependence on the target thickness however the model yields deviating results compared to experimental data.

Reference	$I_0/10^{18}W/cm^2$	τ_{las}/ fs	d/ μm	λ/ μm	d_0/ μm
I. Spencer *et al.* [61]	7.	60.	0.2 - 90.	0.790	2.5/5.
K. Nemoto *et al.* [62]	0.5 - 6.	400	6.	1.053	12.
Y. Oishi *et al.* [63]	2.13 - 12.39	55 - 400	5. -7.	0.800	6.6

Table 5.2: References of experimental data with a low pre-pulse contrast which are compared to the analytical model. Oishi *et al.* specify a spot of 4×11 μm^2 at FWHM which yields the same surface as a spot with $d_0 = 6.6$ μm.

and the less efficient front side acceleration of protons [42] is dominant. Therefore the maximum energy starts to decrease at one point.

Allen *et al.* [48] determined the maximum proton energy for varying intensity ($1. - 5. \times 10^{18}W/cm^2$). The predictions of the model agree well with the experimental results although one has to note that an "appropriate" thickness could be chosen as it was not exactly specified by the experiment (see figure 5.12 (b)).

5.3.2 Experiments with a low contrast pre-pulse

For experiments with a low contrast pre-pulse ($I_{pre}/I_0 \geq 10^{-6}$) the corresponding references are summed up in table (5.2). Spencer *et al.* [61] investigated the dependence of the maximum energy on the target thickness as well as on the target material (figure 5.13 (a)). For the specified experimental parameters the model underestimates the

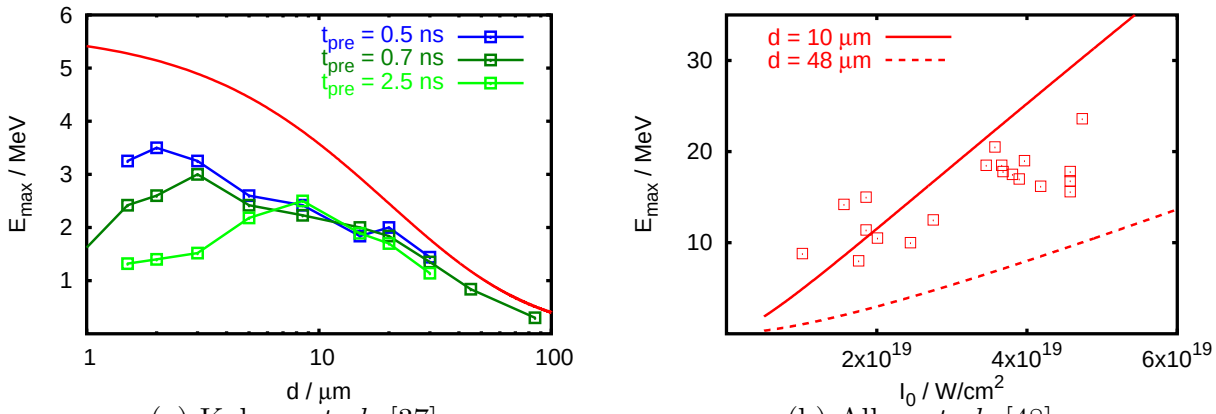

(a) Kaluza *et al.* [37] (b) Allen *et al.* [48]

Figure 5.12: (a) Dependence of the maximum energy on the target thickness for a laser pulse with $I_0 = 1. \times 10^{19} W/cm^2$, and $\tau_{las} = 150$ fs. The three experimental curves are assigned to different pre-pulse durations. (b) As Allen *et al.* do not specify exactly the target thickness for the measurement of the dependence on the intensity, the scaling of the model prediction for both possible thicknesses is given.

maximum proton energy. Besides the fact that the model predicts no maximum (compare to Kaluza *et al.* in subsection 5.3.1) in the TNSA regime for thick targets the energy predicted by the model is at least one order of magnitude smaller compared to the experiments.

Nemoto *et al.* [62] studied the dependence of the maximum energy on the laser intensity (figure 5.13 (b)). The model yields an increase in energy with intensity like in the experiment. However again the model underestimates the maximum energy by almost a factor of two.

The dependence of the maximum energy on the pulse duration is studied by Oishi *et al.* [63]. For the specified experimental parameters the model underestimates the proton energy (see appendix D.2.2) by at least a factor of 5. Though they compared their experimental results to Mora's model and found a good agreement, with the assumptions of section 5 no consistency with the model is found. Especially Oishi *et al.* do not explicitly specify the calculation of the plasma frequency which influences the maximum energy (see equation 3.17). In addition they use the same ion plasma frequency for all pulse durations, all target thicknesses and all intensities.

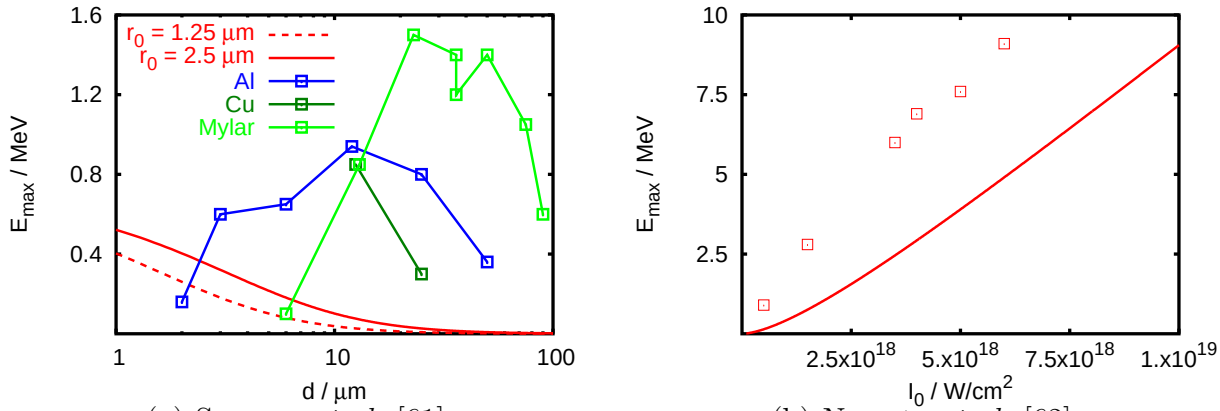

(a) Spencer *et al.* [61] (b) Nemoto *et al.* [62]

Figure 5.13: Maximum proton energy versus target thickness and intensity respectively. Spencer *et al.* (a) varied the target thickness between 2 μm and 90 μm for $I_0 = 7 \times 10^{19} W/cm^2$ and a pulse duration of $\tau_{las} = 60$ fs. Aluminum, copper and Mylar targets where used. Nemoto *et al.* (b) varied the intensity for a 400 fs laser incident on a 6 μm target.

5.3.3 Experiments with single data points

Experiments with only a few or a single data point are summarized in table (5.3). The comparison of the model with the experimental results shows that the maximum energy is always underestimated by a factor up to 5.

5.3.4 Discussion

The comparison of the model with experimental data from literature shows a good agreement to some extent. Especially for experiments for which the contrast of main and pre-pulse is large, various experiments are in line with the theoretical predictions. The data of experiments with a low contrast yield larger deviations from the model. The higher pre-pulse intensities naturally influence the pre-plasma as well as the target rear side. Therefore the initial situation when the main pulse reaches the target deviates stronger from the initial situation in the model. In several experiments the maximum energy is underestimated. In addition in the comparison to the experiments the characteristic acceleration time coefficient is assumed to be constant, $t = 1.3 \times \tau_{las}$.

The main challenge is to estimate the hot electron density which subsequently determines the plasma frequency and thus the parameter τ in equation (3.17). The calculation of the density is based on rough estimations regarding the number of electrons and the volume they spread over. In contrast to the simulations the parameters entering this calculation cannot be identified directly. But in spite of these deficiencies in many cases

Ref.	I_{18}	τ_{las}/ fs	$d/\mu m$	I_{pre}/I_0	$\lambda/\mu m$	$d_0/\mu m$	E_{max}/ MeV	E_{max}^{mod}/ MeV
[64]	50.	300	50	10^{-7}	1.053	8.15	25.	8.8
[2]	300.	500	100.	10^{-4}	1.	9.	58	41.
[65]	7.3	450	100.	10^{-3}	1.053	2.5	8.2	1.7
[66]	6.	50	5.	10^{-5}	0.8	18.	1.	0.26
[35]	60.	40	6.	10^{-6}	0.820	4.	10.	2.4

Table 5.3: Maximum energies adapted from Hegelich *et al.* [64], Snavely *et al.* [2], Murakami *et al.* [65], Matsukado *et al.* [66], Fritzler *et al.* [35], various experiments in comparison with the predictions of the theoretical model. The intensities (I_{18} in $10^{18}W/cm^2$) cover a wide range, $I_0 = 6. \times 10^{18}W/cm^2$ up to $I_0 = 3 \times 10^{20}W/cm^2$. For Hegelich *et al.* the spot radius is calculated by assuming that 40% of the specified laser energy $E_{las} = 30$ J results for $\tau_{las} = 300$ fs in an intensity of $I_0 = 5. \times 10^{19}W/cm^2$.

the model predicts the right dependency of the maximum energy on another parameter and the order of magnitude.

5.4 Conclusions and outlook

The analytical model proposed by Fuchs *et al.* [52] is compared to one- and two-dimensional PIC simulations as well as to experimental data from literature. For one-dimensional simulations a good agreement is found for a wide range of parameters with the extension of a characteristic acceleration time coefficient depending on the pulse duration, $t = R\tau_{las}$ with $R = (111. \pm 21.) \times \tau_{las}^{-0.86\pm0.035}$. However for a few set-ups (e.g. long laser pulses on thick targets) the model deviates from the simulation results.

In two dimensions a limited number of simulations is performed. A similar exponent for the dependence of the characteristic acceleration time coefficient on the pulse duration is found and the model agrees well with the simulation results.

The comparison of the model with experiments shows partly consistency and partly deviations. This is based on the fact that the hot electron density which is essential for prediction of the maximum energy, is calculated by rough estimations. But nevertheless the model provides a general understanding of the scaling of the maximum energy. Additionally the order of magnitude of the maximum energy is given.

To estimate the approximate intensity which is needed to obtain clinically usable proton energies of more than 200 MeV, the model is applied to various parameter sets. The full width at half maximum of the focal spot is $d_0 = 10$ μm, the opening angle is assumed to be $\Theta = 25°$ and the pulse length is $\tau_{las} = 40$ fs. E.g. for a target thickness of 10 μm and a characteristic acceleration time coefficient $R = 2$ an intensity of $5 \times 10^{21}W/cm^2$, which only moderately exceeds the intensity of soon operating Petawatt

laser systems [55], results in a maximum energy of 255 MeV. For $R = 1$ this reduces to 120 MeV. For a target thickness of 55 μm an intensity of $2.5 \times 10^{22} W/cm^2$ is needed to obtain 275 MeV ($R = 2$) and 100 MeV ($R = 1$) respectively.

6 Set-ups with two lasers and two targets

In general the energy spectrum of laser-accelerated protons shows a typical Maxwellian shape with a maximum energy (see for instance figure 3.5). Hence the highest energy conversion efficency is achieved to the lowest-energy particles. For applications, particularly for the use in radiotherapy, a monochromatic proton beam or at least some degree of control on the overall shape of the energy spectrum would be highly desirable. Ideally, one would like to find a way to optimize the laser-to-proton energy conversion efficiency into a finite proton energy range. But even if it is at the expense of a lower efficiency, being able to tailor the proton spectrum "at the source" would be most useful. Most notably, it may suppress the need to devise and use a particle energy selection apparatus [67, 68], a "macroscopic object" which may well destroy the otherwise interesting properties of the proton beam that are its short duration and small source size.

The underlying idea is that large transient electric fields at the source are used to control the spectrum. These fields are created by the interaction of a second laser with a second target. Figure 6.1 shows the basic set-up. The first laser is incident from the left and focused on a proton-electron target. The interaction drives the acceleration of protons. A second target made of heavy ions is placed at a distance d behind the first target. Protons accelerated in forward direction will cross the second target after a certain time. Thereby the fastest protons will reach the second target first. When these fastest protons have crossed the second target a second laser is hitting this foil. The heating of the second target electrons will generate a large negative electric field at the left hand side of the heavy ion target and a large positive electric field at the right hand side. Hence the lower energetic protons will be reflected and the particles which have crossed the target will experience an additional acceleration. In section 6.1.3 this process will be depicted on the basis of simulation results.

6.1 1D PIC simulations

To investigate the above described mechanism one-dimensional simulations are performed. The two lasers have both a cosine squared temporal shape with a total pulse duration of $\tau^I_{las} = \tau^{II}_{las} = 136\ 1/\omega_0$. The first pulse is operating at an intensity with $a^I_0 = 8.5$ while the second pulse, which is incident from the right end of the box, is more intense and delivers $a^{II}_0 = 12$. The delay between the two lasers, $\Delta\tau$, is defined as the

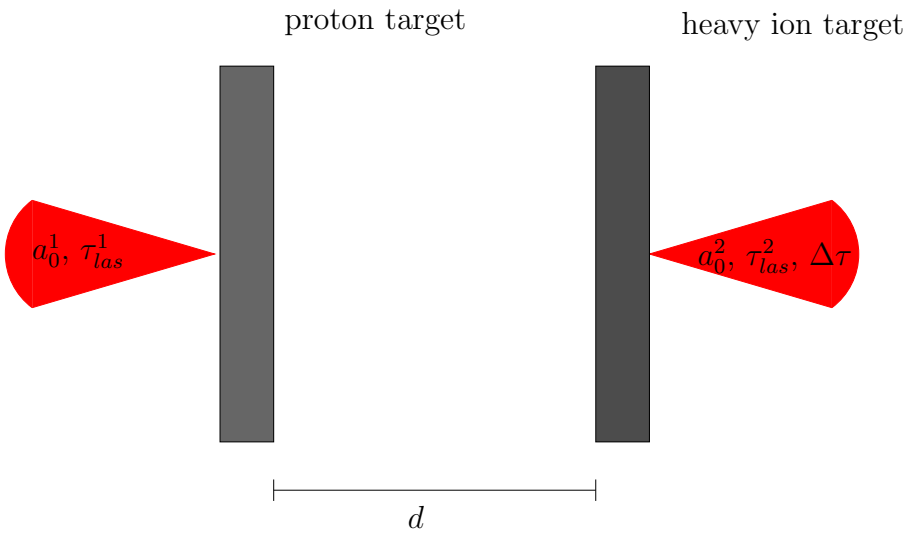

Figure 6.1: The basic two targets - two lasers set-up: The first laser with a_0^I and τ_{las}^I, is incident from the left onto the first target. The interaction of the laser with this proton-electron plasma drives the acceleration of protons. When the fastest protons have crossed the second heavy ion target, a second laser (a_0^{II}, τ_{las}^{II}) hits this target with a delay of $\Delta\tau$. The targets are separated by distance d.

distance of the arrival of the maximum of the second laser at the second target and the supposed arrival of the maximum of the first pulse at the second target.

The first target is consisting of hydrogen. It is $d_I = 4.3\ c/\omega_0$ thick and has a density of $n_I = 40\ n_c$. The second target is made of $n_{II} = 40\ n_c$ high atomic number material ($m_{II} = 30\ m_p$) with a thickness of $d_{II} = 6.3\ c/\omega_0$.

The simulations are performed in a simulation box with $L = 9000\ c/\omega_0$, a mesh size of $\Delta x = 0.1\ c/\omega_0$ and a time step length of $\Delta\tau = 0.06\ 1/\omega_0$. The number of particles per cell is very large ($NPC = 2000$) as the simulations are long-lasting and features of a small amount of particles (namely the fastest protons) are studied. The initial electron, proton and ion temperature is chosen to be zero. Furthermore the positions of the particles are initialized so that the charge density is zero throughout the whole simulation box. These initial conditions are chosen to avoid that the plasma expansion - due to an initial electron temperature - which takes place before the pulses arrive does not influence the simulation, e.g. the absorption of the laser or the density gradient at the rear surface (compare to section 5.1.1). Therefore it is possible to compare set-ups with different time delays without any influence of the initial plasma expansion.

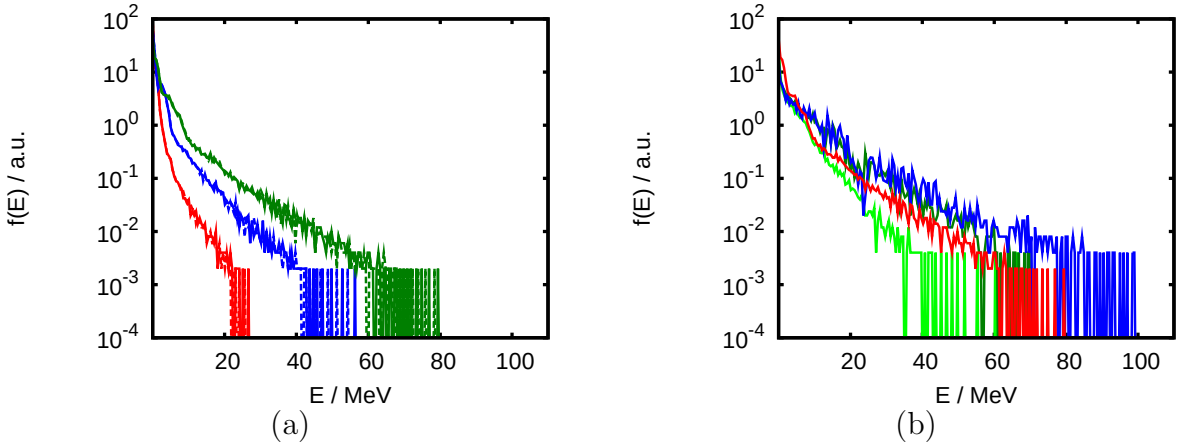

Figure 6.2: (a) A second target placed behind the irradiated first one does not change the energy spectrum (solid lines represent single target and dashed lines the two target set-ups). With increasing intensity the maximum energy is increasing ($a_0^I = 8.5 \mathrel{\widehat{=}}$ red, $a_0^I = 12. \mathrel{\widehat{=}}$ blue, $a_0^I = 14.7 \mathrel{\widehat{=}}$ green). (b) The energy spectrum of a two lasers - one target set-up is changed by the delay between the two pulses (light green: $\Delta\tau = -120\ 1/\omega_0$, dark green: $\Delta\tau = 600\ 1/\omega_0$, blue: $\Delta\tau = 1000\ 1/\omega_0$, red: single pulse with $a_0 = 14.7$ as reference).

6.1.1 One laser, one/two target(s)

To obtain reference spectra of single laser shots on single targets, simulations with $a_0^I = 8.5$, the double intensity, $a_0^I = 12.$, as well as with the threefold intensity, $a_0^I = 14.7$, are performed. The energy spectra show the typical Maxwellian shape with a cut-off energy (figure 6.2 (a)). For the lowest intensity 6.1 % of the laser energy are absorbed by the plasma and the protons reach energies up to 27 MeV. For $a_0^I = 12./14.7$ the maximum energy increases to 57/80 MeV and the absorption also grows to 9.5/12.2 %. When a second target is added, $d = 120\ c/\omega_0$ behind the first one, the energy spectra and absorption are hardly changed (figure 6.2 (a)). The electrons of the second target are slightly heated and an expansion of the second target occurs. The energies of the ions of the second target are below 1 MeV.

6.1.2 Two lasers, one target

To study the influence of a second laser, simulations with two lasers incident on a single target are carried out ($a_0^I = 8.5$, $a_0^{II} = 12.$). The second laser (incident from the left) which is hitting the target with a given delay $\Delta\tau$ is then interacting with a target that already performs a plasma expansion. Three different delays, $\Delta\tau = -120\ 1/\omega_0$ (the "distance" to the second, absent target is set to $d = 120\ c/\omega_0$, i.e. the second laser

hits the target 120 $1/\omega_0$ after the first one), $\Delta\tau = 600\ 1/\omega_0$ and $\Delta\tau = 1000\ 1/\omega_0$, are compared to a single pulse simulation. The Maxwellian shape of the spectra is still present but the maximum energy as well as the number of particles accelerated to high energies is changed (figure 6.2 (b)). Due to the interaction with the underdense part of the expanding plasma the absorption is higher than for a single pulse ($a_0^I = 14.7$) which carries the same total energy. The absorption increases from 12.4 % in the single pulse case, to 15.3 % ($\Delta\tau = -120\ 1/\omega_0$), 33. % ($\Delta\tau = 600\ 1/\omega_0$) and 39. % ($\Delta\tau = 1000\ 1/\omega_0$) respectively. The maximum energy for $\Delta\tau = -120\ 1/\omega_0$ and $\Delta\tau = 600\ 1/\omega_0$ is reduced to 60 MeV and 70 MeV compared to 80 MeV in the single pulse case. For a delay of $\Delta\tau = 1000\ 1/\omega_0$ however the maximum energy increases to 100 MeV. In addition even if the maximum energy is slightly reduced for $\Delta\tau = 600\ 1/\omega_0$ the number of particles with high energies is enhanced.

6.1.3 Two lasers, two targets

To investigate the effect of two targets using two lasers two series of simulations are performed. In the first one the distance is kept constant at $d = 120\ c/\omega_0$. The delay is varied between $\Delta\tau = 0\ 1/\omega_0$ and $\Delta\tau = 1300\ 1/\omega_0$. In a second series of simulations the distance between the two targets is varied from 90 c/ω_0 to 240 c/ω_0. The respective time delay is chosen so that for all distances the momentum of the protons at the second target (due to the expansion of the first one) is the same when the maximum of the second pulse hits the second target.

Basic mechanism

To illustrate the basic mechanism which affects the energy spectrum when the second target is hit by a second pulse, here an exemplary simulation is presented. The delay is chosen to be $\Delta\tau = 800\ 1/\omega_0$. In the beginning (figure 6.3 (a)) the $q_x p_x$-phase space of the first target is showing the typical characteristics of an expanding foil. The fastest protons have departed farthest from the target center leading to a slightly curved diagonal in the phase space. When the second pulse hits the second target electrons are heated. Hence a large electric field is created, negative at the left hand side and positive at the right hand side. This field decelerates particles which just arrive at the second target and gives an additional acceleration to protons which have crossed the foil (figure 6.3 (b)). In the further course of the simulation the low energy protons are reflected at the second target and the high energy part is separated (part (c) and (d) of the figure).

However this “quasi-monoenergetic” feature does not hold in the long run. Due to the reflection of the low energy protons an accumulation of density in front of the second target occurs (figure 6.4 (a)). The corresponding sharp density gradient drives a second expansion resulting in an energy gain of the low energy protons (figure 6.4 (b)). The gap in the energy spectrum is getting narrower and narrower and closes at the end.

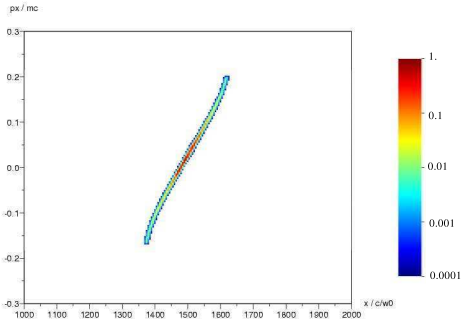

(a) $q_x p_x$-phase space at 2400 $1/\omega_0$

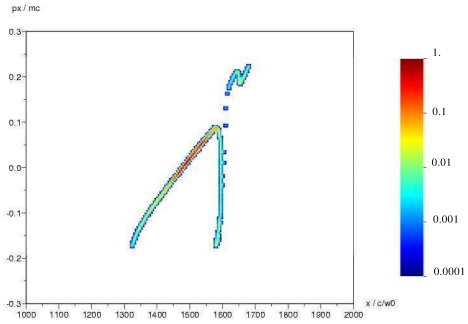

(b) $q_x p_x$-phase space at 2700 $1/\omega_0$

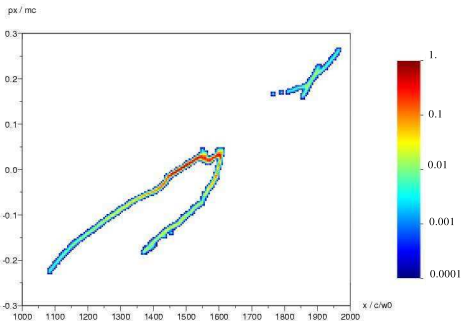

(c) $q_x p_x$-phase space at 3900 $1/\omega_0$

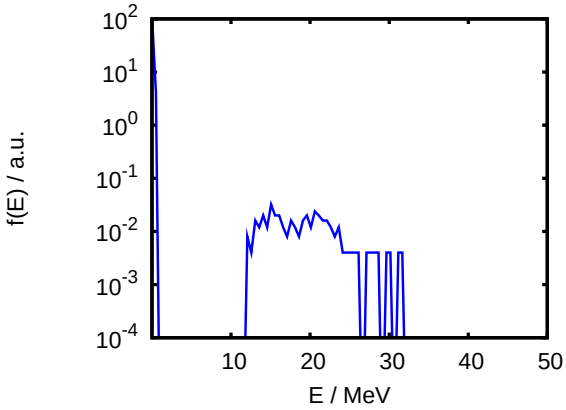

(d) Energy spectrum at 3900 $1/\omega_0$

Figure 6.3: Phase spaces and energy spectrum for various simulation times ($t = 0$ $1/\omega_0$ corresponds to the arrival of the first pulse at the first target) of a two lasers - two targets set-up. The first laser ($a_0^I = 8.5$) is incident on the left target, placed at $x = 1480$ c/ω_0. The second laser ($a_0^{II} = 12.$) is hitting the second target (at 1600 c/ω_0) with a delay of $\Delta\tau = 800$ $1/\omega_0$. The color scale is given in arbitrary units.

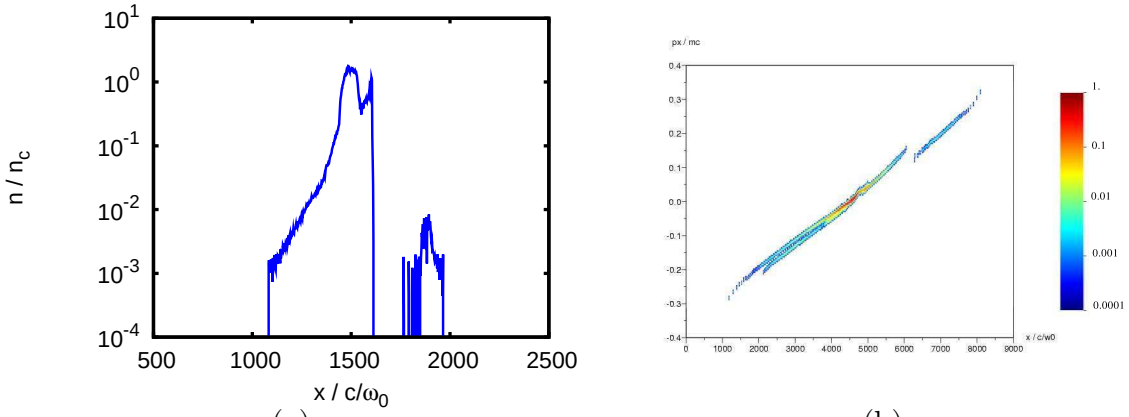

(a) (b)

Figure 6.4: The reflection of low energy particles leads to a peak in the proton density (a). This is driving a second expansion so that in the long run the gap in the momentum is closed (b) (note the division of the phase space with negative momentum into two parts indicating the second expansion).

Variation of time delay

The time delay for the above described set-up is varied between $\Delta\tau = 0\ 1/\omega_0$ and $\Delta\tau = 1300\ 1/\omega_0$. At first e.g. the energy spectra for $\Delta\tau = 800\ 1/\omega_0$ and $\Delta\tau = 1300\ 1/\omega_0$ show an increase in the maximum energy compared to the spectrum of a single pulse (figure 6.5 (a)).

This is due to the re-heating of the electrons which drive the plasma expansion by the second laser pulse. The reflection of particles at the second target leads to a reduction of the number of low energy protons. For $\Delta\tau = 800\ 1/\omega_0$ the spectrum shows an exponential decrease up to 7.5 MeV and an additional plateau up to the maximum energy of around 50 MeV. In the case of $\Delta\tau = 1300\ 1/\omega_0$ the exponential decrease is limited by a minimum at 3.4 MeV in the spectrum followed by a maximum at 7. MeV and a further exponential decrease up to the maximum energy of 50 MeV.

To illustrate the change in the energy spectrum the relative cumulative energy density

$$F(E) = \frac{1}{E_{tot}} \int_0^E f(E')E'dE' \tag{6.1}$$

is computed. This is characterizing how much of the total energy is stored in protons with energies below a given value. Hence the "optimal" spectrum $f(E) \propto \delta(E - E_0)$ would result in the step function $F(E) = \Theta(E - E_0)$ for the relative cumulative energy density.

Obviously for set-ups with two lasers and two targets more energy is stored in the high energy region (figure 6.5 (b)). While in the single target case only 1. % of the total

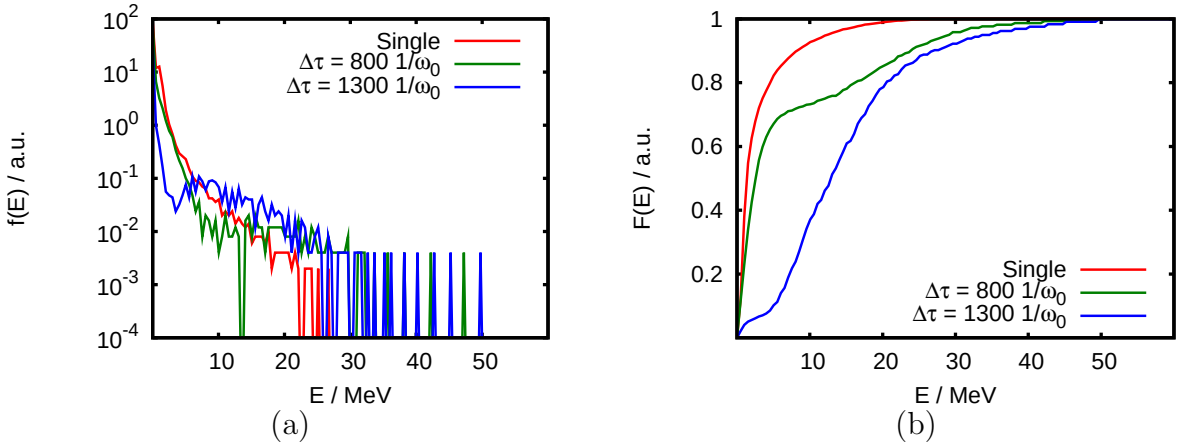

Figure 6.5: (a) Energy spectra and (b) cumulative relative energy density, F(E), for two lasers - two targets set-ups compared to a single laser case.

energy is stored above 20 MeV for delays of $\Delta\tau = 800\ 1/\omega_0$ and $\Delta\tau = 1300\ 1/\omega_0$ 15 % respectively 20 % of the energy is stored in this range.

Variation of distance

In a second series of simulations the distance between the two targets is varied. The delay between the two pulses is chosen in that way that the momentum of the protons crossing the target at the moment of the arrival of the maximum of the second laser pulse is the same for all distances. Two different delays, $\Delta\tau = 800\ 1/\omega_0$ and $\Delta\tau = 1200\ 1/\omega_0$, are chosen as a reference for a distance of 120 c/ω_0. This transfers into delays of 625/925 $1/\omega_0$ ($d = 90\ c/\omega_0$), 970/1500 $1/\omega_0$ ($d = 150\ c/\omega_0$) and 1475/2380 $1/\omega_0$ ($d = 240\ c/\omega_0$) for the respective delays.

In the case of the shorter delay the energy spectra and the relative cumulative energy density show almost the same behavior for $d = 90\ c/\omega_0$, $d = 120\ c/\omega_0$ and $d = 150\ c/\omega_0$ (figure 6.6). The energy spectrum is altered in the same way as the electric field arising at the second target is "dividing" the phase space at the same "position". For $d = 240\ c/\omega_0$ this feature does not hold. As the delay is much longer the expansion is gone much further and the absorption of the second pulse is changed.

The same trend (denoted by the curved shape of $F(E)$) is visible in the comparison of the corresponding set-ups for the reference delay of $\Delta\tau = 1200\ 1/\omega_0$ for $d = 120\ c/\omega_0$ (figure 6.7). But the correlation between the curves for $d = 90\ c/\omega_0$, $d = 120\ c/\omega_0$ and $d = 150\ c/\omega_0$ is by far not as close as in the case of the shorter delay. However the shape of the curves looks almost the same. For $d = 240\ c/\omega_0$ again the situation changes ($F(E)$ yields no curvature for low energies) as the absorption is increasing due to the long-lasting expansion before the arrival of the second pulse.

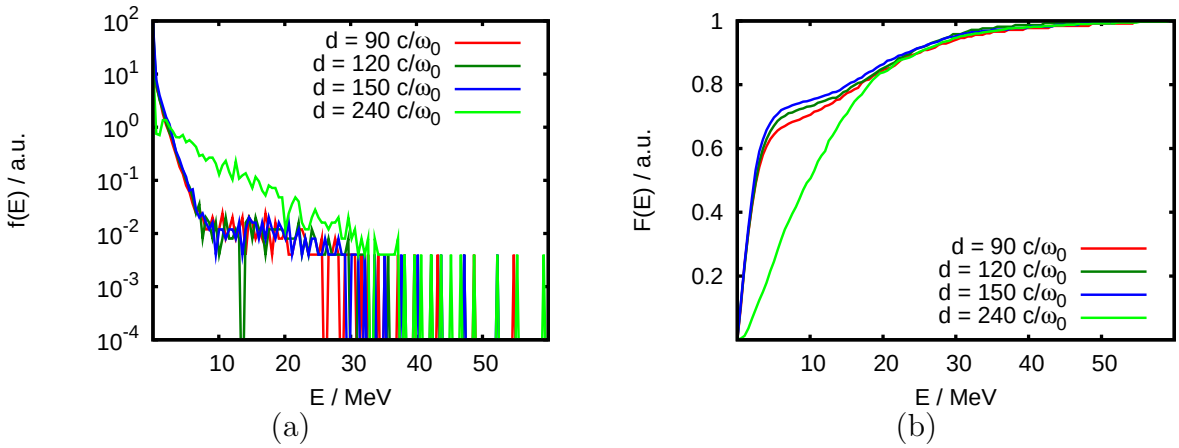

Figure 6.6: (a) Energy spectra and (b) cumulative relative energy density, F(E), for two lasers - two targets set-ups for different target distances. The reference case is $d = 120\ c/\omega_0$, $\Delta\tau = 800\ 1/\omega_0$.

6.2 Conclusions

The possibility of controlling the normally Maxwellian shaped energy spectrum of laser-accelerated protons by a set-up with two lasers and two targets is studied by one-dimensional PIC simulations. Due to the generation of large transient electric fields by the interaction of a second laser at the second target, the energy spectrum of protons originating from the first one can be modified. Lower energy particles are reflected while high energy particles gain an additional acceleration. Shortly after the interaction this results in an proton energy distribution with a "quasi-monoenergetic" high energy part. However due to the reflection at the second target a steep density gradient occurs which drives a second expansion. This leads to an re-acceleration of the low energy particles and the gap in the energy spectrum closes in the long run of the simulation.

However a modification of the energy spectrum still remains. The number of particles with low energies is reduced while the number of high energetic particles is increased. E.g. for a single target only 1% of the total proton energy is stored in protons with energies larger than 20 MeV, while for a delay between the two pulses of $\Delta\tau = 800\ 1/\omega_0$ the fraction can be increased to 15% and for $\Delta\tau = 1300\ 1/\omega_0$ to 20%.

The variation of the distance between the two targets shows that the modification of the energy spectrum is correlated to the "position" where the phase space of the first protons is "divided" by the electric field at the second target. If this "position" is equal for different target distances the resulting energy spectrum is the same. An exception however is the situation of a long-lasting first plasma expansion as the electrons are strongly re-heated by the second laser pulse and therefore the energy spectrum is

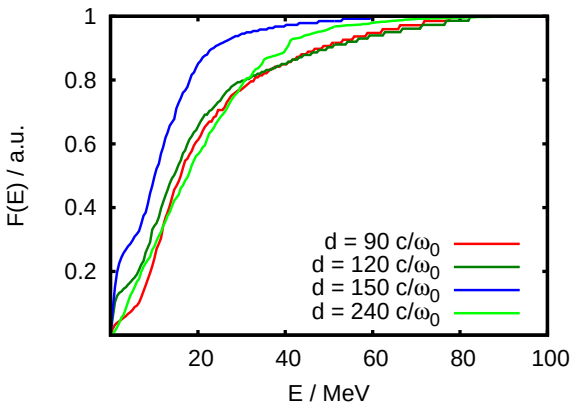

Figure 6.7: Cumulative relative energy density for different target distances. The reference case is $d = 120\ c/\omega_0$, $\Delta\tau = 1200\ 1/\omega_0$.

completely changed.

The assumption of an easy and satisfactorily modification of the normally Maxwellian energy spectrum by two lasers - two target set-ups couldn't be confirmed. The efficiency of laser-to-proton energy conversion is increased for high energy protons, but far away from delivering "quasi-monoenergetic" proton beams. A further detailed investigation of the phenomenon in two dimensions might be useful to evaluate if the effect of the second expansion is more moderate. However first preliminary studies in two dimensions were not promising as additional limitations arise. E.g. due to the transversal limitation of the laser pulse the electric field at the second target is transversally inhomogeneous. Hence as a result of the divergence of the proton beam originating from the first target, protons with the same energy do not experience the same electric field. The energy spectrum shows - even at early simulation times - no clear "quasi-monoenergetic" part.

A more promising way to tailor the spectrum "at the source" seems to be the so-called double-layer targets presented in the next chapter.

7 Double-layer targets

Typically laser-accelerated protons show a Maxwellian energy spectrum (e.g. figure 3.5 (b) in chapter 3). However these spectra are inadequate for radiotherapy as the low energy part would deliver unacceptable dose at small depths when treating a deep-seated tumor. To overcome this problem one might use a compact particle selection system [67, 68]. Since this requires a macroscopic device a tailoring of the energy spectrum at the source would be preferable. Esirkepov *et al.* [10] proposed the so-called double-layer targets to overcome this problem. These were successfully realized by Schwoerer *et al.* [11] and Hegelich *et al.* [12].

In this chapter[1] the underlying physics and possible application to radiotherapy of double-layer targets is studied. At the beginning the effect is studied by means of simple plasma expansion simulations. The influence of various target constituents is studied and compared to an one-dimensional analytical model [56]. Subsequently the studies are extended to one- and two-dimensional PIC simulations of the interaction of a laser pulse with a double-layer target (section 7.2). Afterwards the obtained findings are used as a basis for a comparison of treatment plans for protons originating from double-layer targets and conventional photon beams (section 7.3).

7.1 Plasma expansion of double-layer targets

To investigate the influence of various target parameters on the proton beam characteristics at first plasma expansion simulations are performed. Instead of simulating the interaction of a laser and a plasma, a hot electron population is initially assigned to the double-layer. Hence absorbing and heating processes are neglected whereas it is ensured that the system is always prepared with the same initial conditions (such as hot electron temperature and hot electron density). This allows to study the effect of target constituents on the proton beam characteristics independently of effects caused by the laser-plasma interaction (e.g. change in the absorption due to varying the ion mass of the front layer).

In section 7.2 the main characteristics found for the plasma expansion simulations are investigated for various laser-plasma set-ups.

[1] The studies of this chapter were carried out in conjunction with a diploma thesis and largely published in [69].

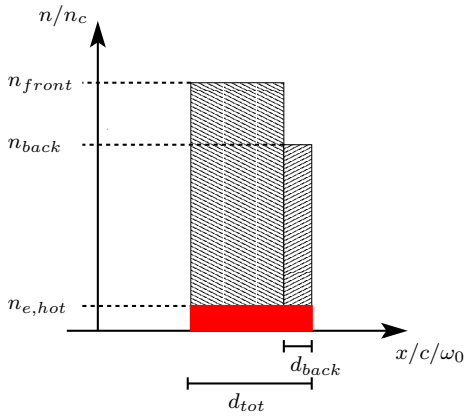

Figure 7.1: The double-layer target with a total thickness of $d_{tot} = 30\ c/\omega_0$ consists of two parts. The front layer is composed of ions ($m = 1 \ldots 48 \cdot m_p, \infty$) with a density of $n_{front} = 15\ n_c$. The rear side with thickness d_{back} is made of protons with a density of $n = 15\ n_c$ or $n = 1.5\ n_c$. The electrons are initially divided into two components. A hot population with temperature $T = 1$ MeV and density $n = 1.5\ n_c$ and moreover a cold population whose density is chosen such that the complete target is neutral in charge.

7.1.1 Simulation parameters

All simulations are performed for a double-layer target with a total thickness of $d_{tot} = 30\ c/\omega_0$ (figure 7.1). The density of the front layer is kept constant ($n_{front} = 15\ n_c$) while the ions' mass is varied, $m = 1 \ldots 8 \cdot m_p$, $m = 27\ m_p$ (aluminum) and $m = 48\ m_p$ (titanium) as well as $m = \infty$ (i.e. fixed ions). Furthermore the density of the second layer ($n = 15\ n_c$ and $n = 1.5\ n_c$) as well as the thickness ($d_{back} = 0.05 \ldots 5\ c/\omega_0$) is changed. The electrons consist of a cold ($T = 0$ MeV) and a hot part with a temperature of $T_{e,hot} = 1$ MeV and a density of $n_{e,hot} = 1.5\ n_c$. These are typical values for a hot electron population created by a laser-plasma interaction with today's laser intensities.

7.1.2 Proof of principle simulations

First of all the dependence of the energy spectrum on the thickness of the thin proton layer at the back is studied. For this purpose the front as well as the back layer consist of protons ($n = 15\ n_c$). Hence no separation will occur and the simulations only provide information about the energies of protons placed at a given "depth" inside the target. For this purpose the thickness of the rear layer is varied between 0.05 c/ω_0 and 5 c/ω_0.

The proton energy spectra (figure 7.2) of the rear layer show a clear separation from the front layer. The minimum cut-off energy of the back side corresponds to the maximum energy of protons in the front of the target. With increasing thickness of the layer at the back the corresponding minimum energy is decreasing (figure 7.3 (a)). For the thinnest

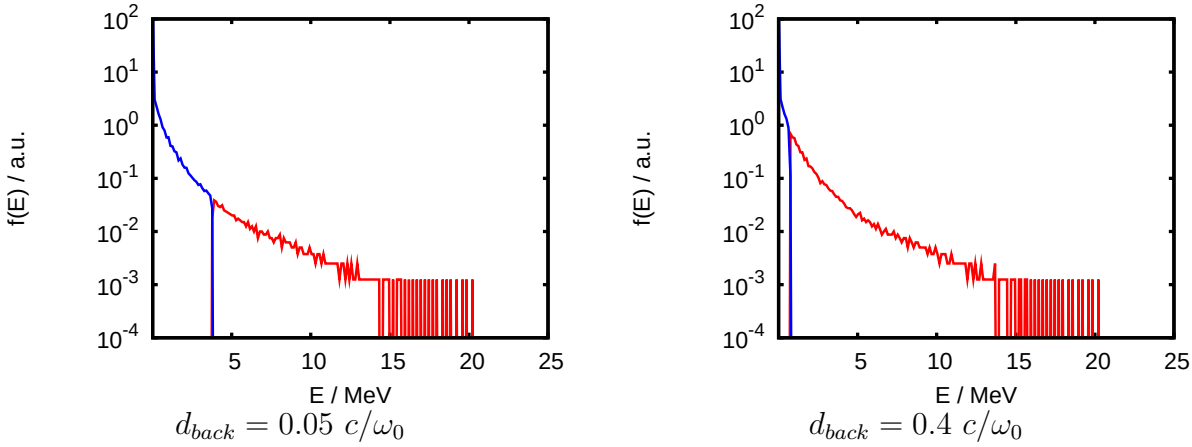

Figure 7.2: The energy spectra of forward going protons (i.e. in the direction of the laser pulse) of the front side (blue) show a clear maximum energy cut-off. This energy corresponds to the minimum energy of the rear side protons (red).

layer with a width of 0.05 c/ω_0 the minimum energy is 3.7 MeV. It is decreasing to 0.6 MeV for 0.4 c/ω_0 and vanishing for $d_{back} = 0.8\ c/\omega_0$. These results imply that the "deeper" a proton is placed inside the target the smaller its final energy will be. Hence for a narrower energy spectrum one selects thin proton layers.

7.1.3 Dependency on target constituents

In the previously studied simulations no separation of the target front and back layer occurs. Following the idea of Esirkepov *et al.* [10] (see also 3.4.1) the mass of the front layer ions is increased, $m = 1 \ldots 8, 27, 48 \cdot m_p, \infty$, to ensure separation and enhance the acceleration efficiency of the rear layer. As the narrowest energy spectrum in the simulations in the previous section is obtained for the thinnest proton layer, the following simulations are confined to $d_{back} = 0.05\ c/\omega_0$.

Energy spectra

Unfortunately the resulting energy spectra show undesirable properties. The minimum energy is actually decreasing with increasing ion mass (figure 7.3 (b)). For a front layer consisting of protons a minimum energy cut-off of ~ 4 MeV is obtained. This cut-off decreases rapidly with increasing mass. For titanium a low cut-off is still present while for fixed ions ($m = \infty$) the minimum energy is vanishing. In contrast the maximum energy is slightly increasing with increasing mass.

The temporal development of the minimum and maximum energy (figure 7.4 (a)) shows the difference between a double-layer with protons and another one with infinitely

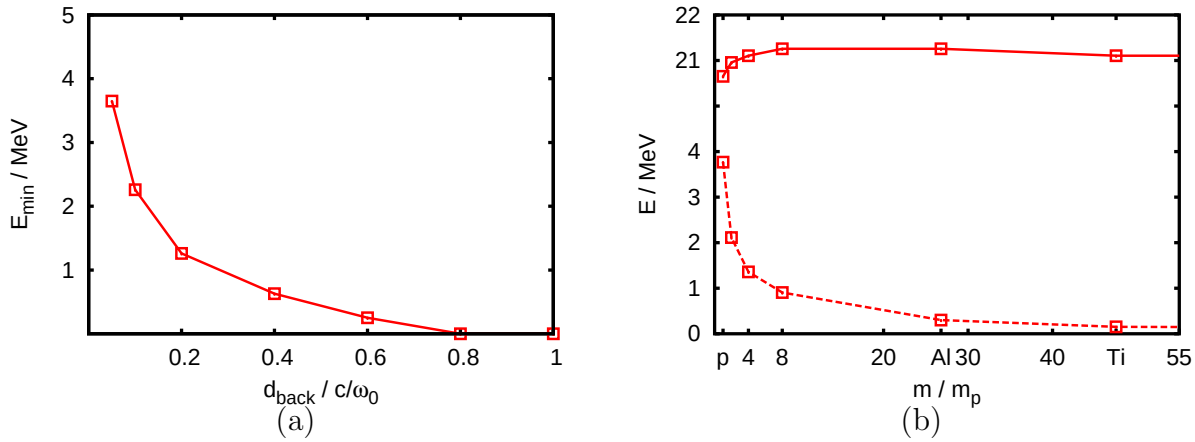

Figure 7.3: (a) The minimum energy cut-off for proton targets with a total thickness of 30 c/ω_0 vs. the thickness of the rear proton layer. (b) The minimum energy (dashed line) of the proton bunch is decreasing rapidly with increasing mass. The maximum energy (solid line) is almost constant ~ 21 MeV.

heavy ions in the front. After an initial increase of the minium energy in the case of fixed ions the cut-off is decreasing with time in contrast to the proton case. At the end of the simulation it is completely vanished. Additionally the maximum energy is slightly enlarged for fixed ions.

Expansion of the proton bunch

The deceleration is due to an expansion of the proton bunch. The hot electrons accompanying the proton layer do not balance the local proton charge density. This is caused by the fact that only a small amount of electrons can escape from the target while most electrons are captured by the fixed substrate. Hence the propagating proton layer is non-neutral and expanding in its center of mass frame. This results in a decrease of the minimum energy as well as in an increase of the maximum energy.

To verify this explanation a simulation is carried out where the density of the thin layer at the back is reduced to $n = 1.5\ n_c$. As the charge excess in the propagating layer is reduced the minimum cut-off energy is not vanishing anymore and of the order of the cut-off for the proton case (figure 7.4 (b)).

The comparison of the electric fields and electron as well as proton densities (figure 7.5) shows that in the case of fixed ions in the front and high density coating a decelerating field occurs on the left hand side of the propagating layer. The hot electrons accompanying the propagating layer for fixed ions do not balance the charge of the layer leading to a dip in the electric field (figure 7.5 (b)). In the case of free protons in the

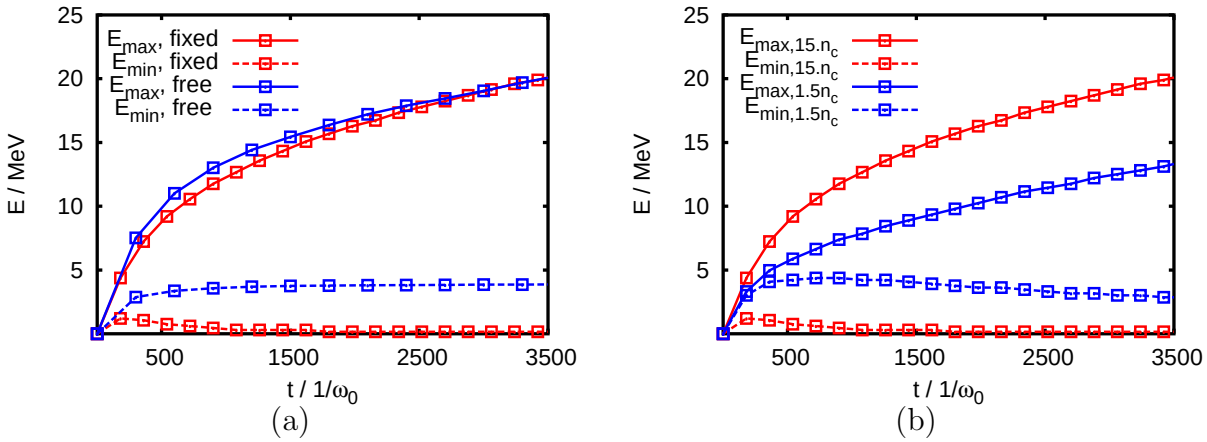

Figure 7.4: (a) The minimum proton energy for a double-layer target with infinitely heavy ions at the front is at first increasing. In contrast to the double-layer target with protons at the front the cut-off is decreasing with time and vanishing at the end. (b) The minimum energy for a double-layer target with a low density coating is decreasing more weakly compared to the high density case. At the end of the simulation one ends up with a non-vanishing cut-off.

front the electron cloud is traveling with the layer and able to balance the charge. Thus no negative electric field occurs (figure 7.5 (a)).

The reduction of the density of the proton layer at the back reduces the size of the dip (figure 7.6). In the case of a high density coating even at early times (part (a)) the dip in the electric field is so large that negative and therefore decelerating fields appear. For later times this feature still holds whereas the difference in the dip is decreasing (part (b)).

7.1.4 Comparison to Albright's model

The model of Albright *et al.* [56] (for details see section 3.4.2) describes the isothermal propagation of a point-like proton layer initially attached to a heavy ion substrate. In dimensionless variables the system is characterized by Poisson's equation

$$\varphi'' = \exp(\varphi) - q\delta(\xi - \xi_L) - \Theta\nu(\xi) \tag{7.1}$$

with normalized potential φ, proton layer charge q, layer position ξ_L and substrate density Θ. Starting from this equation the potential and therefore the electric field can be computed (equations (3.30)-(3.35)). Though in the aforementioned simulations the layer is expanding a comparison to the model provides a deeper insight into the physical processes.

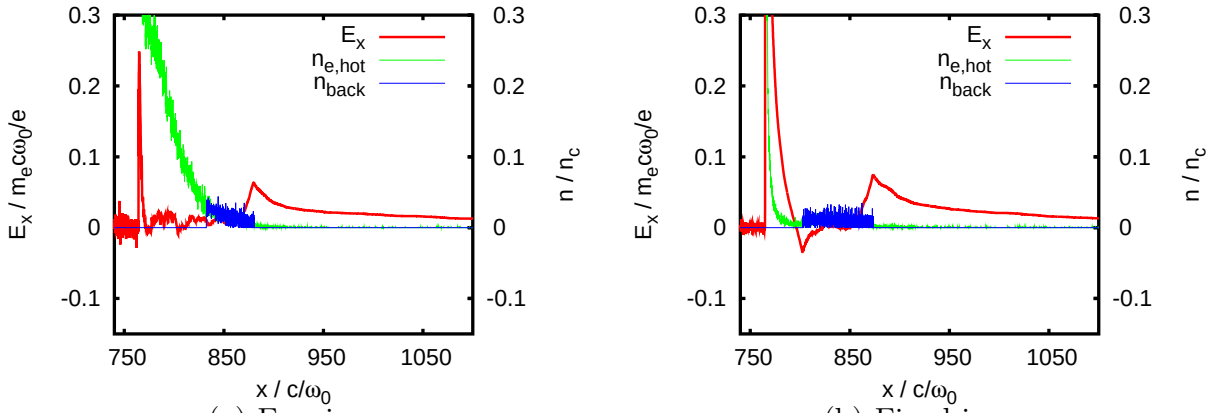

(a) Free ions (b) Fixed ions

Figure 7.5: The electric field as well as the proton layer and hot electron densities at $t = 900\ 1/\omega_0$ for fixed and free protons in the front. The proton layer density is $n_{back} = 15\ n_c$. As the hot electrons do not balance the proton layer density for fixed ions, decelerating fields occur.

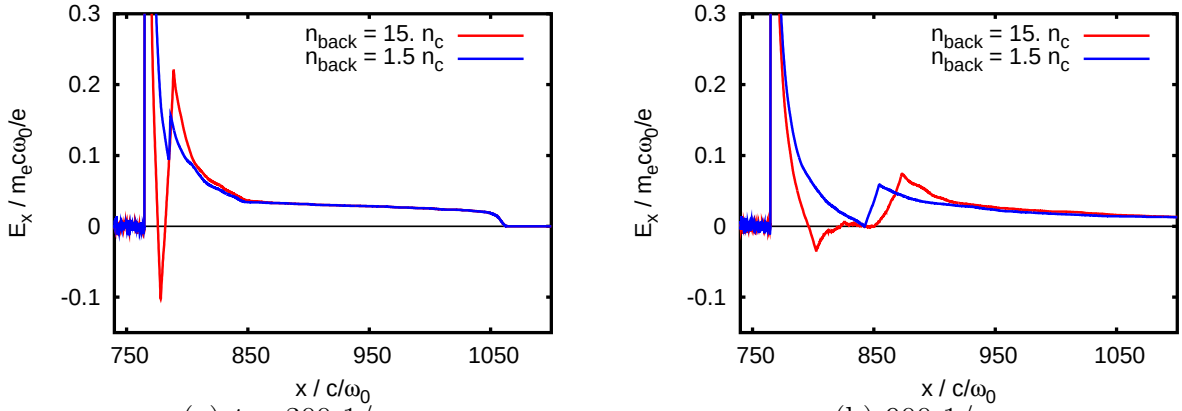

(a) $t = 300\ 1/\omega_0$ (b) $900\ 1/\omega_0$

Figure 7.6: The electric fields for high and low density coatings at $t = 300\ 1/\omega_0$ and $t = 900\ 1/\omega_0$. The "dip" in the electric field is smaller in the low density case and no decelerating fields occur until $900\ 1/\omega_0$.

Two representative simulations for fixed ions in the front layer are compared to the model. One case of high density coating and one for a low density proton layer. The previous simulation parameters, $n_{front} = n_{back} = 15\ n_c$, $n_{e,hot} = 1.5\ n_c$, $d_{back} = 0.05\ c/\omega_0$ translate into the dimensionless variables $q \simeq 0.437$ and $\Theta = 10$ whereas for $n_{back} = 1.5\ n_c$ the proton layer charge reduces to $q \simeq 0.044$.

Comparison of electric fields

The electric fields of the simulations for an early and a late acceleration time (figure 7.7) are in good agreement with the model. Especially in the low density case (part (b) and (d)) the analytical electric field outside the layer matches the one of the simulation. The appearance of decelerating fields at the target edges is also described. One difference is of course the discontinuity of the electric field in the model due to the non-expanding layer. The jump is proportional to the charge of the layer ($\Delta E \propto q$) and constant for all layer positions in the model. In the simulations however the discontinuity is "stretched" on the whole expanded layer. Secondly in the simulations the difference between the maximum and the minimum electric field at the layer edges is decreasing with time (more evident in the high density case (part (a) and (c))). This is based on the second main difference between the simulations and the model. Whereas in the model the layer is propagating in an isothermal system, in the simulations the electrons cool down. Hence the expanding layer can capture more easily electrons and the positive charge excess in the layer is reduced.

Comparison of minimum and maximum energies

As the analytically determined electric fields at the target edges are in good agreement with the simulations one can determine the energy of the left- and the rightmost proton iteratively. Because these are the protons with the highest and the lowest energy the model gives a prediction of the energy spread.

In the iterative process in each step the electric field for a point-like layer placed in the middle of the left- and the rightmost proton, i.e. at position $\xi_L = (x_{max} - x_{min})/2$, is numerically computed (details in section 3.4.2 on page 33). The particles are moved by the corresponding forces resulting in new positions and velocities. At the beginning, for rapidly changing fields, the iteration step is $\delta t = 1\ 1/\omega_0$. When negative electric fields occur the change in the electric fields is moderate and the time step is changed to $\delta t = 15\ 1/\omega_0$.

Similar to the electric fields the energy spread predicted by the model is in good agreement with the simulations (figure 7.8). The general temporal development and the dimensions of the energies found in the simulations are also given by the model. The maximum energies however are overestimated compared to the simulations. This likely originates from the assumption of an isothermal expansion in the model. Hence the electrons do not cool down and transfer more energy to the protons. In addition the

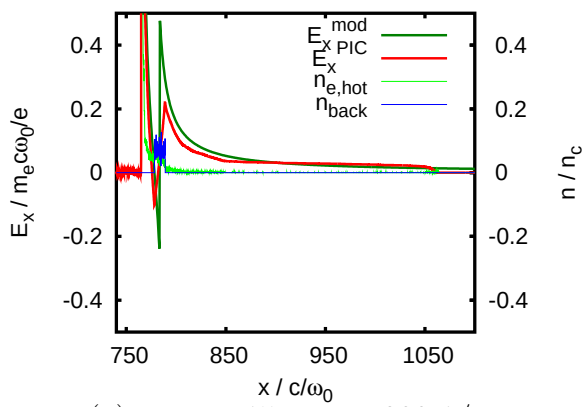

(a) $n_{back} = 15\ n_c, t = 300\ 1/\omega_0$

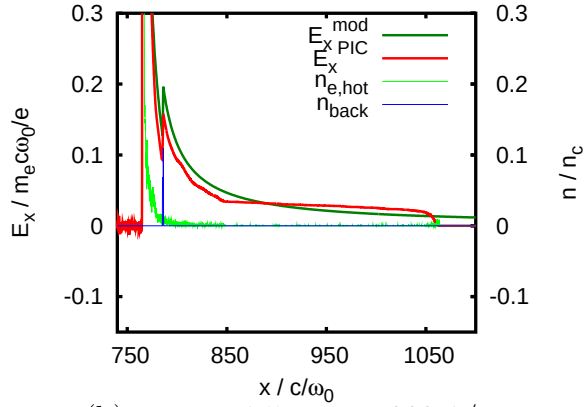

(b) $n_{back} = 1.5\ n_c, t = 300\ 1/\omega_0$

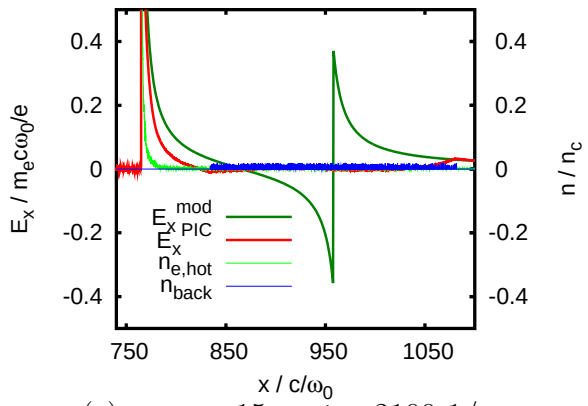

(c) $n_{back} = 15\ n_c, t = 2100\ 1/\omega_0$

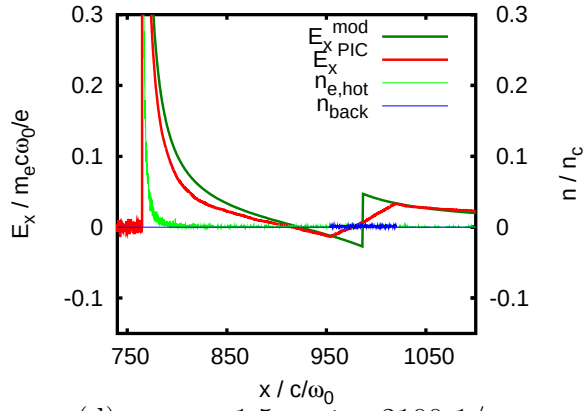

(d) $n_{back} = 1.5\ n_c, t = 2100\ 1/\omega_0$

Figure 7.7: The electric fields of the simulations compared to the one of the model at an early and a late point in time. The left column shows the plots for a high density layer and the right column for a low density case. Outside the proton layer the analytical electric fields match the simulations results pretty well.

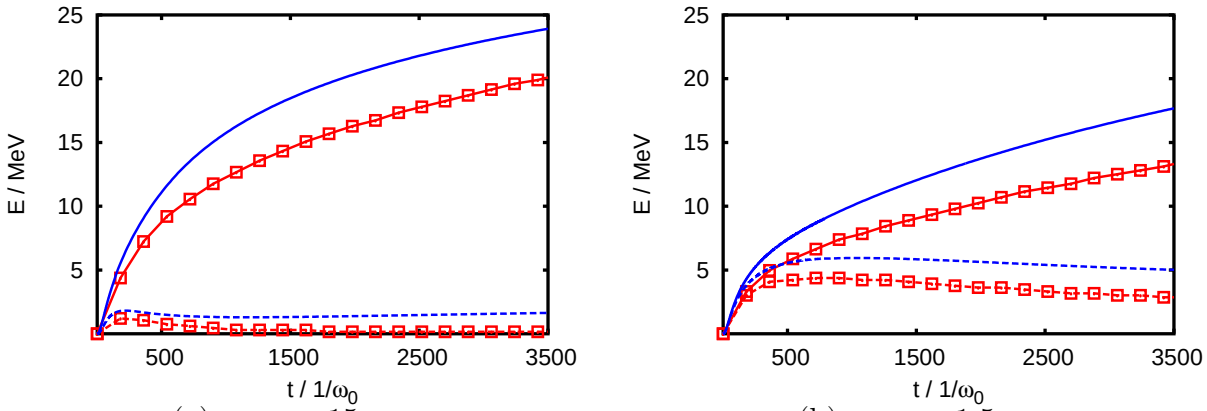

(a) $n_{back} = 15\ n_c$ (b) $n_{back} = 1.5\ n_c$

Figure 7.8: The temporal development of the maximum and minimum energies is in fairly good agreement for the simulations (red) and the model (blue) for proton layers of (a) $n_{back} = 15\ n_c$ and (b) $n_{back} = 1.5\ n_c$ considering the crude approximations employed in the model. However all energies are overestimated. This discrepancy is likely related to the isothermal characteristic of the model. In addition in the high density case (a) the minimum energy predicted by the model is not vanishing but starting to increase again.

model predicts no vanishing of the minimum energy in the high density case. Actually it yields a reacceleration from 1000 $1/\omega_0$ on. This non-physical phenomenon is caused by the expansion of the layer while the model is assuming a point-like proton bunch. If the leftmost proton has departed far enough from the middle of the expanding layer (i.e. the position of bunch in the model) the model predicts a positive electric field at this position (see figure 7.7 (c)) and the particle is reaccelerated.

7.2 Laser-plasma set-ups

In the described simulations the laser-plasma interaction is neglected and the system is initialized with a hot electron population. To verify if the effect of the second expansion is only an intrinsic property of the plasma expansion, simulations for fixed ions including the laser-plasma interaction are performed. In the next section basic studies in one dimension are given whereas in section 7.2.2 some exemplary two dimensional simulations are presented.

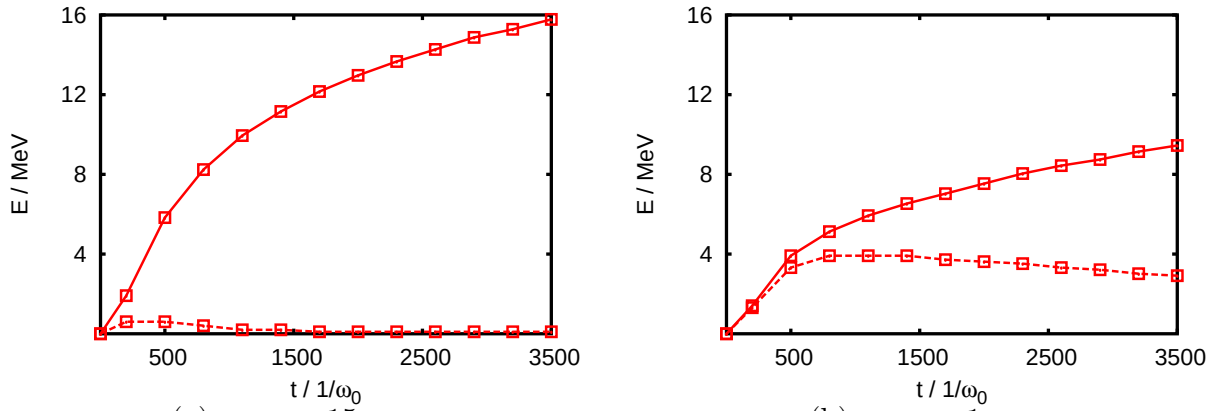

(a) $n_{back} = 15.\ n_c$ (b) $n_{back} = 1.\ n_c$

Figure 7.9: Temporal development (at $t = 0\ 1/\omega_0$ the laser hits the target) of minimum and maximum energy for fixed ions in laser-plasma interaction simulations. As for a pure plasma expansion the second expansion can be reduced by reducing the density of the proton layer.

7.2.1 1D simulations

In principle the target set-up is identical to the plasma expansion simulations (figure 7.1) except for the hot electron population. Initially all electrons are at rest and later on heated by a laser. The laser yields a normalized vector potential of $a_0 = 3.7$ and a pulse length of 190 $1/\omega_0$. Besides the density of the proton layer is reduced from 15. n_c to 1. n_c (instead of 1.5 n_c). The rear layer still has a thickness of $d_{back} = 0.05\ c/\omega_0$.

Minimum and maximum energy

For a high density coating ($n_{back} = 15\ n_c$, figure 7.9 (a)) the simulations show the same properties as in the case of a simple plasma expansion (compare to figure 7.4 (a)). After an initial increase in the minimum energy cut-off it starts to decrease and vanishes in the end. The reduction of the layer density to $n_{back} = 1\ n_c$ leads to a weakening of the second expansion and hence a non-vanishing minimum energy (figure 7.9 (b)). This enhancement is similar to the situation in the plasma expansion simulations where lowering of the layer density also led to a non-vanishing minimum cut-off energy (figure 7.4 (b)).

In addition the dependence of the minimum energy on the mass of the substrate is rediscovered (figure 7.10). The minimum energy is rapidly decreasing with increasing mass of the front layer ions (compare to figure 7.3 (b)). The maximum energy also tends to increase for heavier substrates but is fluctuating especially for substrates with low masses. The fluctuations are based on the complex variations of the absorption

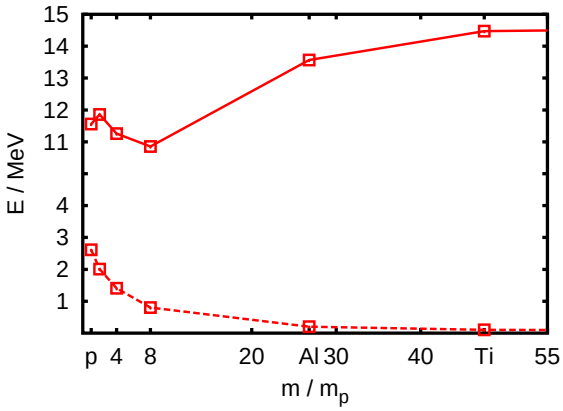

Figure 7.10: The minimum energy (dashed line) of the proton bunch is decreasing rapidly with increasing mass. The maximum energy (solid line) tends to increase with increasing mass but fluctuates for small ion masses.

due to different masses. The absorption is sensitive to the density profile at the target front during the laser-plasma interaction which is of course influenced by the inertia of the ions. The absorption in the end affects the hot electron density and therefore the maximum energy.

7.2.2 2D simulations

Two-dimensional PIC simulations are performed to study the basic process of proton acceleration with double-layers in a more realistic set-up. As the computational time increases significantly for two-dimensional simulations the investigations are restricted to a limited number of set-ups. Like in the one-dimensional simulations the influence of the thickness of the proton layer at the rear side is studied. In addition the lateral extension of the proton dot is varied.

The simulations are performed for a 750 $c/\omega_0 \times 144$ c/ω_0 wide box divided into cells with $\Delta x = \Delta y = 0.16$ c/ω_0. The target is placed at $x = 240$ c/ω_0 and consists of a $n = 10$ n_c, 9.6 c/ω_0 thick layer of fixed ions and a proton layer with thickness d_{back}. The lateral dimension of the layer is L and its density $n_{back} = 1$ n_c. A temperature of 5 keV is assigned to the electron population which equals the proton densities. At the beginning of the simulation 50 particles per cell are initialized. The laser yields the normalized vector potential $a_0 = 3.7$ and Gaussian profiles in time with a FWHM of $\tau_{las} = 190$ $1/\omega_0$ as well as in transversal direction ($l_{y,FWHM} = 40$ c/ω_0). 50000 time steps with $\Delta t = 0.08$ $1/\omega_0$ are performed resulting in a total simulation time of $T = 4000$ $1/\omega_0$.

The dimensions of the proton dot at the rear side are varied. For a thickness of $d_{back} = 0.16$ c/ω_0 the lateral extension is $L = 10, 20$ and 40 c/ω_0. Furthermore for the smallest transversal size, $d_{back} = 10$ c/ω_0 the thickness is changed, $d_{back} = 0.16$, 0.8 and

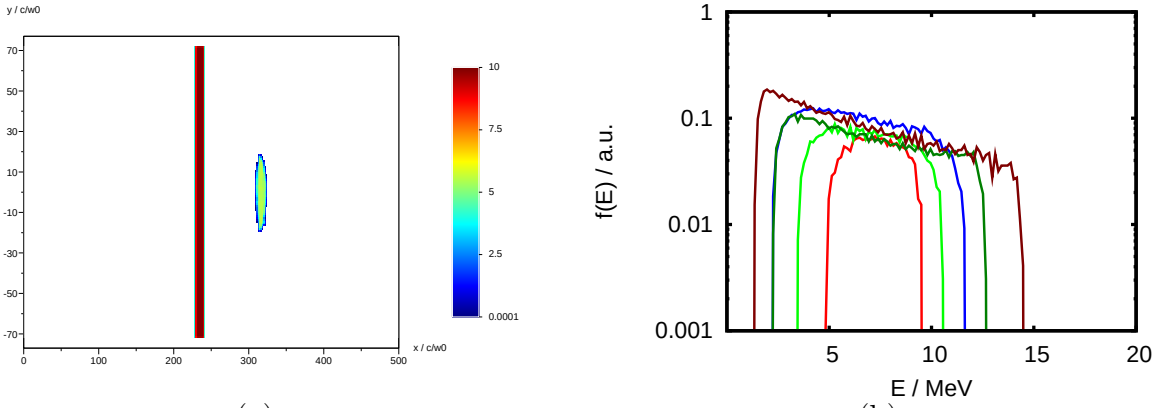

(a) (b)

Figure 7.11: (a) Proton density at 800 $1/\omega_0$ after the laser has hit the target (the color scale denotes the density in n_c). (b) Energy spectra for $d_{back} = 0.16\ c/\omega_0$ and $L = 10\ c/\omega_0$ (red), $L = 20\ c/\omega_0$ (light green), $L = 40\ c/\omega_0$ (blue) as well as for $L = 10\ c/\omega_0$ and $d_{back} = 0.8\ c/\omega_0$ (dark green) and $d_{back} = 1.6\ c/\omega_0$ (dark red).

$1.6\ c/\omega_0$.

As in one dimension the proton dot, which is initially attached to the fixed proton layer, propagates in positive x-direction (figure 7.11 (a)). The energy spectra at 3060 $1/\omega_0$ after the maximum of the laser pulse has reached the target surface are shown in figure 7.11 (b). The mean energy for all set-ups is around 7 MeV. The smallest energy spread is found for $d_{back} = 0.16\ c/\omega_0$ and $L = 10\ c/\omega_0$. For increasing layer thickness the maximum energy increases while the minimum energy is decreasing (table 7.1). However the expansion which is leading to an additional amplification of the energy spread is more moderate compared to the situation in one dimension. E.g. for a much thinner layer with $d_{back} = 0.05\ c/\omega_0$ the relative energy spread yields in one-dimensional simulations already $\Delta E/E_0 = 1.0$ (see figure 7.9).

An increase of the lateral extension of the proton dot also scales up the energy spread. Especially protons situated far away from the center of the dot contribute to the low energy part of the spectrum.

The energy spread found in the two-dimensional simulations is compared to the analytical estimation (equation (3.38))

$$\left(\frac{\Delta E}{E_0}\right)_{3D} = \sqrt{\frac{eQL}{3\epsilon_0 E_0}} \tag{7.2}$$

which is valid in three dimensions. The simulation results are larger by a factor $3-4$ compared to the analytical predictions (table 7.1). This reduction of the energy spread

L / c/ω_0	d_{back} / c/ω_0	E_{min} / MeV	E_{max} / MeV	$\Delta E/E_0$	$(\Delta E/E_0)^{theo}$
10.	0.16	4.7	9.5	0.68	0.19
20.	0.16	3.3	10.6	1.04	0.28
40.	0.16	2.1	11.8	1.39	0.39
10.	0.8	2.1	12.8	1.43	0.42
10.	1.6	1.2	14.5	1.68	0.58

Table 7.1: Minimum, maximum energy as well as the energy spread for various proton dots. Additionally the energy spread calculated by equation (7.2) is given.

is due to the less intense repulsive Coulomb force in three dimensions.

7.3 Treatment planning

In the previous sections the possibility of generating "quasi-monoenergetic" proton spectra was studied. Depending on laser and target parameters the energy spectrum varies. In addition the dimension (1D, 2D or 3D) in which the process is investigated plays a significant role. Here the potential of these proton beams for radiotherapy especially in contrast to conventional intensity modulated γ-radiation therapy is studied.

7.3.1 Towards high energies

At first the characteristic energies have to be scaled to suitable energies. According to the scaling laws of chapter 5 energies of more than 200 MeV can be obtained for intensities of $I \sim 5 \times 10^{21} W/cm^2$ for proper parameters sets, the minimum energy is simply assumed to be $E_{min} = 200$ MeV. Additionally based on the PIC simulation results the energy spectra are assumed to show a constant shape with homogeneously distributed protons with energies between E_{min} and E_{max}.

Furthermore a suitable dose rate is required which corresponds to a minimum current of at least 1 nA. For a todays laser system with a repetition rate of $f = 10$ Hz and assuming that the whole proton dot at the rear side is accelerated, a 1 n_c proton layer of size 2 μm $\times$ 2 μm and thickness 0.16 μm would be sufficient. If the minimum energy is approximately equal to the mean energy the relative energy spread in three dimensions (equation (7.2)) is $\Delta E/E_0 \sim 10\%$, i.e. $\Delta E = 20$ MeV. The order of magnitude of the energy spread is confirmed by two-dimensional PIC simulations by Schwoerer *et al.* [11]. For a 0.1 μm thick PMMA dot with a diameter of 2.5 μm a peak energy of 173 MeV is found at an intensity of $I = 1.2 \times 10^{21} W/cm^2$. The corresponding relative energy width is $\Delta E/E_0 = 1\%$.

Besides this "optimal" proton beam a "worst-case" proton beam is studied. The two-dimensional simulations showed an energy spread which is increased by a factor $3 - 4$

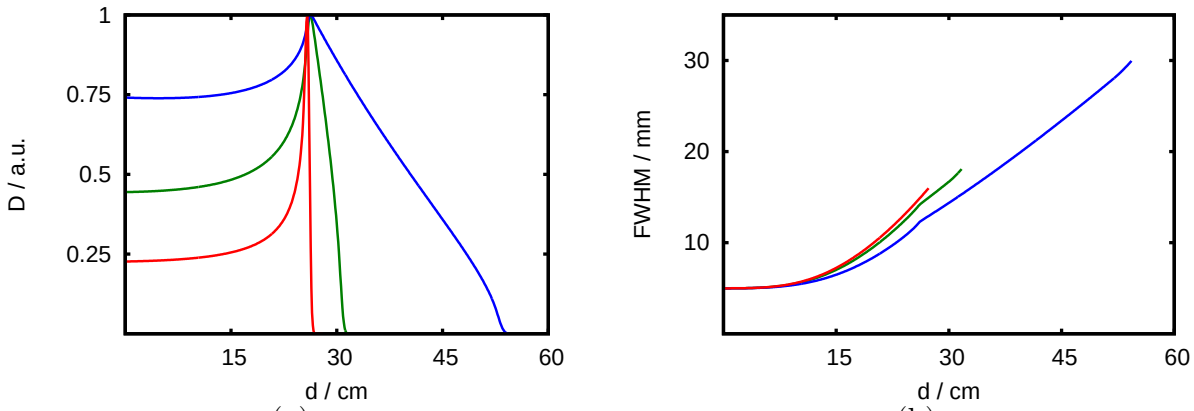

Figure 7.12: Depth dose curves (a) and the full width at half maximum of the lateral spread (b) of proton beams with a constant energy distribution. The minimum energy is set to $E_{min} = 200$ MeV and the energy spread is $\Delta E = 0$ MeV (red), $\Delta E = 10$ MeV (green) and $\Delta E = 100$ MeV (blue) respectively.

compared to the model (section 7.2.2). Hence a "worst-case" relative energy spread of 50% is assumed, i.e. $\Delta E = 100$ MeV.

7.3.2 Dosimetric properties

To integrate laser-accelerated proton beams into a treatment planning system the corresponding depth dose curve (DDC) and the lateral spread in depth in water are calculated.

Depth dose curve

The DDC is calculated by an analytical proton pencil beam approach [70]. The calculations are slightly customized as constant energy spectra instead of Gaussian distributions are considered. The spectra are sampled with a constant step size of 0.1 MeV and afterwards the resulting DDCs of monoenergetic pencil beams are added and normalized.

The maximum of the DDCs of the proton beams with relative energy spreads $\Delta E/E_0 = 10\%$ and $\Delta E/E_0 = 50\%$ is in both cases close to the position of the maximum for a monoenergetic beam with the same energy as the minimum energy $E_{min} = 200$ MeV (figure 7.12 (a)). In contrast to the steep dose fall-off behind the maximum in the case of the monoenergetic beam, the dose vanishes not until 5 cm ($\Delta E/E_0 = 10\%$) respectively more than 25 cm ($\Delta E/E_0 = 50\%$) behind the peak. In addition the entrance dose increases with increasing energy spread.

Lateral spread

To calculate the lateral spread in depth for the dose deposition in a water phantom the quadratic parameterization found by Hong *et al.* [71] for monoenergetic proton beams is used,

$$\sigma_w(z, R_0) = a_0 R_0 \left(a_1 \frac{z}{R_0} + a_2 \frac{z^2}{R_0^2} \right), \tag{7.3}$$

with standard deviation σ_w of a Gaussian distribution, depth in water z (in cm), initial range of the monoenergetic proton beam R_0 (in cm) and fit parameters a_i. The latter are given by $a_0 = 0.02275$, $a_1 = 0.18$ and $a_2 = 0.82$. To approximate the standard deviation of a proton beam with an energy spread, $\sigma_w(z, E_{min}, E_{max})$ at each depth z is computed as the weighted composition of the individual contributions of the remaining sampled energies. The weighting factors are given by the normalized dose deposition of the sampled monoenergetic beams at the relevant depth[2],

$$\sigma_w(z, E_0, E_n) = \sum_{i=0}^{i=n} w_i(z) \sigma_w(z, E_i), \tag{7.4}$$

with $w_i = D(z, E_i) / \sum D(z, E_k)$, $E_0 = E_{min}$ and $E_n = E_{max}$. $D(z, E_i)$ represents the dose delivered at depth z by a monoenergetic proton beam with energy E_i.

The full width at half maximum (figure 7.12 (b)) of the lateral spread is increasing with depth. Compared to the monoenergetic proton beam it is slightly reduced.

7.3.3 Optimization and dose calculation

Before the comparison of treatment plans for laser-accelerated proton beams and conventional photon IMRT is performed some details regarding optimization and dose calculation are given.

D_{ij}-matrix approach

The optimization is based on the D_{ij}-matrix approach [72]. The starting point for treatment planning is a three-dimensional data set from a computer tomograph (CT). It is divided into so-called voxels which are small volume elements with a typical dimension of $2 \times 2 \times 3 mm^3$. These are assigned to volumes of interest like the tumor, i.e. the target, organs at risk or normal tissue. Then the beam directions are chosen. Each beam is divided into small elements. These so-called bixels are defined in the isocenter plane and carry an individual weight w_j which has to be optimized to obtain the optimal dose

[2] Be aware, that this dependence is only a phenomenological approximation, Nevertheless for energy spectra in the range of $E_{min} \simeq 110$ MeV the results obtained by equation (7.4) are very well reproduced by adequate Monte Carlo simulations.

distribution. The matrix element D_{ij} is the dose which is delivered by bixel j for unit weight to voxel i, i.e. the dose at voxel i is

$$d_i = \sum_{j=1}^{N_j} D_{ij} w_j \tag{7.5}$$

where N_j is the number of bixels.

Dose calculation

To calculate the D_{ij}-matrix at first the radiological depth η_i of the voxel i is calculated, $\eta_i = \sum_r \rho_r \Delta x_r$. This calculation requires the relative electron densities ρ_r (compared to water) of a voxel which is assigned to the Hounsfield units of the CT cube. Furthermore the corresponding length Δx_r of the ray inside the voxel is needed. The dose at this depth and at the corresponding lateral displacement of voxel i with regard to the central axis of the beam is given by the pre-calculated dose distribution.

Optimization

The optimization of the bixel weights w_j is done by minimizing the objective function F. This is composed by the objective functions for the target (F_t) and the organs at risk (F_r),

$$F = \sum_{t=1}^{N^{TARGET}} F_t + \sum_{r}^{N^{OAR}} F_r \tag{7.6}$$

with

$$F_t = \frac{1}{N_t} \sum_{i=1}^{N_t} s_u^t \left[d_t^{min} - d_i\right]_+^2 + s_o^t \left[d_i - d_t^{max}\right]_+^2 , \tag{7.7}$$

$$F_r = \frac{1}{N_r} \sum_{i=1}^{N_r} s_o^r \left[d_i - d_r^{max}\right]_+^2 . \tag{7.8}$$

$$\tag{7.9}$$

$[x]_+ = x\Theta(x)$ is the positive operator, $N_{t/r}$ are the number of voxels in the target/organ at risk. A minimum and maximum dose ($d_t^{min/max}$) is specified for each target as well as a maximum dose for all organs at risk. The corresponding penalties for over- and under-dosage are $s_{u/o}^t$ for the target and s_o^r for the organs at risk respectively. An iterative gradient algorithm is optimizing the objective function to obtain the optimal dose distribution.

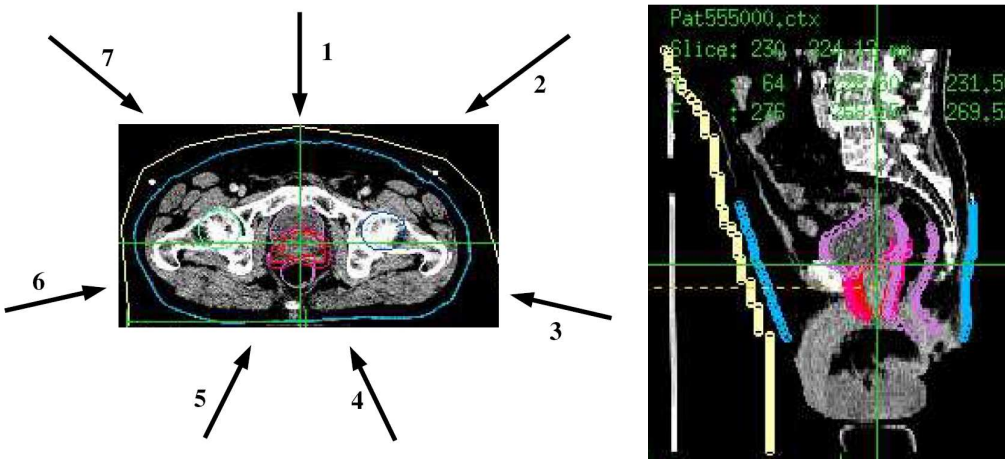

(a) (b)

Figure 7.13: The comparison between laser-accelerated proton and photon treatment plans is based on a clinical approved seven-field 6MV photon plan (a). Part (b) shows a sagittal slice.

7.3.4 Comparison of laser-accelerated proton and photon treatment plans

The comparison is based on a clinical approved seven-field prostate treatment plan (figure 7.13) for 6 MV photons. The optimization parameters, such as beam directions and penalty factors, are retained for the proton treatment plans. The prescribed dose to the gross tumor volume (GTV) is 76 Gy. The spatial resolution of the photon bixels is 5×5 mm^2 while the distance between two proton beamlets is 3 mm. As scanning mode distal edge tracking is chosen. Three proton beams are compared to the photon plan, each with a minimum energy of 200 MeV. Two "laser-accelerated" beams with $\Delta = 20$ MeV and $\Delta E = 100$ MeV respectively and one conventional monoenergetic beam are chosen.

To compare the treatment plans the respective target coverage and dose sparing of organs at risk are opposed. For that purpose minimum, maximum and mean doses (normalized to the mean dose to the GTV) as well as dose-volume histograms (DVHs) are consulted.

The target coverage for all proton plans is the same or even slightly improved (figure 7.14 (a)), except for the minimum dose to the planning target volume (PTV) of the monoenergetic proton beam.

In addition the dose sparing of sensitive structures is improved by all proton beams (see figure 7.14 (b) and table 7.2). The mean dose to the organs at risk and the remaining normal tissue is reduced by all proton plans.

For the monoenergetic proton beam the dose to the rectum is reduced to 29.1%,

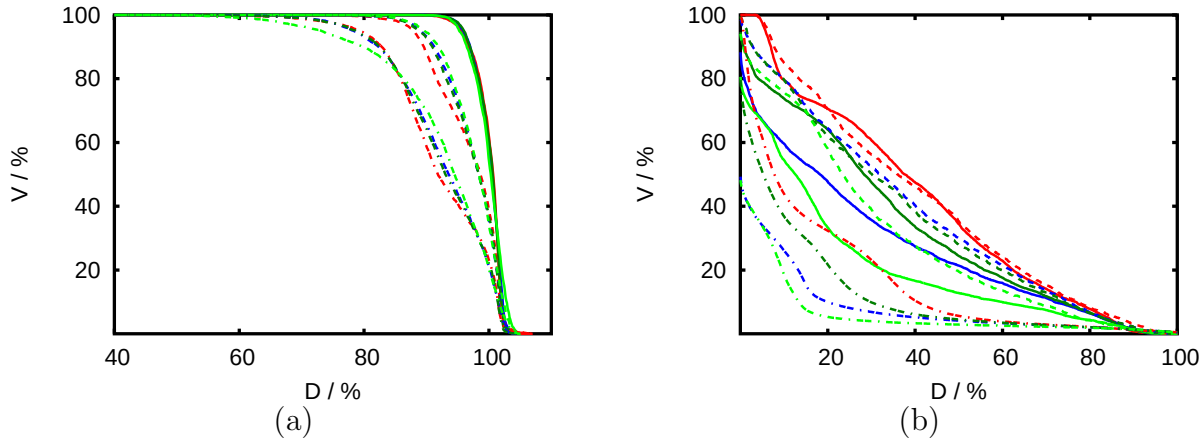

Figure 7.14: (a) DVHs of the GTV (solid line), CTV (dashed line) and PTV (dashed-dotted line). Photons are represented by red, protons by light green ($\Delta E = 0$ MeV), blue ($\Delta E = 20$ MeV) and dark green ($\Delta E = 100$ MeV) respectively. (b) The corresponding DVHs of bladder (solid line), rectum (dashed line) and normal tissue (dash-dotted line).

compared to 39.6% for photons. For the two proton beams with non-monoenergetic energy spectra the corresponding dose is 35.7% ($\Delta E = 20$ MeV) and 34.6% ($\Delta E = 100$ MeV) respectively.

For the normal tissue and the bladder the mean dose is simply decreasing with decreasing energy spread. E.g. the dose to the bladder is reduced from 39.1% (photons) to 32.4% ($\Delta E = 100$ MeV), 26.4% ($\Delta E = 20$ MeV) and 20% (monoenergetic). The

However for the left and right femur the proton beam with the small energy spread, $\Delta E = 20$ MeV, yields the lowest mean dose with 2% and 3.8% versus 11.8% and 17.2% for photons respectively.

7.4 Conclusions and outlook

The principle of proton acceleration by double-layer targets consisting of a substrate and a thin proton layer has been studied by means of PIC simulations. The underlying process of generating "quasi-monoenergetic" energy spectra is demonstrated by simulating simple plasma expansions. The energy spread is strongly affected by the target constituents. For increasing thickness and density of the proton layer and increasing mass of the substrate the energy spread augments, leading to some extent to vanishing minimum energies. This is based on a Coulomb expansion of the proton layer which has separated from the substrate. The negative charge of the hot electron cloud does not balance the positive charge of the layer and thus repelling forces arise. The simulation

		$\Delta E = 0$ MeV	$\Delta E = 20$ MeV	$\Delta E = 100$ MeV	6MV
Rectum	D_{min}	0.0	0.0	0.0	3.2
	D_{mean}	29.1	35.7	34.6	39.6
	D_{max}	103.7	99.5	100.1	100.1
Bladder	D_{min}	0.0	0.0	0.0	3.4
	D_{mean}	20.0	26.4	32.4	39.1
	D_{max}	98.9	97.9	97.2	98.6
Femur (right)	D_{min}	0.0	0.0	0.2	2.9
	D_{mean}	4.6	3.8	11.2	17.2
	D_{max}	12.2	15.0	27.3	33.7
Femur (left)	D_{min}	0.0	0.0	0.0	1.9
	D_{mean}	3.8	2.0	8.3	11.8
	D_{max}	13.0	17.4	30.6	41.5
Normal tissue	D_{min}	0.0	0.0	0.0	0.0
	D_{mean}	6.3	8.2	12.2	16.7
	D_{max}	105.0	104.3	104.4	107.0

Table 7.2: Maximum, minimum and mean dose (normalized to the mean dose to the GTV) of organs at risk and normal tissue for treatment plans of a monoenergetic proton beam, proton beams with an energy spread and 6 MV photons.

results are more or less in agreement with the predictions of an analytical approach [56]. Based on this model and additional two-dimensional simulations energy spectra of proton beams with minimum energies suitable for radiotherapy are obtained. It turns out that the expansion is much more moderate in three dimensions leading to energy spreads of about 10%. Subsequently a comparison of treatment plans for protons originating from double-layer targets and conventional photon beams is carried out. Due to the uncertainty of the exact energy width a "best" ($\Delta E/E_0 = 10\%$) and a "worst-case" ($\Delta E/E_0 = 50\%$) as well as a monoenergetic proton beam are chosen. The results for a clinical approved prostate plan show that compared to the photon plan the plan quality improves by all proton plans. The target coverage is almost the same or even slightly improved while the dose sparing of sensitive structures is superior in the case of the proton plans. In general with decreasing energy width the proton plan quality improves.

Though the comparison is based on limited simulations - in the sense of low dimension and "unrealistic" target set-ups - as well as on rough estimations the results are promising. As laser intensities increase the proton energy will become higher and energies will be reached which are suitable for radiotherapy. Even if the resulting energy spectra do not show a pure monoenergetic characteristic an improvement of treatment plan quality compared to conventional photon beams is present. However to achieve this aim further technological progress with regard to laser and micro-structured targets is necessary.

8 Conclusions and outlook

In this part of the work the potential of an application of laser-accelerated protons in radiotherapy was investigated. Studies with regard to the maximum energy as well as concerning the control of the energy spectrum were performed.

With respect to the maximum energy an analytical model describing the scaling of the maximum proton energy [52] was compared to one- and two-dimensional PIC simulations as well as to experimental data from literature. For the one-dimensional simulations a good agreement of the model with the simulation results was found by extending the model by a characteristic acceleration time coefficient R. This is taking into account that the acceleration process in laser-plasma interactions is non-isothermal in contrast to the model which assumes an infinitely large reservoir of hot electrons. It turns out that the characteristic acceleration time coefficient depends on the pulse duration, $R = (111. \pm 21.) \times \tau_{las}^{(-0.86 \pm 0.035)}$. With this assumption the model agrees with the simulation results over a wide range of parameters. However in a few cases deviations from the model are found (e.g. for thick targets).

Additionally, a series of two-dimensional simulations was performed. Again the characteristic acceleration time coefficient depends on the laser pulse duration in a very similar way as for the one-dimensional simulations, i.e. $R = (113. \pm 9.1) \times \tau_{las}^{(-0.93 \pm 0.019)}$.

Finally the model was also compared to experimental data from literature was performed. In general one could state that for experiments with a high contrast of pre-pulse and main laser pulse the model agrees well with the experimental data and therfore yields reliable results. However for a low contrast the deviations between experimental results and the predictions of the theoretical approach become quite pronounced.

But all the investigations demonstrate that even with the crude approximations of the model an almost reliable scaling of the maximum energy can be predicted. Based on these findings an estimation of the intensity which results in clinically usable proton energies of more than 200 MeV is made. These energies might be obtained by lasers with intensities of a few times $10^{21} W/cm^2$ which will be available with future laser systems.

The second investigation concerned the achievable control of the energy spectrum respectively the influence of a poly-energetic spectrum. Typically, laser accelerated protons yield an exponentially decreasing energy spectrum which is inadequate for radiotherapy. At first set-ups with two lasers and two targets were performed. The spectrum of protons originating from the first foil was manipulated by large electric fields at the second foil. These fields were generated by the interaction of a second laser with this second target. However, due to an additional expansion the early creation of a promising "quasi-monoenergetic" high energy part vanishes again.

The studies with regard to double layer targets [10] were much more encouraging. The acceleration of a thin proton layer initially attached to a heavy ion substrate leads to a "quasi-monoenergetic" spectrum. The basic mechanism was investigated in the case of a simple plasma expansion and the simulation results show a good agreement with an analytical model [56]. Besides the thickness of the proton layer a Coulomb expansion of the propagating layer was basically responsible for the magnitude of the energy spectrum and fairly well described by the theoretical approach. Based on these results and additional two-dimensional PIC simulations the energy spread for clinically relevant energies was estimated. The dimensions of the attached proton layer were always chosen such that the number of protons is sufficient to provide a reasonable current of at least 1 nA. These spectra were used as a basis for treatment planning of a prostate case. Even in the "worst case" scenario (i.e. the largest energy spread) the laser-accelerated protons led to an improvement of treatment plan quality compared to a conventional photon plan. At a similar target coverage the dose sparing of critical structures was improved by the protons. In general the plan quality naturally increases with decreasing energy spread.

These results are encouraging that one might be able to exploit the advantages of laser-plasma accelerators for proton radiotherapy. However, in the long run towards clinical application various obstacles still have to be overcome. First, the experimental verification of the scaling laws has to be established. Second, the probably most promising set-up of double-layered targets still has to be developed for clinically required higher energies of $200 - 230$ MeV.

Furthermore, various general "technical" problems have to be solved. For any clinical application a high reliability of the acceleration process has to be guaranteed. The current systems, which are of course in an experimental state and therefore do not have the ambition of being perfectly reliable, lack e.g. the reproducibility of generating the energy spectra. For clinical use however the energy as well as the energy spread have to be controlled within a few percent. Another challenge will be the dosimetry of the proton bunches. As the temporal extension of the bunches is of the order of the laser pulse duration (i.e. sub-picosecond) new ways of measuring dose have to be developed. In addition the biological effects of this extremely short time dose application have to be studied.

But nevertheless the above noted expectations regarding the maximum energy and the control of the energy spread certainly justify further efforts to study the potential of laser-accelerated protons in radiotherapy.

Part II

ELECTRONS

9 Introduction

Very high energy electrons (VHEE) in the range of $150 - 250$ MeV show advantageous dosimetric properties compared to photon beams [13, 14, 15, 17]. For instance DesRosiers *et al.* [13] studied the lateral spread and the penetration of these electron beams by means of Monte Carlo simulations. They showed that the penumbra of a single VHEE beam is somewhat less wide than the penumbra of single clinical photon beams for depths below 5 cm and somewhat wider for depths above 10 cm. In contrast to low energy electrons ($5 - 50$ MeV), which are currently used in radiotherapy, VHEE are not restricted to non-deep-seated tumors because the practical range exceeds 40 cm. Additionally the effects caused by nuclear reactions are analyzed. The increased dose due to neutron production and induced radioactivity result in an increased relative biological effectiveness (RBE) factor of < 1.03. Another aspect is the opportunity of electromagnetic scanning of the electron beams which is provided by the limited scattering in air.

Yeboah *et al.* studied intensity modulated very high energy electron therapy (VHEET). At first [14] they evaluated the potential of these electron beams for dose conformation and identified those variables that influence optimized dose distributions for this modality for a prostate cancer phantom geometry. They found that energies above 100 MeV are required to achieve acceptable dose conformation in the target and dose sparing of sensitive structures. 250 MeV electrons showed the best plan quality with respect to these quantities. A large number of fields in the range of 9-21 beams is required to provide acceptable plans. For rotation therapy the modulation of beam energy had no beneficial consequences on the optimized dose distributions. However when using a small number (≤ 9) of beams minor improvements in VHEET plans may be achieved if energy modulation is implemented. Based on these results they performed a comparison of intensity-modulated proton therapy (IMPT), intensity-modulated very high energy electron therapy with 250 MeV electrons and intensity-modulated x-ray therapy (IMXT) [15]. For a two-dimensional model for the geometry of a prostate case the best plan quality was achieved by IMPT. The comparison of VHEET and IMXT shows that they both provide almost the same target coverage. But the mean dose to bladder and rectum was reduced by up to 10% of the prescribed target dose when applying VHEET. Thus the greatest dose escalation would be possible with IMPT, then VHEET, and then IMXT.

A major objection to VHEET is the lack of clinically available, compact and inexpensive accelerators. This could be overcome by the use of compact laser-plasma accelerators [73, 74, 75, 3] which provide "quasi-monoenergetic" electron energy spectra with peak

energies between 50 MeV and 250 MeV.

The potential of laser-accelerated electron beams is analyzed in the next chapters. At first the underlying physics is described in detail and recent experimental results are presented (chapter 10). The dosimetric properties of these electron beams are studied by means of Monte Carlo simulations (chapter 11) to find appropriate beam characteristics for most conformal treatment plans. In a second step (chapter 12) the obtained dose distributions are used as a basis for treatment planning. A clinical prostate plan for 6 MV photons is compared to plans for various electron beam set-ups.

10 Underlying physics and experimental results

The experimental set-up of laser-plasma based electron accelerators is almost the same as the one for accelerating protons. A high intensity laser with $I \geq 10^{18} W/cm^2$ is focused onto a target (see figure 3.1 in chapter 3). In contrast to proton acceleration the solid target is replaced by a helium gas jet with a diameter of ~ 2 mm. The density of the gas is below the critical density and yields e.g. $n_e = 7.5 \times 10^{18}$ 1/cm^3 [3].

The front of the laser pulse ionizes the helium atoms such that the main pulse is interacting with a plasma. The ponderomotive force, which is proportional to the intensity gradient, expels electrons from the high intensity regions, creating a plasma wave [76] (figure 10.1). The corresponding electric field exceeds strengths of 1 TV/m [77]. As they travel with a velocity close to the speed of light, these fields are capable of accelerating background electrons to relativistic energies. These are injected into the wake-field and accelerated in "quasi-monoenergetic" bunches [73, 74, 75].

However the injection of electrons into the accelerating "bubble" is a highly non-linear phenomenon. Hence from shot to shot large fluctuations regarding peak energy and energy spread are observed. Recently [3] this problem was overcome by controlling the injection with a second laser pulse. This counter-propagating "injection" pulse with the same wave length and polarization but a more moderate intensity, $I \sim 4 \times 10^{17} W/cm^2$, collides with the "pump" laser ($I \sim 3.4 \times 10^{18} W/cm^2$). The generated standing wave pre-accelerates electrons which in the end yield a quasi-monoenergetic spectrum (figure 10.2 (a)). The peak energy is e.g. $E_{peak} = 170$ MeV and the energy spread is 10%. In addition the electron bunch is strongly collimated with a divergence angle of 6 mrad at full width half maximum (FWHM).

This set-up with two laser pulses propagating in opposite directions allows to control the point of electron injection. This results in an increased stability and reproducibility of the electron beams. Furthermore it provides the potential to tune the peak energy by varying the delay between the two pulses. If the collision takes place at the beginning of the gas jet, i.e. close to the surface where the "pump" laser enters the gas jet, the electrons are accelerated throughout the whole plasma leading to large peak energies. However when the delay is chosen such that the pulses collide at the end of the gas jet, only a short acceleration distance remains and the peak energy is much lower. The electron energy can be tuned between 15 MeV and 250 MeV. As the energy spread is almost constant, $\Delta E = 10 - 20$ MeV, the relative energy spread is decreasing with increasing electron energy (figure 10.2 (b)).

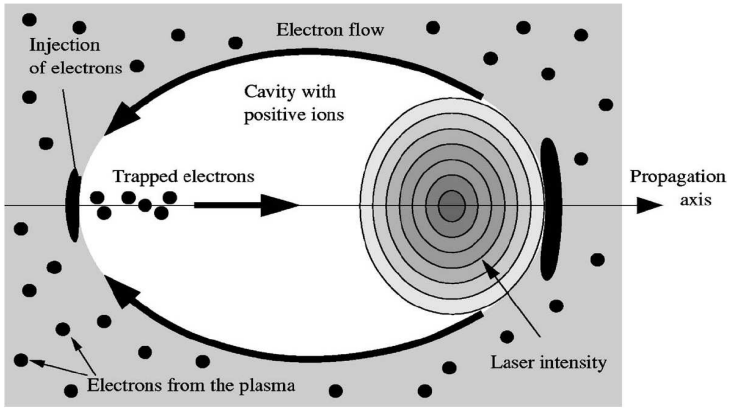

Figure 10.1: Schematic view of electron acceleration
[1]The short laser pulse expels electrons out of high intensity regions leaving a positively charged cavity behind. Electrons which are trapped in this "bubble" are accelerated to relativistic energies.

The charge of the electron bunch is $Q = 15 - 30$ pC in the energy range between 100 MeV and 200 MeV and drops below 10 pC for energies > 200 MeV. Moreover by turning the angle between the polarization of the two counter-propagating pulses the charge can be tuned. For crossed polarizations no injection occurs and the peak in the energy spectrum vanishes.

[1]By the courtesy of the Groupe Sources de Particules par Laser, Laboratoire d'Optique Appliqée, CNRS, ENSTA, Palaiseau, France

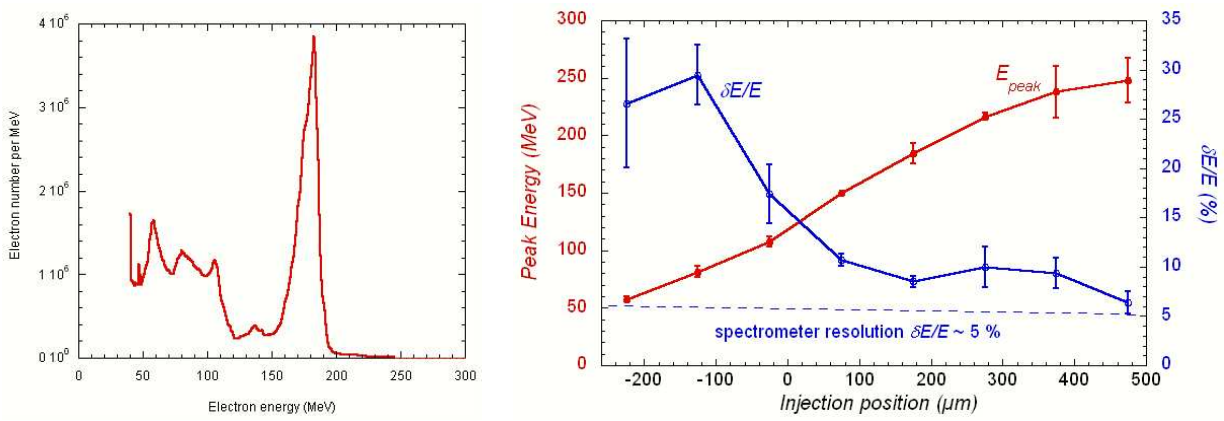

(a)[1] (b)[1]

Figure 10.2: (a) Typical "quasi-monoenergetic" energy spectrum of laser accelerated electrons. The peak energy is 170 MeV and the energy spread 10%. (b) Dependence of electron peak energy (red) and energy spread (blue) on the injection position. $z_{inj} = 0$ μm corresponds to injection in the middle of the gas jet whereas $z_{inj} = 500$ μm denotes a collision of the two laser pulses close to the entrance of the gas jet, i.e. the surface where the "pump" laser is entering.

11 Dosimetric properties

11.1 Monte Carlo simulations

To study the dosimetric properties of laser-accelerated electron beams Monte Carlo simulations are performed. In general the term "Monte Carlo" describes a method which uses stochastic techniques to study the behavior of a physical system. For instance instead of solving complex transport equations one follows the trajectories of single particles and computes the energy deposited in a material. The simulation of a large number of particle trajectories results in a distribution of a physical quantity, here the dose distribution. The physical processes and interactions a single particle experiences on a track are simulated by sampling the corresponding probability distributions.

To give a simple example bremsstrahlung is considered. The differential cross section $d\sigma(Z, E, k)/dk$ characterizes the probability for the production of a photon of energy k by an electron with energy E in the field of an atom of charge Z. When a particle undergoes the process of bremsstrahlung on its trajectory the new electron momentum k'_{el} and the wave vector k of the created photon are sampled from the corresponding probability distribution.

To analyze the dose distribution of laser-accelerated electrons the Monte Carlo tool GEANT4 [78] is used. To briefly introduce the basic terms of GEANT4 the rough course of a simulation is sketched. The simulation (or a *run*) is the collection of a number of *events*. One single event is starting with the generation of a *primary particle* which is followed along its trajectory. The trajectory of the particles is performed *step* by *step*. Along or past a step *physical processes* are included. *Readout geometries* are used to observe physical quantities, for example the energy deposited in a material.

To study the dosimetric properties of laser-accelerated electrons the initial energy of the primary particles is sampled by the energy distribution. The low energy part is assumed to be removed, e.g. by a compact magnetic system (see figure 11.4). The high energy part is characterized by a Gaussian distribution with peak energy E_{peak} and FWHM ΔE. The source is presumed to be point like and the angular distribution of the initial momentum is as well specified by a Gaussian distribution. At FWHM the divergence angle is $\alpha = 6$ mrad. It is assumed that all energies yield the same divergence angle.

To analyze only the effects of several experimental set-ups on the dosimetric properties, the beam is assumed to be propagating in vacuum before entering the water phantom for most of the simulations. Thus scattering in air is neglected. At the end of section

11.4 an exemplary simulation is given for which scattering in air is included.

Each simulation is performed with at least 5×10^6 particles which is only a fraction of the real number of particles but sufficient to perform adequate statistics in reasonable computational time. The electron beam is directed onto a water phantom of $40 \times 40 \times 80$ cm^3.

The integrated depth dose curve (DDC), $DDC(z) = \iint D(x, y, z)dxdy$, with dose $D(x, y, z)$ at lateral distances x, y from the central axis and at depth z, and the FWHM of lateral dose profiles are computed. To determine the FWHM the energy deposited in a slab with a transversal side length of 15 cm is measured. The resolution of this slab is 1 mm in lateral and 3 mm in longitudinal direction. The integration of the energy deposited in lateral slices of the whole phantom with a distance of 3 mm results in the depth dose curve. The maximum step length in the simulations is set to 0.1 mm. The cut value, which determines the threshold range for which no secondary particles will be generated, is also set to 0.1 mm.

At first an exemplary dose distribution is presented (section 11.2). The main dosimetric characteristics are presented on the basis of longitudinal and transversal profiles, the dose distribution in the central plane as well as on the depth dose curve. In addition the maximum dose deposited by a single electron bunch is calculated.

In section 11.3 dosimetric properties for different peak energies are compared. Furthermore the characteristics of experimentally obtained energy spectra are compared to electron beams with a sharp energy.

Additionally in section 11.4 the influence of the source to surface distance as well as a refocusing set-up are studied.

11.2 Exemplary dose distribution

At first an exemplary dose distribution is presented to show the major dosimetric characteristics of laser-accelerated high energy electron beams. The electron peak energy is $E_{peak} = 185$ MeV, the energy spread is $\Delta E/E_{peak} = 8.0\%$ at FWHM and the distance to the water phantom is set to $d = 100$ cm.

The dose distribution in the central plane (figure 11.1 (a)) shows a forward peaked pattern in depth with a slight broadening due to the electron scattering. The isodoses remain almost parallel to the central axis and broaden only slightly for large depths due to to multiple Coulomb scattering. E.g. the 50% isodose extends to a depth of 10.4 cm and the 10% isodose to a depth of 21.0 cm at a maximum lateral spread of 1.5 cm.

The integrated depth dose curve (figure 11.1 (b)) shows a relatively flat characteristic with a broad maximum at the large depth of 23.1 cm. The entrance dose is $\sim 70\%$ and the dose fall-off behind the maximum is almost symmetric to the dose increase in front of it such that the exit dose at 40 cm is around 80%.

The central axis dose profile (figure 11.2 (b)) shows an exponential decrease. 10% of the entrance dose are reached at a depth of ~ 22.0 cm. The lateral profiles fit accurately

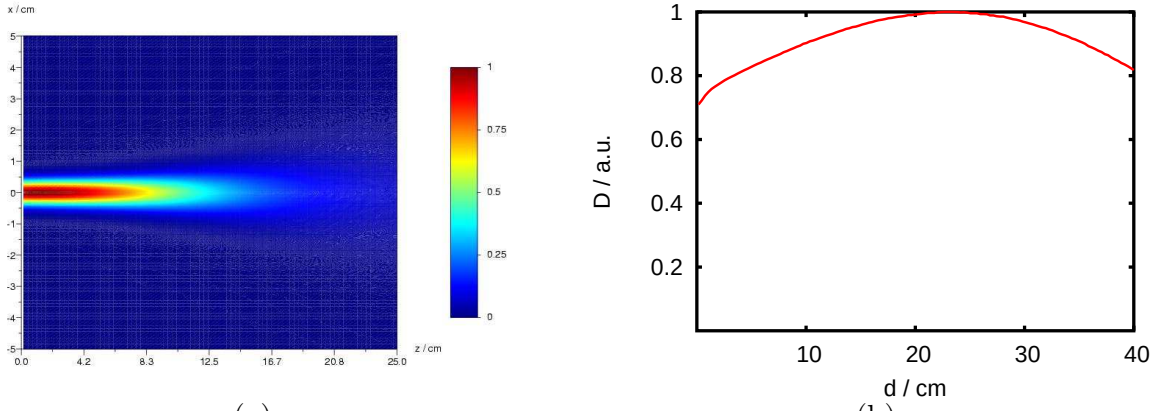

(a) (b)

Figure 11.1: (a) The dose distribution in the central plane for 185 MeV electrons at a distance of 100 cm to the phantom surface. The color scale is indicating the dose in arbitrary units. (b) The depth dose curve for the same electron beam.

to Gaussian distributions (figure 11.2 (a)). At a depth of 5 cm the FWHM of the lateral distribution is 6.8 mm, increasing to 13.3 mm at 15 cm and 25.6 mm and a depth of 25 cm.

The maximum dose which is located close to the phantom surface on the central axis is 4.4 Gy/nC.

11.3 Variation of electron peak energy/energy spread

At first simulations for three different peak energies, $E_{peak} = 150, 185, 250$ MeV, are performed. On the basis of the experimental results (figure 10.2, [3]) the energy spread is chosen, $\Delta E/E_{peak} = 11.5, 8.0, 6.5\%$ at FWHM. The distance to the phantom surface is kept constant at $d = 100$ cm. The depth dose curves (figure 11.3 (a)) for the three electron beams show the relatively flat characteristic with a broad maximum. The depth of the maximum increases with peak energy. For $E_{peak} = 150$ MeV it is located at $\sim$ 19 cm, for $E_{peak} = 185$ MeV at ~ 23 cm and it increases to ~ 29 cm for $E_{peak} = 250$ MeV. The relative entrance dose however decreases with increasing peak energy. For the three energies it decreases from 75% down to 65%. The dose fall-off behind the maximum is also slightly changing with electron peak energy. E.g. 15 cm behind the maximum (i.e. at total depth $\sim 35 - 45$ cm) the dose decreases to approximately 88% (250 MeV), 85% (185 MeV) and 83% (150 MeV). This of course means that the exit dose decreases with decreasing energy.

The lateral spread of the dose distribution is characterized by the FWHM. This is

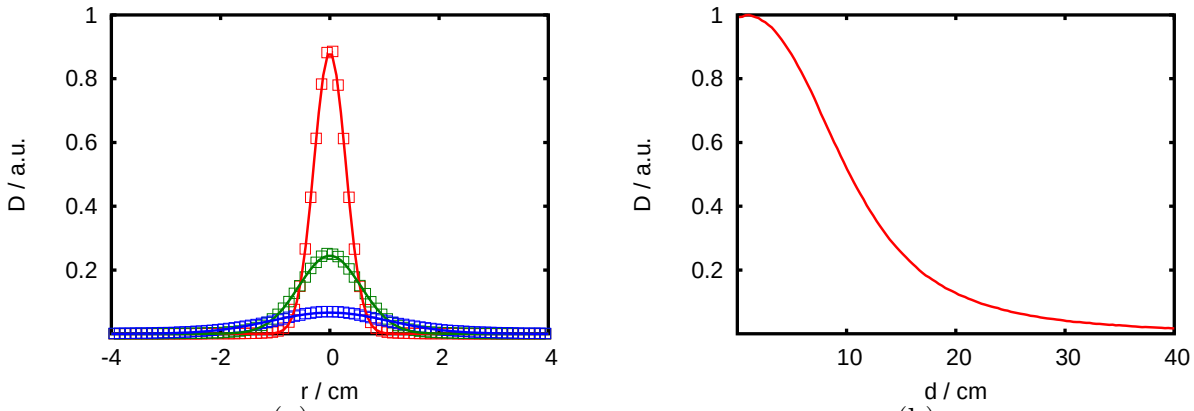

Figure 11.2: (a) Lateral profiles for 185 MeV electrons with a SSD of 100 cm. Gaussian distributions fit accurately to the measured profiles for depths of 5. cm (red), 15. cm (green) and 25. cm (blue). (b) The corresponding longitudinal profile on the central axis.

determined by fitting the lateral profiles to Gaussian distributions (cf. figure 11.2 (a)). At the phantom surface the FWHM yields the same value of 6 mm for all energies. Inside the phantom it increases with depth (figure 11.3 (b)). For larger energies the increase is less intense due to less scattering of the electrons. At 20 cm the FWHM has increased to 22.5 mm, 18.9 mm and 15.1 mm for peak energies of 150 MeV, 185 MeV and 250 MeV respectively. However the FWHM at the maximum of the depth dose curve is increasing with increasing energy, from $\sim$ 21 mm for 150 MeV to $\sim$ 22 mm for 185 MeV and $\sim$ 24 mm for 250 MeV.

The comparison of the dosimetric characteristics for experimentally obtained electron beams with monoenergetic beams of the same energy shows no difference neither for the depth dose curve nor for the FWHM (figure 11.3). Regarding the depth dose curve this can be substantiated by the fact that the DDC shows a broad maximum and e.g. the depth of the maxima for 140 and 160 MeV electrons differ only by $\sim$ 1. cm. In addition the scattering is only slightly affected in this energy range. Hence a further reduction of the energy spread is not required to improve the dosimetric characteristics of the electron beams.

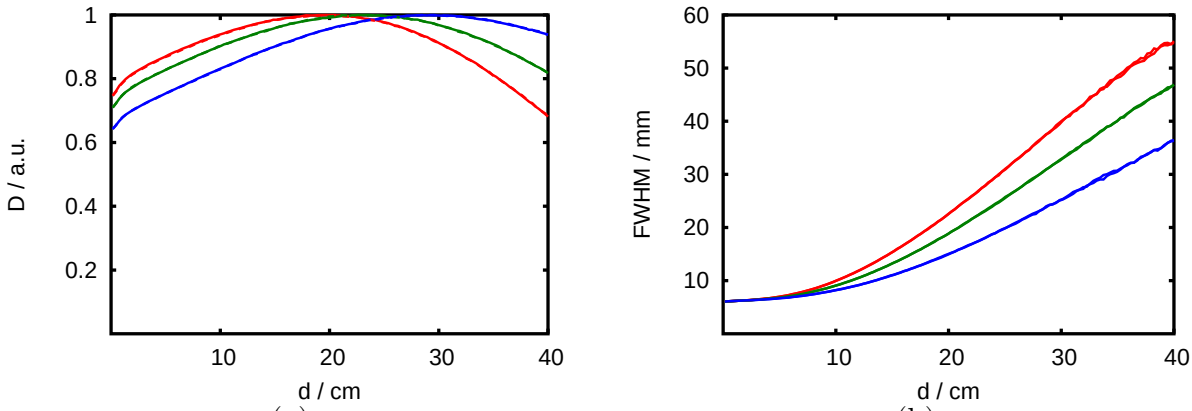

(a) (b)

Figure 11.3: (a) The DDCs and (b) the FWHM of the lateral dose profiles for 150 MeV (red), 185 MeV (green) and 250 MeV (blue) electrons. The curves for electrons with no energy spread (dashed lines) fit almost exactly to the ones with the experimentally observed energy spreads (solid line) and are nearly completely covered by the latter.

11.4 Variation of source to surface distance and focused beam

Due to the divergence of the beam the source to surface distance (SSD) influences the intensity of the electron beam at the phantom surface and therefore the dosimetric distribution inside (because of the small divergence angle of 6 mrad the depth dose curve does not change).

To quantify the influence the SSD is varied between 1 cm and 100 cm for an electron energy of 185 MeV. Moreover a refocusing set-up is investigated where it is assumed that compact magnetic fields refocus the electron beam (figure 11.4, [17]). Chromatic abberations due to the energy spread of the spectrum are neglected. The focal spot position f is given by the corresponding depth in the water phantom. This definition implies that the intensity of an unfocused electron beam with SSD d and a focused electron beam with focal length $f = d$ yield the same intensity profile on the phantom surface.

Figure 11.5 shows the FWHM for various distances. The electron peak energy is 185 MeV and the energy spread 8%. At the phantom surface the lateral spread is proportional to the distance to the source. Inside the phantom scattering leads to an increase of the FWHM. In addition this increase is amplified by the divergence of the

[1]By the courtesy of the Groupe Sources de Particules par Laser, Laboratoire d'Optique Appliqée, CNRS, ENSTA, Palaiseau, France

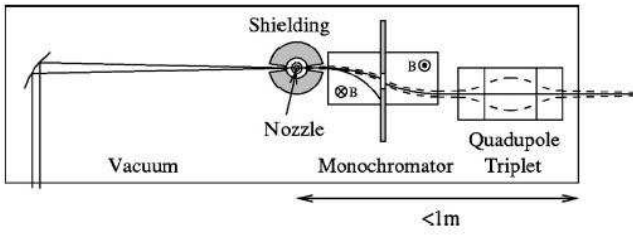

Figure 11.4: [1]Sketch of a compact device to remove low energy electrons and refocus the electron beam. The laser is focused using an off-axis parabola onto a gas jet to accelerate electrons. Dangerous radiation produced at the nozzle is shielded. Low energy electrons are filtered by a monochromator. A quadrupole triplet refocuses the electron beam.

electron beam. E.g. at a depth of 10 cm the FWHM yields 5.6 mm for $d = 1$ cm, 6.2 mm ($d = 30$ cm), 7.3 mm ($d = 60$ cm) and 9.1 mm ($d = 100$ cm). As the effect of the divergence on the FWHM is of the same order as the effect of scattering the distance between source and surface should be as small as possible.

Since it is unfeasible to apply source to surface distances of only a few centimeters, refocused beams [17] are considered. The depth of the focal spot is varied for an electron peak energy of 185 MeV. $f = 15$ cm and $f = 30$ cm are compared to an unfocused beam with distance $d = 30$ cm (figure 11.5 (b)). The FWHM at the phantom surface is slightly reduced for the focused beams but the overall shape is nearly the same for all three set-ups. The advantage of the refocused beams is of course the possibility to apply them with a larger SSD.

In the end an expample with included scattering in air is given. The lateral spread of 250 MeV electron beams with $d = 100$ cm of course reduces by focusing. Figure 11.5 (b) shows a comparison of an unfocused beam propagating in vacuum and a focused beam ($f = 0$ cm) propagating through air. The broadening due to scattering in air is suppressed by focusing and the lateral spread is actually slightly reduced.

11.5 Comparison to 6MV photons

The depth dose curve of laser-accelerated electrons compares favorably with the one of photons for deep-seated tumors. The maximum is placed at large depths and the depth dose curve does not decrease exponentially behind the maximum. This means that in case of electrons the high dose values penetrate deeper compared to photons.

To evaluate the possible advantages of electron beams in contrast to 6 MV photon beams in more detail the lateral spread for various electron beam set-ups is compared to the penumbra (distance of 90-10% dose) of a 6 MV photon treatment field. The convolution of the Heaviside function with a lateral Gaussian profile gives an estimation

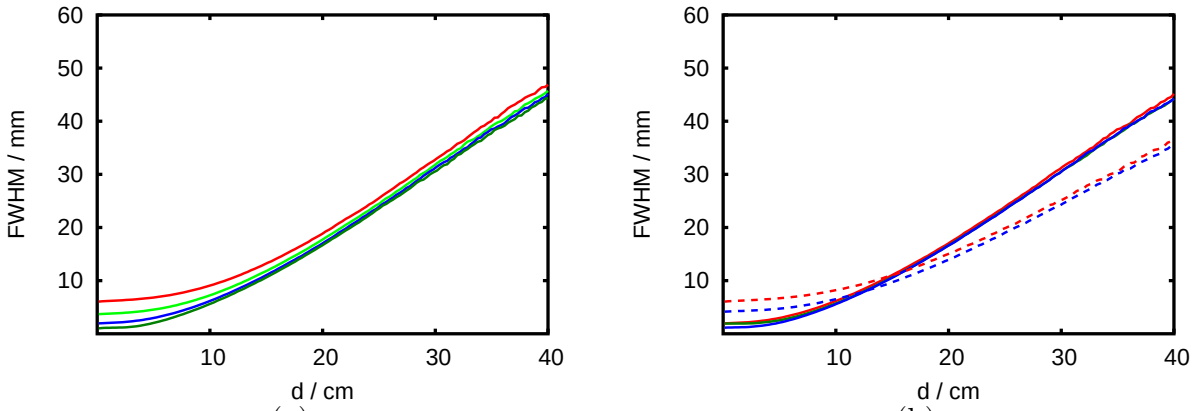

Figure 11.5: (a) Comparison of the FWHM for variuos SSDs (d = 100 cm (red), d = 60 cm (light green), d=30 cm (blue), d = 1 cm (dark green)) of a 185 MeV electron beam. (b) Comparison of focused electron beams (f = 30 cm (green), f = 15 cm (blue)) an electron beam with a SSD of 30 cm (red) , a 250 MeV electron beam with d = 100 cm (red dashed line) and a 250 MeV refocused beam (f = 0 cm, blue dashed line) for which scattering in air is included.

of the penumbra of an electron treatment field.

For a distance of 100 cm the penumbra (table 11.1) of unfocused electron beams is always larger than for the photon treatment field. For focused electron beams however at a depth of 5 cm the penumbra is smaller. Depending on the peak energy, the depth where the electron beam penumbra equals the one of the photon beam can exceed 10 cm. When scattering in air is included this feature still holds. For depths below 5 cm the penumbra for electron beams is still smaller than the one of a photon treatment field.

	d = 100 cm			f = 30 cm			f = 0 cm	
Depth	150MeV	185MeV	250MeV	150MeV	185MeV	250MeV	250MeV	6MV
1 cm	5.6	5.6	5.6	1.7	1.7	1.7	3.8	3.9
5 cm	6.3	6.1	6.0	2.6	2.3	2.0	4.3	4.5
10 cm	9.0	8.2	7.4	6.3	5.2	3.9	5.8	4.5
15 cm	13.8	11.9	10.0	11.8	9.5	7.1	8.7	4.5

Table 11.1: The estimated penumbra (90-10%, in mm) of unfocused (d = 100 cm) and focused (f = 30 cm) electron beams as well as for 250 MeV electrons for which scattering in air is included (f = 0 cm). The penumbra of focused beams are smaller than the penumbra of 6 MV photons at small depths.

In conclusion laser-accelerated electrons demonstrate some advantageous dosimetric properties compared to photons. Regarding deep-seated tumors the depth dose curves show broad maxima and no exponential decrease. The lateral penumbra for some electron beam set-ups (e.g. 250 MeV, refocused beams) is smaller at shallow depths compared to the one of photons. To check if these advantages result in an improvement of treatment plan quality a clinically approved photon prostate plan is compared to treatment plans with intensity modulated laser-accelerated electron beams.

12 Treatment planning - comparison to 6MV photons

To investigate if the dosimetric properties of laser-accelerated electrons compared to photons result in an improvement of treatment plan quality a comparison of treatment plans is made. The starting point is a clinical approved prostate intensity modulated radiation therapy (IMRT) treatment plan (see section 7.3.4) which is compared to various set-ups of electron beams supposedly created by laser-plasma accelerators. The electron beams are also intensity modulated at a fixed peak energy. Details regarding optimization and dose calculation were already presented in section 7.3.3.

12.1 Comparison of electron and photon treatment plans

The optimization parameters of the original photon plan, such as beam directions and penalty factors, are retained for electron treatment plans. The prescribed dose to the gross tumor volume (GTV) is 76 Gy. The spatial resolution of the photon bixels is 5×5 mm^2 while the distance between two electron beamlets is 2.5 mm. To compare the treatment plans the respective target coverage and dose sparing of organs at risk are compared. For that purpose minimum, maximum and mean doses (normalized to the mean dose of the GTV) as well as dose-volume histograms are investigated.

The electron beam set-ups are chosen as in table 11.1, i.e. the influence of the peak energy (150 MeV, 185 MeV and 250 MeV), focusing the beam ($d = 100$ cm vs. $f = 30$ cm) and one exemplary case including scattering in air are studied.

Concerning the target coverage for electron beams at a constant SSD of $d = 100$ cm the minimum dose to the GTV is almost independent of the electron energy. For 150 MeV electrons the minimum dose to the GTV is 87.9%. For 185 MeV it is 88.2% and for 250 MeV it is again 87.9%. These values are similar to the minimum dose for the photon plan of 87.8%. Focused electron beams show a slightly increased minimum dose: 88.0%, 88.3% and 88.0% are achieved for 150 MeV, 185 MeV and 250 MeV respectively. The value for the set-up with included scattering in air, 88.3% also exceeds the minimum dose for photons. In addition the maximum dose to the GTV for electron beams is always smaller (103.4%-103.8%) than for the photon plan (105.%).

In the following the comparison is restricted to four exemplary electron beam set-ups

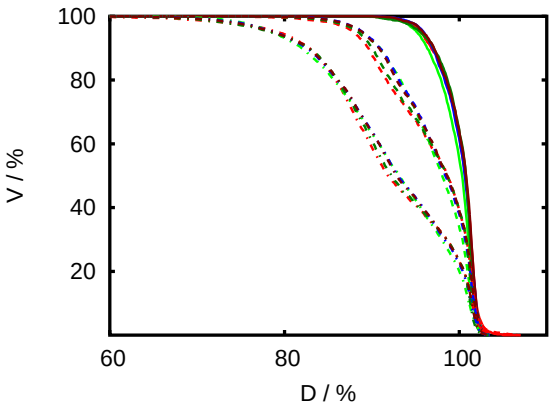

Figure 12.1: Dose-volume histograms for GTV (solid line), CTV (dashed line) and PTV (dashed-dotted line). Four electron beam set-ups - 150 MeV, $d = 100$ cm (light green), 250 MeV, $d = 100$ cm (blue), 250 MeV, $f = 30$ cm (dark green) and 250 MeV with scattering in air (dark red) - are compared to a 6 MV photon plan (red). For all 250 MeV electron plans the target coverage is almost the same as for the photon plan.

because the trend observed for the GTV - electron plan quality improves with increasing electron energy and focusing - holds for most plan properties. For a SSD of $d = 100$ cm two electron peak energies, 150 MeV and 250 MeV, are chosen. Furthermore the focused 250 MeV electron beam as well as the electron beam with included scattering in air are compared to the photon plan.

The dose values of the clinical target volume (CTV) show the same trend as for the GTV (table 12.1). Focusing increases/reduces the minimum/maximum dose to the CTV. In addition for all set-ups the minimum dose exceeds the one of photons while the maximum dose for electron beams goes below the one of photons. In the planning target volume (PTV) this trend is also visible for the maximum dose but it is reversed for the minimum dose. But in all cases the minimum dose to the PTV is larger than in the photon case.

Summing up the target coverage can be slightly improved by increasing peak energy and focusing the electron beam. For 250 MeV the target coverage is almost the same as in the case of photons (figure 12.1).

Regarding organs at risk and the remaining normal tissue the mean dose is slightly reduced by all electron beam set-ups (except left femur 12.6%-13.7% for electrons compared to 11.8% for photons). The maximum dose values differ only slightly from the one of the photon plan for rectum, bladder and normal tissue. In case of the femurs the maximum dose is slightly increased for electron beams.

The mean dose to bladder and rectum is again decreasing with electron energy and focusing. For 250 MeV, focused beams it is reduced by 22% (bladder) and 14% (rectum)

		$d = 100$ cm		$f = 30$ cm	$f = 0$ cm	
		150 MeV	250 MeV	250 MeV	250 MeV	6MV
GTV	D_{min}	87.9	87.9	88.0	88.3	87.8
	D_{mean}	100.0	100.0	100.0	100.0	100.0
	D_{max}	103.8	103.4	103.3	103.4	105.0
CTV	D_{min}	69.8	69.8	71.0	70.3	67.8
	D_{mean}	97.4	97.2	96.9	97.2	96.8
	D_{max}	103.8	103.4	103.3	103.4	107.
PTV	D_{min}	61.6	57.7	52.5	56.6	49.7
	D_{mean}	92.7	92.5	92.2	92.5	92.1
	D_{max}	103.8	103.4	103.3	103.4	107.
Rectum	D_{min}	0.1	0.0	0.0	0.0	3.3
	D_{mean}	37.8	34.7	33.9	34.7	39.6
	D_{max}	97.5	99.1	99.8	99.5	100.1
Bladder	D_{min}	0.0	0.0	0.0	0.0	3.4
	D_{mean}	35.8	32.7	30.6	32.1	39.1
	D_{max}	95.8	97.0	98.7	97.7	98.6
Femur (right)	D_{min}	1.9	0.7	0.3	0.5	2.9
	D_{mean}	15.8	16.3	16.7	16.5	17.2
	D_{max}	36.3	36.1	42.0	38.3	33.7
Femur (left)	D_{min}	1.0	0.1	0.0	0.0	1.9
	D_{mean}	12.6	13.0	13.7	13.3	11.8
	D_{max}	41.6	40.8	46.2	42.3	41.5
Normal tissue	D_{min}	0.0	0.0	0.0	0.0	0.0
	D_{mean}	14.5	14.1	13.5	13.9	16.7
	D_{max}	103.8	103.4	103.3	103.4	107.0

Table 12.1: Maximum, minimum and mean dose (in %, normalized to the mean dose to the GTV) of target volumes, organs at risk and normal tissue. Four exemplary electron beam set-ups - 150 MeV and 250 MeV for a SSD of $d = 100$ cm, 250 MeV focused at a depth of $f = 30$ cm and 250 MeV with a SSD of $d = 100$ cm, focused at the surface with included scattering in air - are compared to a 6 MV photon plan.

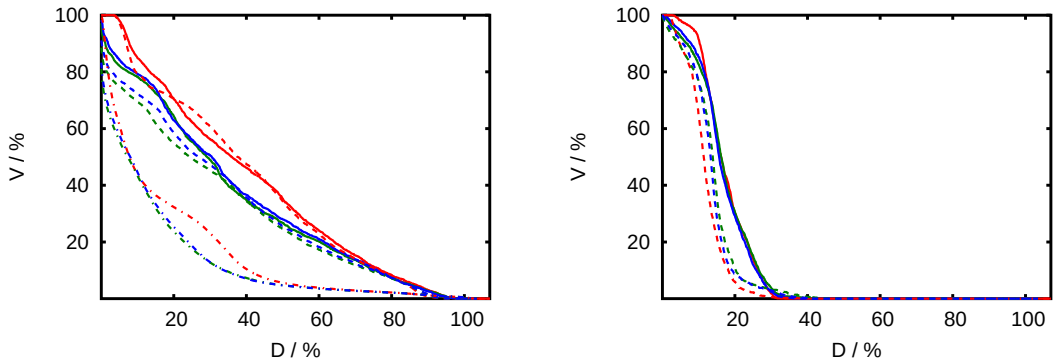

Figure 12.2: Dose-volume histograms for organs at risk and normal tissue for 250 MeV electrons ($f = 30$ cm (green) and scattering in air included (blue)) compared to the photon (red) DVHs. The dose sparing of rectum (solid line (a)) and bladder (dashed line (a)) is improved. The dose sparing of normal tissue (dash-dotted line (a)) is improved between 20 % and 40% while the DVHS of femurs ((b) right -solid line, left - dashed line) are slightly changed.

compared to the mean dose in the case of the photon plan. Even for the electron beam with included scattering in air a reduction of 18% respectively 12% is achieved. However the mean dose to the femurs (right/left) is increasing with peak energy and focusing, from 15.8%/12.6% to 16.7%/13.7% compared to 17.2%/11.8% for photons. Concerning the remaining normal tissue a reduction of the mean dose is achieved by all electron plans compared to the photon plan. The largest reduction by 19% is obtained for the 250 MeV, focused set-up.

The dose-volume histograms show the improvement in plan quality for 250 MeV, focused electrons (no scattering/scattering included) in more detail. The target coverage (figure 12.1) is almost the same for electrons and photons. In case of rectum and bladder the volume which receives a certain dose is reduced for almost all dose values (figure 12.2 (a)). The DVHs of the two electron plans differ only slightly.

The DVH of the right femur changes only slightly for the electron plans compared to the photon plan (figure 12.2 (b)). For the left femur the volume which receives 20-40% of the maximum dose is increased for the electron plans.

Summary

The observed moderate improvement of plan quality for 250 MeV can be explained at first by the characteristics of the depth dose curve. For electrons the maximum is placed at larger depths compared to photons. Furthermore the DDC decreases only slowly behind the maximum. The smaller penumbra compared to the one of photons for small depths (table 11.1) is also a basis for plan quality improvement.

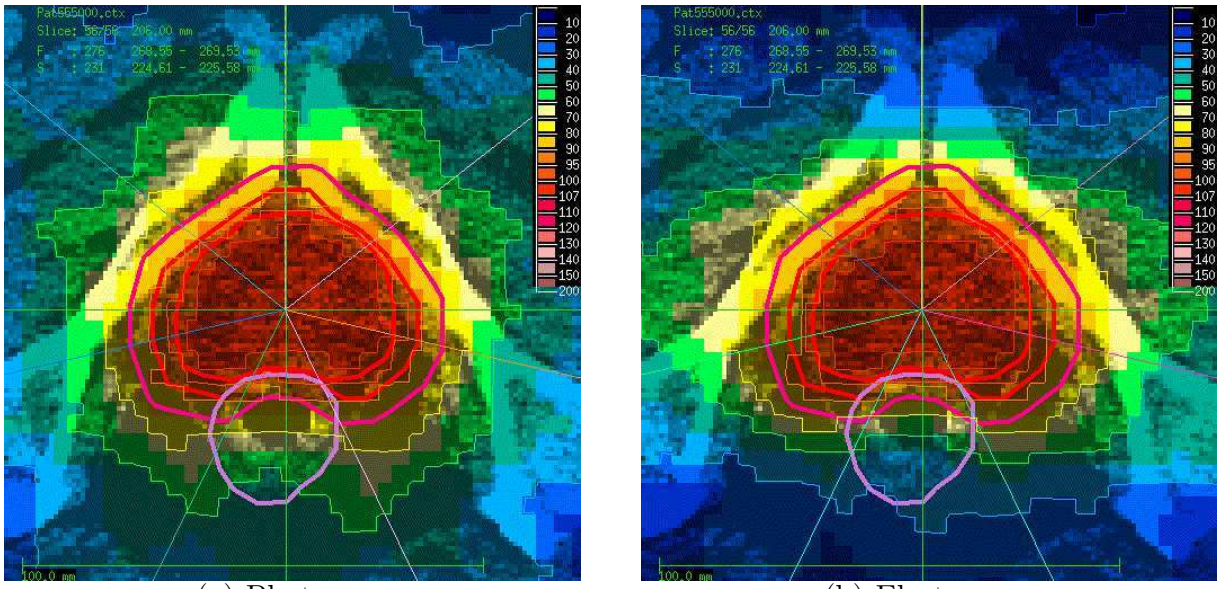

(a) Photons (b) Electrons

Figure 12.3: Transversal dose distribution (in % of the mean dose to the GTV) for (a) photons and (b) 250 MeV, focused ($f = 30$ MeV) electrons.

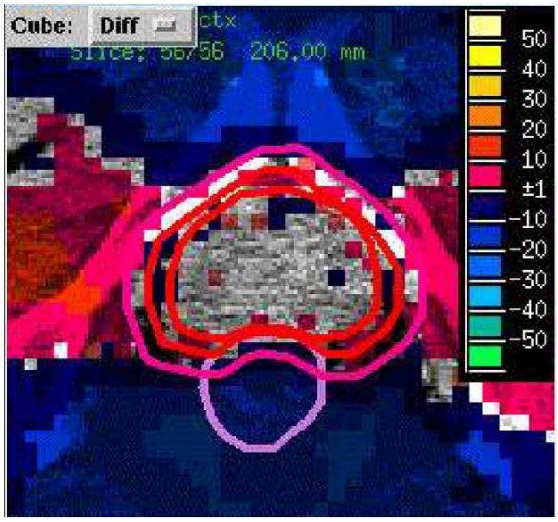

Figure 12.4: The difference between electron dose and photon dose (in % of the mean dose to the GTV), $D_{el} - D_{ph}$, in a transversal slice.

The dose distribution in a typical transversal CT slice (250 MeV, photons focused versus; figure 12.3) illustrates the above noted results. The target coverage is almost

the same in both cases. But one can observe that the dose sparing of the rectum and normal tissue is better for electron beams. The difference of the two dose distributions (figure 12.4) shows this more clearly. The dose to organs at risks as well as to most of normal tissue is lower for the electron beam (except for the femurs). This exception is due to the geometrical configuration of the beams (the femurs are placed in the tail of electron beams number two and six (figure 7.13)).

13 Conclusions and outlook

Laser-accelerated electrons with energies ranging from $150 - 250$ MeV exhibit some advantageous dosimetric characteristics compared to photons. Regarding deep-seated tumors the depth dose curve shows a broad maximum at large depths (≥ 20 cm). The lateral penumbra of treatment fields for focused electron beams is smaller compared to 6 MV photons at depths smaller than 10 cm. These advantages result in a slight improvement of the quality of selected clinical cases, e.g. for an IMRT prostate plan. While the target coverage is almost the same for 250 MeV electrons compared to photons the dose sparing of sensitive structures is improved. E.g. the mean dose to the bladder is reduced by 22% for 250 MeV, focused electrons. These findings agree well with previous results regarding very high energy electrons as a treatment modality [13, 14, 15]. The lack of compact and cost-efficient electron accelerators could be overcome by laser-plasma systems.

As laser-accelerated electrons can improve treatment plan quality one has to check if laser-plasma accelerators can provide an electron beam with sufficient charge in reasonable time. The maximum dose on the central axis of a laser-accelerated electron beam yields e.g. 0.1 Gy per shot for 250 MeV, focused electrons with scattering in air included. However, when delivering the dose in a pencil beam scanning mode, the maximum dose of most of the optimized pencil beams is of the order of $\lesssim 0.1$ Gy and thus can be delivered by a laser-plasma accelerator. As the charge can be tuned continously by rotating the polarization of the two laser beams, in principle every needed spot weight can be performed by one single laser shot. At a distance of 2.5 mm between each spot a total number of ~ 5000 spots is required. Since the laser is operating at an frequency of 10 Hz, this results in ~ 10 minutes "beam-on time".

To study in more detail the influence of tissue inhomogeneities the dose distribution should be recalculated via Monte Carlo simulations. In a next step the optimization could be based on D_{ij}-matrices which are calculated by Monte Carlo simulations. Furthermore the dose deposition of an electron beam has to be characterized experimentally to verify the Monte Carlo simulation results. In the long run the effect of the short time of dose application (a single electron bunch is expected to deliver a maximum dose of ~ 0.1 Gy in ~ 100 fs) has also to be investigated.

Part III

Summary

Summary

In this work basic characteristics of laser-accelerated particles and their potential application to radiotherapy were studied. The work was divided into two parts analyzing protons (part I) and electrons (part II) respectively.

At first the scaling of the maximum proton energy was studied. An analytical model [50] was compared to one- and two-dimensional PIC simulations as well as to experimental data from literature. The model was extended by a characteristic acceleration time coefficient R which takes into account that in laser-plasma experiments the expansion is adiabatic in contrast to the isothermal theoretical approach. If a dependency of R on the laser pulse duration is assumed, a good agreement of the model with one- and two-dimensional PIC simulations was found for a wide range of parameters.

The comparison of the model to experimental data from literature shows in general that for experiments with a high contrast of pre- and main pulse the theoretical approach agrees well with the experimental results. However for low contrast experiments the deviations between the model and the experimental results become larger.

But all investigations show that the model provides a quite reliable scaling of the maximum proton energy. Therefore an estimation of the laser intensity needed for clinically usable proton energies was made. It turns out that intensities of a few times $10^{21} W/cm^2$ - which will be available with future laser systems - might result in proton energies of more than 200 MeV.

As typical proton energy spectra yield a Maxwellian shape which is inadequate for radiotherapy, set-ups to modify the proton spectra were studied. In a first approach the proton bunch was manipulated by generating large electric fields at a second target by a second laser to separate high and low energy protons. Unfortunately due to an additional expansion the early creation of a "quasi-monoenergetic" high energy part does not hold in the long run of the simulation. On the other hand studies of so-called double-layer targets [10] were much more encouraging. The acceleration of a thin proton layer initially attached to a heavy ion substrate leads to a separated high energy part in the proton spectrum. One-dimensional PIC simulations describe the dependency of the width of the energy spectrum on the target constituents and are in good agreement with an analytical approach [56]. Based on this model and additional two-dimensional simulations the energy spread for clinically relevant energies was estimated. Assuming that a minimum current of 1 nA is ensured, prostate treatment plans of two hypothetic proton beams with different relative energy spreads (10% and 50%) were used for comparative treatment planning with conventional photon and proton plans. Even for the "worst case" scenario the laser-accelerated protons led to an improvement of treatment plan quality compared to the conventional photon plan.

These results raise hope that one might benefit from the advantages of laser-plasma accelerators, i.e. their compactness and cost efficiency, in the future. However besides the experimental validation of the scaling of the maximum energy and the creation of

"quasi-monoenergetic" proton beams with double-layer targets at high energies, additional "technical" obstacles have to be overcome. E.g. the reproducibility of the energy spectrum (which the current laser systems do not ensure) has to be controlled within a few percent for any clinical application. Another challenge will be the dosimetry of the sub-picosecond proton bunches. Furthermore, the biological effects of this extremely short time dose application have to be studied.

The other potential application of laser-accelerated particles is related to the use of high-energy electrons ($150 - 250$ MeV). In contrast to the maximum energy of protons accelerated by laser-plasma interactions, the current laser systems are capable of electron energies proposed by several groups [13, 14, 15] for the application in radiotherapy. However, these studies were based on hypothetical monoenergetic electron spectra as compact and cost efficient conventional accelerators to achieve these energies are not available. This lack might be overcome by the use of laser-plasma accelerators. The analysis of "quasi-monoenergetic" electrons obtained with laser-plasma accelerators in part II of this work agrees well with the results of the previous studies. Monte Carlo simulations show that regarding deep-seated tumors the depth dose curve of high energy electrons compares favorably to the one of photons as it yields a broad maximum at large depths (≥ 20 cm). In addition the lateral penumbra of treatment fields for focused electron beams is smaller compared to 6 MV photons at depths smaller than 10 cm. These advantages result in a slight improvement of the quality of an exemplary prostate electron treatment plan compared to a conventional photon plan.

Moreover as laser-plasma accelerators provide a reasonable dose rate one might think of an application in radiotherapy. But before finally evaluating the slight improvement in treatment plan quality, additional investigations have to be performed. E.g. the influence of inhomogeneities should be incorporated by Monte Carlo simulations, the dose deposition of an electron beam has to be characterized experimentally and like for protons the biological effects of the short time of dose application (a single electron bunch is expected to deliver a maximum dose of ~ 0.1 Gy in ~ 100 fs) have to be studied.

Concluding, though for laser-accelerated protons as well as for electrons various obstacles have to be overcome before an application in radiotherapy might be realized, the above findings motivate further efforts to study the potential of laser-accelerated particles in more detail.

A Mora's model

A.1 Electric field at the ion front

To calculate the electric field at the ion front,

$$E_{x,front} = \int_{x_f}^{\infty} \partial_x^2 \phi dx, \tag{A.1}$$

$$\tag{A.2}$$

the Poisson equation is solved:

$$\partial_x^2 \phi = \frac{e(n_e - Zn_i)}{\epsilon_0} \tag{A.3}$$

$$= \frac{en_{e0}}{\epsilon_0} \exp\left(\frac{e\phi}{k_B T_e}\right) \tag{A.4}$$

$$\longrightarrow \partial_x \left(\partial_x \phi\right)^2 = \frac{2en_{e0}}{\epsilon_0} (\partial_x \phi) \exp\left(\frac{e\phi}{k_B T_e}\right) \tag{A.5}$$

$$\longrightarrow \int_{x_f}^{\infty} \partial_x \left(\partial_x \phi\right)^2 dx = \int_{\phi(x_f)}^{\phi(\infty)} \frac{2en_{e0}}{\epsilon_0} \exp\left(\frac{ey}{k_B T_e}\right) dy. \tag{A.6}$$

With $\partial_x \phi(x \to \infty) \to 0$ and $\phi(x \to \infty) \to -\infty$ the field at the ion front yields

$$E_{x,front} = \sqrt{2} E_{x,0} \exp\left(\frac{e\phi_f}{2k_B T_e}\right) \tag{A.7}$$

$$= \sqrt{2} E_{x,0} \sqrt{\frac{n_{ef}}{n_{e0}}} \tag{A.8}$$

with $E_{x,0} = \sqrt{\frac{n_{e0} k_B T_e}{\epsilon_0}}$.

For $x = 0$ at $t = 0$, $\phi(0)$ is calculated by integrating Poisson's equation from $-\infty$ to $x = 0$,

$$\phi(0) = -\frac{k_B T_e}{e}. \tag{A.9}$$

Therfore the electric field at the ion front at $t = 0$ yields

$$E_{x,front} = \sqrt{\frac{2}{\exp(1)}} E_{x,0}. \tag{A.10}$$

A.2 Electric field

Integrating equation (A.5) from x (instead of x_f) to ∞ results in (equation A.7)

$$\partial_x \phi(x) = -\sqrt{2} E_{x,0} \exp\left(\frac{e\phi(x)}{2k_B T_e}\right). \tag{A.11}$$

Separation of variables yields

$$-\frac{2k_B T_e}{e}\left[\exp\left(-\frac{e\phi(x)}{2k_B T_e}\right) - \exp\left(-\frac{e\phi(0)}{2k_B T_e}\right)\right] = -\sqrt{2} E_{x,0} x \tag{A.12}$$

and with (A.9)

$$\phi(x) = -2\frac{k_B T_e}{e} \ln\left(\sqrt{\exp(1)} + \frac{1}{\sqrt{2}}\frac{x}{\lambda_D}\right). \tag{A.13}$$

Thus the electric field is

$$E_x(x) = \sqrt{\frac{2}{\exp(1)}} E_{x,0} \frac{1}{1 + x/\sqrt{2\exp(1)}\lambda_D} \tag{A.14}$$

A.3 Energy spectrum

To calculate the energy distribution,

$$\left(\frac{dN}{dE}\right)_{ion} = \frac{\partial N}{\partial x}\frac{\partial x}{\partial v}\frac{\partial v}{\partial E}, \tag{A.15}$$

the three terms are evaluated separately.

$$\frac{\partial N}{\partial x} = n_i \tag{A.16}$$

$$= n_{i0} \exp\left(\frac{-v_i}{c_s}\right) \qquad \text{(eqn.(3.8))} \tag{A.17}$$

$$= n_{i0} \exp\left(-\sqrt{\frac{2E}{Z k_B T_e}}\right), \tag{A.18}$$

$$\frac{\partial x}{\partial v} = t \qquad \text{(eqn.(3.8))}, \tag{A.19}$$

$$\frac{\partial v}{\partial E} = \sqrt{\frac{1}{2m_i E}}. \tag{A.20}$$

And therefore

$$\frac{dN}{dE} = \frac{n_{i0} c_s t}{\sqrt{2Z k_B T_e E}} \exp\left(-\sqrt{\frac{2E}{Z k_B T_e}}\right). \tag{A.21}$$

B Albright's model

B.1 Potential and electric field in region I

In region I holds $\varphi'' = \exp(\varphi)$. Integrating from ξ to infinity yields ($\partial_\xi\varphi(\infty) = 0$, $\varphi(\infty) = -\infty$)

$$\int_\xi^\infty \partial_{\xi'}(\partial_{\xi'}\varphi)^2 d\xi' = \int_\xi^\infty 2\partial_{\xi'}\varphi \exp(\varphi) d\xi' \tag{B.1}$$

$$\partial_\xi\varphi^2 = 2\exp(\varphi) \tag{B.2}$$

$$\partial_\xi\varphi = -\sqrt{2}\exp(\varphi/2). \tag{B.3}$$

The negative square root is taken as the electric field is positive in region I. Further integration from ξ_L to ξ results in

$$\int_{\xi_L}^{\xi} \partial_{\xi'}\varphi \exp(-\varphi/2) d\xi' = \int_{\xi_L}^{\xi} -\sqrt{2} d\xi' \tag{B.4}$$

$$\exp(-\varphi/2) - \exp(-\varphi_{L,I}/2) = (\xi - \xi_L)/\sqrt{2} \tag{B.5}$$

$$\varphi = -2\ln[\exp(-\varphi_{L,I}/2) + (\xi - \xi_L)/\sqrt{2}] \tag{B.6}$$

with $\varphi_{L,I} \equiv \lim_{\xi\downarrow\xi_L} \varphi(\xi)$. And therefore

$$\partial_x\varphi = \frac{-\sqrt{2}}{\exp(-\varphi_{L,I}/2) + (\xi - \xi_L)/\sqrt{2}}. \tag{B.7}$$

B.2 Potential and electric field in region II

In region II holds $\varphi'' = \exp(\varphi)$ with $\varphi_{L,II} = \varphi_{L,I} \equiv \varphi_L$, i.e. continuous potential, and $\varphi'_{L,II} = \varphi'_{L,I} + q$, i.e. discontinuous electric field due to the singularity in the light-ion charge. Integration from ξ to ξ_L as in B.1 gives

$$(\partial_x\varphi)^2 = (\partial_x\varphi_{L,II})^2 - 2[\exp(\varphi_{L,II}) - \exp(\varphi)] \tag{B.8}$$

Inserting the matching conditions and equation (B.3) results in

$$(\partial_x\varphi)^2 = 2[\exp(\varphi) - (\sqrt{2}q\exp(\varphi_L/2) - q^2/2)] \tag{B.9}$$

$$\partial_x\varphi = \sqrt{2}p[\exp(\varphi) - a]^{1/2} \tag{B.10}$$

with $a = q\left(\sqrt{2}\exp(\varphi_L/2) - q/2\right)$, $p = \pm 1$. Integrating from ξ to ξ_L gives (for $a > 0$)

$$\sqrt{2}p(\xi_L - \xi) = \int_{\varphi}^{\varphi_L} \frac{dx}{\sqrt{\exp(x) - a}} \tag{B.11}$$

$$\overset{[79],p.89}{\Longrightarrow} \sqrt{2}p(\xi_L - \xi) = \frac{2}{\sqrt{a}}\Big[\arctan(\sqrt{\exp(\varphi_L)/a - 1}) - \arctan(\sqrt{\exp(\varphi)/a - 1})\Big] \tag{B.12}$$

$$\overset{[79],p.47}{\Longrightarrow} \sqrt{2}p(\xi_L - \xi) = \frac{2}{\sqrt{a}}\arctan\left[\frac{\sqrt{\exp(\varphi_L)/a - 1} - \sqrt{\exp(\varphi)/a - 1}}{1 + \sqrt{(\exp(\varphi_L)/a - 1)(\exp(\varphi)/a - 1)}}\right] \tag{B.13}$$

Defining $\gamma = \tan\left((\xi_L - \xi)\sqrt{a/2}\right)$ yields

$$\varphi = \varphi_L + \ln\left(1 + \gamma^2\right) - 2\ln\left(1 + p\gamma\sqrt{\exp(\varphi_L)/a - 1}\right). \tag{B.14}$$

B.3 Energy spread

The energy spread of the beam is estimated in a rough way. In one dimension the initial charge density of the proton layer (charge Q, initial width L_0) is much larger than the local hot electron density. Therefore the expansion is driven by the repulsive forces between the protons. The rightmost proton, which feels the strongest electric field, obeys the equation of motion in the center of mass frame

$$m_i \frac{d^2}{dt^2}x = eE(x). \tag{B.15}$$

x is the distance from the center of the slab. The electric field at the edge of the slab is constant,

$$E(x) = \int_0^x \partial_x E dx - E(0) = \int_0^x \frac{\rho}{\epsilon_0}dx = x\frac{\rho}{\epsilon_0} = x\frac{Q}{2x}\frac{1}{\epsilon_0} = \frac{Q}{2\epsilon_0}. \tag{B.16}$$

The equation of motion yields

$$\frac{d^2}{dt^2}x = \alpha \quad \text{with}\, \alpha = \frac{eQ}{2m_i\epsilon_0}. \tag{B.17}$$

This results in the velocity $v(t) = \alpha t$ (the ion is initially at rest) and position $x(t) = \alpha t^2/2 + L_0/2$. The expansion is stopped if the hot electron density equals the density of the expanding proton layer, $n_i(t) \overset{!}{\approx} \bar{n}_{e,h}\exp(\varphi_L)$. The corresponding expansion time is

determined by

$$n_i(t) = \frac{Q}{2x(t)e} = \bar{n}_{e,h}\exp(\varphi_L) \tag{B.18}$$

$$\frac{Q}{e(\alpha t^2 + L_0)} = \bar{n}_{e,h}\exp(\varphi_L) \tag{B.19}$$

$$\frac{Q}{e\bar{n}_{e,h}\exp(\varphi_L)} = \alpha t^2 + L_0 \tag{B.20}$$

$$\sqrt{\frac{1}{\alpha}\left(\frac{Q}{e\bar{n}_{e,h}\exp(\varphi_L)} - L_0\right)} = t \tag{B.21}$$

$$\tag{B.22}$$

and gives the final velocity in the center of mass frame

$$v = \alpha t = \sqrt{\alpha\left(\frac{Q}{e\bar{n}_{e,h}\exp(\varphi_L)} - L_0\right)} \tag{B.23}$$

$$= \sqrt{\alpha L_0\left(\frac{n_{i0}}{\bar{n}_{e,h}\exp(\varphi_L)} - 1\right)}. \tag{B.24}$$

As $n_{i0} \gg \bar{n}_{e,h}\exp(\varphi_L)$ the second term can be neglected and with $q = Q/\bar{n}_{e,h}e\lambda_D$, $\lambda_D = \sqrt{\epsilon_0 k_B T_{e,h}/\bar{n}_{e,h}e^2}$:

$$v = \sqrt{\frac{\alpha Q}{e\bar{n}_{e,h}\exp(\varphi_L)}} \tag{B.25}$$

$$= \sqrt{\frac{Q^2}{2m_i\epsilon_0\bar{n}_{e,h}\exp(\varphi_L)}} \tag{B.26}$$

$$= \sqrt{\frac{q^2\bar{n}_{e,h}e^2\lambda_D^2}{2m_i\epsilon_0\exp(\varphi_L)}} \tag{B.27}$$

$$= \sqrt{\frac{q^2 k_B T_{e,h}}{2m_i\exp(\varphi_L)}}. \tag{B.28}$$

Therefore the difference in energy for the fastest and the slowest proton is

$$\Delta E = E_{max} - E_{min} = \frac{1}{2}m_i(v_0 + v)^2 - \frac{1}{2}m_i(v_0 - v)^2 \tag{B.29}$$

$$= 2m_i v_0 v \tag{B.30}$$

when the center of the slab is moving with v_0. Hence the relative energy spread yields

$$\frac{\Delta E}{E_0} = \frac{2m_i v_0 v}{\frac{1}{2}m_i v_0^2} \tag{B.31}$$

$$= \frac{4v}{v_0} \tag{B.32}$$

$$= \sqrt{\frac{16q^2 k_B T}{2m_i \exp(\varphi_L) v_0^2}} \tag{B.33}$$

$$= 2\sqrt{\frac{q^2 \exp(-\varphi_L) k_B T}{E_0}}. \tag{B.34}$$

$$\tag{B.35}$$

This result is consistent with Albright *et al.* 's [56] estimation,

$$\frac{\Delta E}{E_0} = \sqrt{\frac{q^2 \exp(-\varphi_L) k_B T}{E_0}}. \tag{B.36}$$

In three dimensions a layer with finite transverse extent $L \gg L_0$ has an upper bound on the energy spread. As long as $2x(t) \lesssim L$ the layer expands as in one dimension. Then the layer accelerates more slowly as it expands spherical [56]. The expansion time for $2x(t) \overset{!}{\approx} L$ is

$$\alpha t^2 + L_0 = L \tag{B.37}$$

$$t = \sqrt{(L - L_0)/\alpha} \tag{B.38}$$

resulting in the final velocity ($L \gg L_0$)

$$v = \alpha t = \sqrt{\alpha L} \tag{B.39}$$

$$= \sqrt{\frac{eQL}{2m_i \epsilon_0}}. \tag{B.40}$$

Hence the relative energy spread in three dimensions is given by

$$\frac{\Delta E}{E_0} = \frac{4v}{v_0} \tag{B.41}$$

$$= \sqrt{\frac{16eQL}{2m_i \epsilon_0 v_0^2}} \tag{B.42}$$

$$= 2\sqrt{\frac{eQL}{\epsilon_0 E_0}} \tag{B.43}$$

$$= 2\sqrt{\frac{e^2 q \bar{n}_{e,h} \lambda_D L}{\epsilon_0 E_0}} \tag{B.44}$$

$$= 2\sqrt{\frac{q k_B T_{e,h} L}{\lambda_D E_0}} \tag{B.45}$$

with $Q = q\bar{n}_{e,h}e\lambda_D$ and $\lambda_D = \sqrt{\epsilon_0 k_B T_{e,h}/\bar{n}_{e,h}e^2}$. Like in the one-dimensional case this estimation is according to Albright *et al.* 's result,

$$\frac{\Delta E}{E_0} = \sqrt{\frac{qk_B T_{e,h} L}{3\lambda_D E_0}} \tag{B.46}$$

$$= \sqrt{\frac{eQL}{3\lambda_D E_0}}. \tag{B.47}$$

C Plasma expansion

C.1 Determination of E(0)

For periodic boundary conditions holds

$$\int_0^L E(x)dx = -\int_0^L \partial_x \phi dx = 0 \tag{C.1}$$

and hence on a grid with grid points $i = 0, \ldots, NC$

$$\sum_{i=0}^{NC-1} E(i) = 0. \tag{C.2}$$

To determine the electric field at the origin of the grid $E(i = 0)$ [38], $\partial_x E = \rho$ is integrated from one grid point i to the next one,x $i + 1$,

$$\forall i \leq NC - 2 \qquad \int_{x_i}^{x_{i+1}} \partial_x E dx = \int_{x_i}^{x_{i+1}} \rho dx \tag{C.3}$$

$$E(i+1) - E(i) = \frac{\rho(i) + \rho(i+1)}{2}\Delta x \tag{C.4}$$

$$E(i+1) = E(i) + \frac{\Delta x}{2}\left(\rho(i) + \rho(i+1)\right) \tag{C.5}$$

$$= E(0) + \frac{\Delta x}{2}\sum_{j=0}^{i}\left(\rho(j) + \rho(j+1)\right) \tag{C.6}$$

$$\implies \forall 1 \leq i \leq NC - 1 \quad E(i) = E(0) + \frac{\Delta x}{2}\sum_{j=0}^{i-1}\left(\rho(j) + \rho(j+1)\right) \tag{C.7}$$

$$\implies \sum_{i=0}^{NC-1} E(i) = NC \cdot E(0) + \frac{\Delta x}{2}\sum_{i=1}^{NC-1}\sum_{j=0}^{i-1}\rho(j) + \rho(j+1) \tag{C.8}$$

$$\overset{equ.(C.2)}{\implies} 0 = NC \cdot E(0) + \frac{\Delta x}{2}\sum_{i=1}^{NC-1}\sum_{j=0}^{i-1}\rho(j) + \rho(j+1) \tag{C.9}$$

$$\implies E(0) = -\frac{\Delta x}{2NC}\sum_{i=1}^{NC-1}\sum_{j=0}^{i-1}\rho(j) + \rho(j+1). \tag{C.10}$$

D Scaling laws for laser-accelerated protons

D.1 1D PIC simulations

D.1.1 Absorption

The absorption is fitted to $f(\%) = \alpha a_0^\beta$. The curves represent $\tau_{las} = 100\ 1/\omega_0$,$d = 20\ c/\omega_0$ (red), $\tau_{las} = 500\ 1/\omega_0$,$d = 10\ c/\omega_0$ (light green), $\tau_{las} = 100\ 1/\omega_0$,$d = 60\ c/\omega_0$ (blue), $\tau_{las} = 500\ 1/\omega_0$,$d = 60\ c/\omega_0$ (dark green).

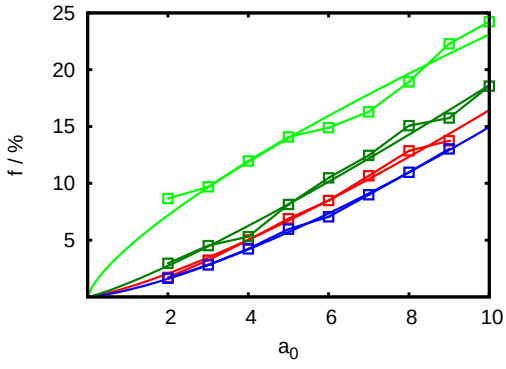

The table specifies the corresponding values for $\tau_{las} = 100, 200, 300, 400$ and $500\ 1/\omega_0$ and target thicknesses of $d = 10, 15, 20$ and $60\ c/\omega_0$.

	d / c/ω_0			
	10		15	
τ_{las} / $1/\omega_0$	α	β	α	β
100			0.9 ± 0.15	1.27 ± 0.075
200	1.5 ± 0.35	1.1 ± 0.12	1.0 ± 0.18	1.25 ± 0.084
300	3.0 ± 0.50	0.79 ± 0.083	1.7 ± 0.21	1.01 ± 0.062
400	4.9 ± 0.31	0.61 ± 0.033	4.2 ± 0.60	0.63 ± 0.074
500	4.4 ± 0.52	0.73 ± 0.060	4.8 ± 0.45	0.59 ± 0.051
	20		60	
τ_{las} / $1/\omega_0$	α	β	α	β
100	0.84 ± 0.98	1.29 ± 0.059	0.61 ± 0.038	1.39 ± 0.031
200	0.81 ± 0.10	1.34 ± 0.061	0.47 ± 0.074	1.47 ± 0.075
300	1.2 ± 0.15	1.16 ± 0.062	0.55 ± 0.096	1.41 ± 0.082
400	3.1 ± 0.25	0.75 ± 0.040	1.31 ± 0.13	1.10 ± 0.047
500	4.0 ± 0.37	0.65 ± 0.047	1.20 ± 0.14	1.2 ± 0.057

Fitting the absorption to $f(\%) = \alpha a_0^{\beta}$.

D.2 Comparison to experimental data

D.2.1 High contrast pre-pulse

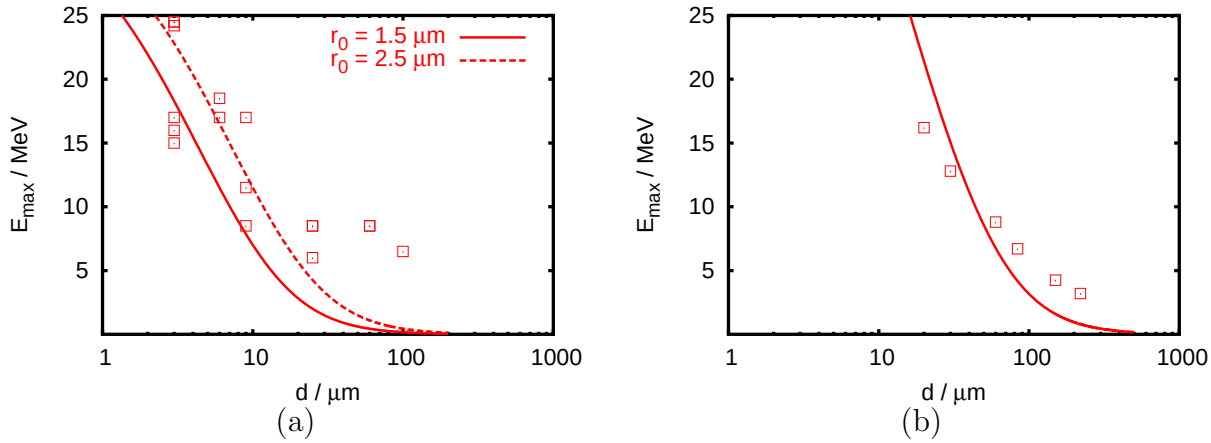

Figure D.1: Comparison of the analytical model with (a) data adapted from Mackinnon *et al.* [60] and Fuchs *et al.* [49].

The analytical model agrees well with the experimental data adapted from Mackinnon *et al.* [60] and Fuchs *et al.* [52] (figure D.1). For Mackinnon *et al.* the exact spot diameter is not specified.

D.2.2 Low contrast pre-pulse

The comparison of the maximum energy adapted from Oishi *et al.* [63] with the analytical approach yields deviations. The proton energy is underestimated by at least a factor of three (figure D.2).

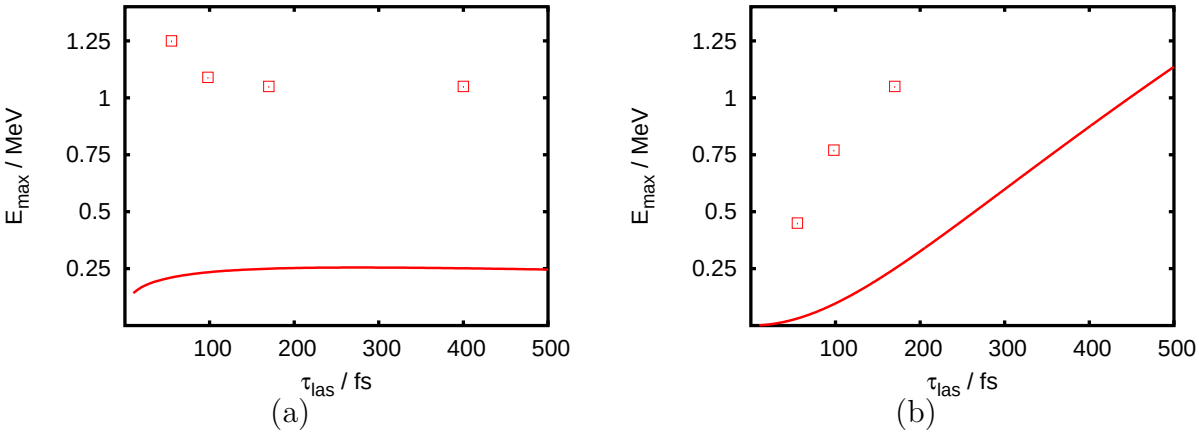

Figure D.2: Maximum energy versus pulse duration from Oishi *et al.* [63] for (a) constant laser energy, and (b) constant intensity, $I_{las} = 2.1 \times 10^{18} W/cm^2$. For constant energy the energy which results in $2.1 \times 10^{18} W/cm^2$ for $\tau_{las} = 170$ fs is chosen and kept constant.

List of Figures

List of Tables

Bibliography

[1] D. Umstadter, J. Phys. D **36**, R151 (2003)

[2] R. A. Snavely *et al.*, Phys. Rev. Lett. **85**, 2945 (2000)

[3] J. Faure *et al.*, Nature 444, 737 (2006)

[4] V. Malka *et al.*, Med. Phys. **31**, 1587 (2004)

[5] E. Fourkal *et al.*, Med. Phys. **29**, 2788 (2002)

[6] E. Fourkal *et al.*, Med. Phys. **34**, 577 (2007)

[7] C.-M. Ma *et al.*, Med. Phys. **33**, 571 (2006)

[8] for a review see e.g. D.W. Miller, Med. Phys. **22**, 1943 (1995)

[9] http://p-therapie.web.psi.ch/proscan.html

[10] T. Zh. Esirkepov *et al.*, Phys. Rev. Lett. **89**, 175003 (2002)

[11] H. Schwoerer *et al.*, Nature **439**, 445 (2006)

[12] B. M. Hegelich *et al.*, Nature **439**, 441 (2006)

[13] C. DesRosiers *et al.*, Phys. Med. Biol. **45**, 1781 (2000)

[14] C. Yeboah *et al.*, Phys. Med. Biol. **47**, 1285 (2002)

[15] C. Yeboah *et al.*, Phys. Med. Biol. **47**, 2247 (2002)

[16] E. Lefebvre *et al.*, Nucl. Fus., **43**, 629 (2003)

[17] Y. Glinec *et al.*, Med. Phys. **33**, 155 (2006)

[18] F. F. Chen, *Introduction to plasma physics and controlled fusion*, Plenum Press (1984)

[19] R.J. Goldston and P.H. Rutherford, *Plasmaphysik*, Vieweg (1998)

[20] P. Mulser, *High Power Laser-Matter Interaction*, lecture notes 2005/06, to be published in Springer

[21] B. Quesnel and P. Mora, Phys. Rev. E **58**, 3719 (1998)

[22] C. J. McKinstrie, Phys. Fluids, **31**, 278 (1988)

[23] F. Ewald, *Harte Röntgenstrahlung aus relativistischen Laserplasmen und laserinduzierte Kernreaktionen*, PhD thesis, Friedrich-Schiller-Universität Jena, 2004

[24] L. V. Keldysh, Sov. Phys. JETP **20**, 1307 (1965)

[25] S. Fritzler, *Particle sources with high-intensity lasers: A tool for plasma diagnostics and an innovative source for applications*, PhD thesis at École Polytechnique, France, 2003

[26] A. B. Langdon *et al.*, Phys. Rev. Lett. **44**, 575 (1980)

[27] J. P. Matte, Phys. Rev. A **45**, 2558 (1992)

[28] P. J. Catto *et al.*, Phys. Fluids **11**, 704 (1977)

[29] S. C. Wilks *et al.*, Phys. Rev. Lett. **69**, 1383 (1992)

[30] G. Malka *et al.*, Phys. Rev. Lett. **77**, 75 (1996)

[31] F. Brunel *et al.*, Phys. Rev. Lett. **59**, 52 (1987)

[32] J. P. Freidberg *et al.*, Phys. Rev. Lett. **28**, 795 (1972)

[33] D. Strickland *et al.*, Opt. Commun. **56**, 219 (1985)

[34] G. A. Mourou *et al.*, Physics Today (January 1998), 22 (1998)

[35] S. Fritzler *et al.*, Appl. Phys. Lett. **83**, 3039 (2003)

[36] P. Kenna *et al.*, Phys. Rev. Lett. **94**, 084801 (2005)

[37] M. Kaluza *et al.*, Phys. Rev. Lett. **93**, 045003 (2004)

[38] C. K. Birdsall and A.B. Langdon, *Plasma physics via computer simulations*, Institute of Physics Publishing, London (1991)

[39] E. d'Humières, *Accélération de protons par interaction laser-plasma et applications*, PhD thesis at Université Paris 6, 2006

[40] J. Denavit, Phys. Rev. Lett. **69**, 3052 (1992)

[41] A. Pukhov *et al.*, Phys. Rev. Lett. **79**, 2686 (1997)

[42] Y. Sentoku *et al.*, Phys. Plasmas **10**, 2009 (2003)

[43] M. C. Kaluza, Phd thesis at TU München, 2004

[44] S. P. Hatchett *et al.*, Phys. Plasmas **7**, 2076 (2000)

[45] A. Maksimchuk *et al.*, Phys. Rev. Lett. **84**, 4108 (2000)

[46] E. L. Clark, Phys. Rev. Lett. **84**, 670 (2000)

[47] S. C. Wilks *et al.*, Phys. Plasmas **8**, 542 (2001)

[48] M. Allen *et al.*, Phys. Plasmas **10**, 3283 (2003)

[49] J. Fuchs *et al.*, Phys. Rev. Lett. **94**, 045004 (2005)

[50] P. Mora, Phys. Rev. Lett. **90**, 185002 (2003)

[51] P. Mora, Phys. Rev. E **72**, 056401 (2005)

[52] J. Fuchs *et al.*, Nat. Phys. **2**, 48 (2006)

[53] J. Fuchs *et al.*, Phys. Rev. Lett. **91**, 255002 (2003)

[54] M. Key *et al.*, Phys. Plasmas **5**, 1966 (1998)

[55] for an overview see http://lfw.pennnet.com/articles/article_display.cfm?article_id=266389; www.physik.uni-jena.de/qe/Forschung/F-Deutsch/Petawatt/FP-Petawatt.html, www.llnl.gov/str/Petawatt.html, http://www.gsi.de/forschung/phelix/, www.clf.rl.ac.uk/news/CLF_News/petawatt.htm

[56] B. J. Albrigth *et al.*, Phys. Rev. Lett. **97**, 115002 (2006)

[57] T. Esirkepov *et al.*, Phys. Rev. Lett. **96**, 105001 (2006)

[58] J. Schreiber *et al.*, Phys. Rev. Lett. **97**, 1045005 (2006)

[59] E. d'Humières *et al.*, Phys. Plasmas **12**, 062704 (2005)

[60] A. Mackinnon *et al.*, Phys. Rev. Lett. **88**, 215006 (2002)

[61] I. Spencer *et al.*, Phys. Rev. E **67**, 046402 (2003)

[62] K. Nemoto *et al.*, Appl. Phys. Lett. **78**, 595 (2001)

[63] Y. Oishi *et al.*, Phys. Plasmas **12**, 073102 (2005)

[64] M. Hegelich *et al.*, Phys. Rev. Lett. **89**, 085002 (2002)

[65] Y. Murakami *et al.*, Phys. Plasmas **8**, 4138 (2001)

[66] K. Matsukado *et al.*, Phys. Rev. Lett. **91**, 215001 (2003)

[67] E. Fourkal *et al.*, Med. Phys. **30**, 1660 (2003)

[68] W. Luo *et al.*, Med. Phys. **32**, 794 (2005)

[69] J. Weichsel, *Application of Laser Accelerated Protons from Double-Layer Targets to Radiotherapy*, Diploma thesis, Ruprecht-Karls-Universität Heidelberg, 2007

[70] T. Bortfeld, Med. Phys. **24**, 2024 (1997)

[71] L. Hong *et al.*, Phys. Med. Biol. **41**, 1305 (1996)

[72] S. Nill, *Development and application of a multi-modality inverse treatment planning system*, PhD thesis, Ruprecht-Karls-Universität Heidelberg, 2001

[73] C. Geddes *et al.*, Nature 431, 538 (2004)

[74] S. Mangles *et al.*, Nature 431, 535 (2004)

[75] J. Faure *et al.*, Nature 431, 541 (2004)

[76] T. Tajima *et al.*, Phys. Rev. Lett. **43**, 267 (1979)

[77] V. Malka *et al.*, Science **298**, 1596 (2002)

[78] Agostinelli *et al.*, Nuclear Instruments and Methods in Physics Research A 506, 250 (2003)

[79] Gradshteyn and Ryzhik's *Table of Integrals, Series, and Products*, Academic press, 2000

Danksagung / Remerciements

Zum Schluss möchte ich mich noch bei allen bedanken, die zum (hoffentlichen) Gelingen dieser Arbeit beigetragen haben:

- Mein Dank gilt an erster Stelle Uwe Oelfke für die Aufnahme in seine Arbeitsgruppe und die Unterstützung während meiner Promotion.
- Herrn Professor Jürgen Debus danke ich für die Übernahme des Zweitgutachtens.
- Herrn Professor Wolfgang Schlegel möchte ich für die Aufnahme in seine Abteilung danken.
- Bei Hanitra Szymanowski bedanke ich mich für die Hilfe bei der Einarbeitung in die Grundlagen der Medizinphysik und Monte Carlo Simulationen.
- Bei Julian Weichsel möchte ich mich für die vielen ergiebigen Diskussionen und sehr angenehme Zusammenarbeit bedanken.
- Je voudrais exprimer mes vifs remerciements à Erik Lefebvre et Emmanuel d'Humières du Département de physique théorique et appliquée au Commissariat à l'Énergie Atomique (CEA), pour leur aide dans l'apprentissage des fondements de l'interaction laser-plasma et pour leur hospitalité pendant mes séjours dans leur institut.
- De plus je remercie Victor Malka et les membres de son Groupe Sources de Particules par Laser au Laboratoire d'Optique Appliqée de m'avoir donné un aperçu des expériences laser-plasma, en particulier Yannick Glinec et Alain Tafo.